ABSTRACT

Smith, Jennifer Connor. Structure-Property Relationships for Alternatively Stiff and Flexible Redox-Active Core Dendrimers of the Type, $[Fe_4S_4(S\text{-}Dend)_4]^{2-}$ (Under the direction of Professor Christopher B. Gorman)

The purpose of this work has been to establish structure-property relationships in novel redox-active core dendrimers. Alternatively stiff and flexible series of redox-active, iron-sulfur core dendrimers of the general structure $(nBu_4N)_2[Fe_4S_4(S\text{-}Dend)_4]$ (Dend = dendrons of generations 1 through 4) were studied. Molecular dynamics simulations were performed on dendrimer models to produce detailed pictures of three-dimensional structure. These simulations along with NMR experiments (Pulsed Field-Gradient Spin-Echo and Inversion Recovery) indicated that the flexible dendrimers are much more compact than the rigid dendrimers. In addition, the simulations indicated an offset and mobile iron-sulfur core. In contrast, the rigid dendrimers were open with a more central and relatively immobile iron-sulfur core. Heterogeneous electron transfer rate constants measured using cyclic voltammetry and Osteryoung square wave voltammetry, indicated that the rigid dendrimers were more effective at attenuating the rate of electron transfer than were the flexible dendrimers of comparable molecular weight. These key structural differences for alternatively stiff and flexible dendrimers turned out to play a critical role in rationalizing their electron transport properties. That is, the offset positioning of the core in the flexible dendrimers permits facile ET to/from a poised platinum electrode compared to the rigid dendrimers, where the core is centrally positioned. While the dendrimers containing rigid ligands had better encapsulated redox cores for a given molecular weight, these molecules had higher electron transfer rates for a given molecular radius. Moreover, for the rigid dendrimer series, the attenuation of electron transfer was modest as the molecular size increased, indicative of a highly “conductive” medium. This behavior was not observed in the flexible series. Here, a steeper attenuation of the ET rate constant was observed as molecular size increased, indicative of a comparably more insulating ET medium.

Structure-Property Relationships for Alternatively Stiff and Flexible Redox-Active Core Dendrimers of the Type, $[Fe_4S_4(S\text{-}Dend)_4]^{2-}$

by

JENNIFER CONNOR SMITH

A dissertation submitted to the Graduate Faculty of
North Carolina State University
in partial fulfillment of the
requirements for the Degree of
Doctor of Philosophy

CHEMISTRY

Raleigh

1999

APPROVED BY:

Chair of Advisory Committee

To Fabio

Jennifer Connor Smith was born to Judith Connor and William Francis Smith, Jr., February 22, 1972 in Goldsboro, North Carolina. Jennifer spent the majority of her childhood in Washington, North Carolina. After graduating second in her class from Washington High School in 1990, Jennifer attended the University of North Carolina at Chapel Hill, North Carolina. Ultimately taking a B. A. in Chemistry, Jennifer attended Graduate School in Chemistry at North Carolina State University. Here, she met and married Fabio Palazzo of Rochester, New York. Jennifer has one sister, Lindsay Winning Smith.

ACKNOWLEDGMENTS

First and foremost, I would like to acknowledge my advisor and mentor, Professor Chris Gorman. Professor Gorman has had and will continue to have a huge influence on my personal development as a teacher, researcher and scholar.

I would like to acknowledge past and present members of the Gorman Group, particularly, those members involved in the preparation of the materials studied herein. They are Dr. Kang Y. Chen, Mr. Brandon L. Parkhurst, and Dr. Michael W. Hager. Additionally, I would like to acknowledge all my colleagues in the Gorman, Linderman, Shultz, and Bowden groups; for the opportunity to work in a stimulating and interactive multidisciplinary research environment.

I would like to acknowledge North Carolina State University NMR Facility staff members, Dr. Hanna Sierzputowska-Gracz and Dr. Sabapathy Sankar, for their time and instruction. Additionally, several extremely enlightening discussions with Professor Ed Stejskal on Pulsed-Field Gradient NMR spectroscopy and Inversion Recovery are gratefully acknowledged.

I would like to acknowledge the North Carolina Supercomputing Center (Research Triangle Park, NC) for generous allocation of supercomputing resources and technical support.

Finally, I would like to acknowledge my parents, Judy and Bill Smith for teaching, by example, commitment, perseverance, scholarship and the true meaning of success. Additionally, I would like to thank all of my family and friends for their support and companionship.

TABLE OF CONTENTS

LIST OF FIGURES AND SCHEMES

CHAPTER 1

LIST OF TABLES

PREFACE

Controlling electron transport at a prescribed distance, direction or time-scale is a centerpiece of many nanoscale device schemes. To this end, novel molecular design strategies founded on structure-property relationships governing electron transport (ET) on the molecular-length scales must be elucidated. In this body of work, alternatively rigid and flexible Fe_4S_4-core metallodendrimers were studied to map out the influences of relative conformational flexibility on ET properties. In addition, these architectures were also considered from the standpoint of the "conductivity" of the individual chemical units. The most poignant discoveries outlined at the end of Chapter 2 underscore the interplay of these two chemical properties, conformational flexibility and conductivity through chemical bonds from an ET perspective.

Nature has already demonstrated a mastery over controlling ET on the molecular scale. The interplay between conformation and relative molecular-scale conductivity is at play there as well. Proteins, for example, use secondary and tertiary structure to pass electrons around in the body at very precise distances and time-scales. The body of work presented here is not biochemical at all. Nevertheless, we found it profitable and illustrative to consider our results within the context of ET in bio-organic superstructures; such as proteins and DNA. Therefore, a survey and background of ET in organic superstructures from a biochemical perspective is included in Chapter 1 of this thesis. The following four chapters explicate structure-property studies on metallodendrimers; both experimental and computational.

CHAPTER 1

LONG RANGE ELECTRON TRANSFER IN SUPRAMOLECULAR ORGANIC CHEMISTRY — A BIOCHEMICAL PERSPECTIVE

"In nature's infinite book of secrecy
A little can I read."
W. Shakespeare: Antony and Cleopatra.

1.1. Introduction

Electron Transfer (ET) is the most fundamental of chemical reactions. It is a shift of charge density in a donor-acceptor system by the transfer of an electron from one orbital centered on a donor site to another orbital centered on an acceptor site. Just like any chemical reaction, the time-scale, mechanism and driving force for the reaction depends on the structural and energetic features of reactants, products and surrounding medium.

Long range ET represents an interesting class of reactions in which donor-acceptor sites are situated at large distances from one another. The critical parameter when thinking about long range ET in supramolecular organic molecules is electronic transmission of the intervening medium between donor and acceptor. *Conductivity* is the equivalent macroscopic term, and will be used throughout; albeit in quotations. Since Marcus' semi-classical theory on ET, much effort has been devoted to mapping out the precise role and proper theoretical treatment of the intervening medium between donor and acceptor.

The recent emergence of nanoscale technology has unveiled the possibility for controlling electron transport on macromolecular length-scales. Many of the schemes for nanoscale devices incorporate macromolecules designed to facilitate ET at a prescribed distance, direction or timescale. To date, our understanding of the rules governing supramolecular ET is still in its infancy. Nature, however, has already mastered ET in supramolecular organic systems. Our expertise in designing functional electroactive supramolecular systems starts with an understanding of the structure-property relationships governing ET in biomacromolecules. For this reason, an introduction to long range ET from a biological perspective is important and presented here.

Historically, mapping out the rules for long range ET in biomacromolecules has proved challenging. Long range ET reactions are ubiquitous in Nature and can occur readily despite very large donor-acceptor site-separation and poor orbital overlap. Organic chemists have struggled to understand and emulate Nature's most efficient ET architectures. Progress is being made. However much can still be learned from Nature

about the rules for predicting and controlling long range ET in organic superstructures. Emerging paradigms will be critical in fields ranging from biochemistry and biotechnology to supramolecular organic materials chemistry.

1.2. History

Marcus and Hopfield made seminal contributions to the theory behind long range ET. In the late 50's, Marcus introduced the Landau-Zener modified theory of ET.[1-3] The key new feature of this semi-classical theory was that ET rate depends on an electronic coupling factor, H_{DA}, between donor-acceptor in addition to those parameters considered initially in classical Marcus theory, the standard reaction free energy, ΔG^{o}, and nuclear reorganization energy, λ. Marcus also proposed a strong, exponential dependence of the electronic coupling factor, H_{DA}, on intersite distance. Techniques for applying Marcus theory to real problems in long range ET remained elusive for sometime afterward.

In 1974, Hopfield proposed a 1-D barrier model for predicting rate-distance-dependence in ET proteins.[4] In this theoretical model, a square tunneling barrier (Figure 1.1) approximated the electronic coupling factor between donor-acceptor. The model described a probability, ρ, that an electron could "jump the gap" as an exponentially decaying function of donor-acceptor separation distance. (Equation 1.1) In Equation 1.1, R_o is the edge-to-edge donor-acceptor distance and R is the intersite separation. The strength of the exponential decay curve in Hopfield's model was represented mathematically as a pre-exponential term, β, in Equation 1.1. This was the birth of the distance-decay parameter, β. Modern researchers have used the distance-decay parameter, β, as an indication of medium "conductivity."

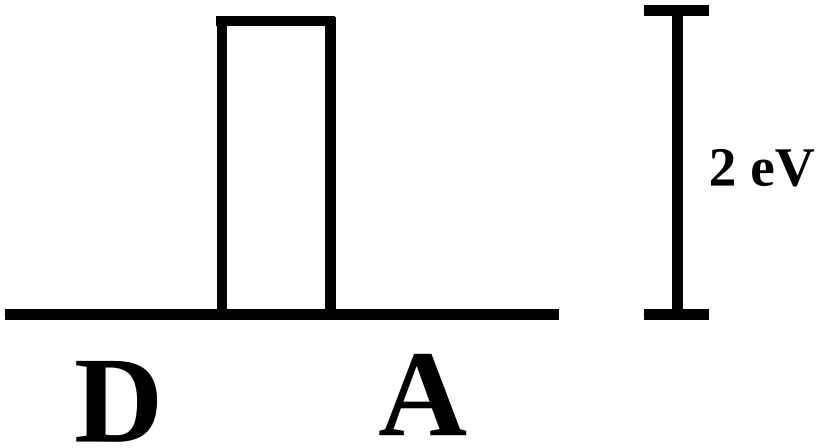

Figure 1.1. Hopfield's simple description of electron tunneling in proteins assumed that a square barrier existed between donor-acceptor sites. The probability that an electron passed over the barrier is a strong function of the barrier height and intersite distance.

$$\rho = \exp(-\beta(R - R_o)) \qquad \text{(Equation 1.1)}$$

Incorporating no chemical details about the chemical nature of the intervening medium, Hopfield's ET transfer model was unsophisticated, but illuminating in an era void of high-resolution three-dimensional structure-determination. This simple model predicted a distance-decay parameter, β = 1.45 $Å^{-1}$ by invoking a 2 eV electron tunneling barrier. The tunneling barrier was based generally on the HOMO-LUMO gap in amino acid matrices. In 1992, Dutton and coworkers reported a similar distance-decay factor (β = 1.4 $Å^{-1}$) on average for long range ET in and around the photosynthetic reaction center.[5] The consistency of this measurement with Hopfield's prediction substantiated the treatment of protein medium, or any other medium, as a coarse-grain dielectric continuum.

McConnell first challenged the continuum model- at least for synthetic donor-acceptor systems.[6] He invoked the concept, "superexchange," that interactions among "virtual orbitals" within chemical units in a donor-acceptor bridge could facilitate electron migration over long distances.[7] The McConnell model considered only covalent bonding

interactions and predicted an exponential dependence of electronic coupling with donor-acceptor bridge length. Although this model pioneered the concept of superexchange and did well predicting ET in bridged organic donor-acceptor complexes, it failed for biological ET in proteins.

By the 80's, technological and scientific advances helped uncover the details of protein three-dimensional structure-function relationships. The ability to determine three-dimensional structure using high resolution X-ray crystallography and multi-dimensional NMR spectroscopy facilitated atom-scale theoretical models for long range ET. Additionally, innovative experimenters began uncovering new mechanistic details and structure-property relationships for long range ET in proteins and DNA. Pioneers in the field of long range biological ET today have begun to answer the most fundamental questions. What structural features facilitate the transfer of an electron over very large distances? How important is protein tertiary and secondary structure compared to primary structure? Precisely, what role does hydrogen-bonding play in long range ET? Why and how has Nature come to use long range ET as an instrument for biological machinery? What factors permit chemists to engineer synthetic ET systems for novel applications? To answer these questions, one must start with the simplest of models for an ET reaction. (Figure 1.2)

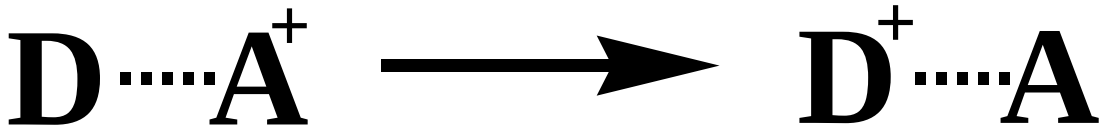

Figure 1.2. An ET reaction scheme for a symmetrical intervalence compound with a donor site (D) and an acceptor (A) site.

1.3. Marcus Theory

1.3.1. Fundamentals

In the late 50's, Marcus introduced a seminal theory for estimating outer-sphere electron transfer (ET) from the reorganization energy, λ, reaction free energy, ΔG^o, and an electronic coupling factor, H_{DA}.[1-3,8] (Equation 1.2a and 1.2b) Fundamentally, Marcus pioneered the use of nuclear potential energy surfaces to predict the migration of charge in donor-acceptor systems. The basic theory hinges on the notion that charge migration is dictated by forcefield imposed by the surrounding nuclei. These forces can be considered constant on the ET timescale. This is an application of the Born-Oppenheimer approximation. The theory can be illustrated within the context of a simple donor-acceptor system shown in Figure 1.2.

$$k_{ET} = \kappa \exp\left(\frac{-\left(\Delta G^o + \lambda\right)^2}{4\lambda k_B T}\right) \qquad \text{(Equation 1.2a)}$$

or

$$k_{ET} = \underbrace{\left(\frac{4\pi^3}{h^2 \lambda k_B T}\right)}_{\text{frequency factor}} \underbrace{\left(H_{DA}\right)^2}_{\text{electronic coupling factor}} \underbrace{\exp\left(\frac{-\left(\Delta G^o + \lambda\right)^2}{4\lambda k_B T}\right)}_{\text{nuclear term}} \qquad \text{(Equation 1.2b)}$$

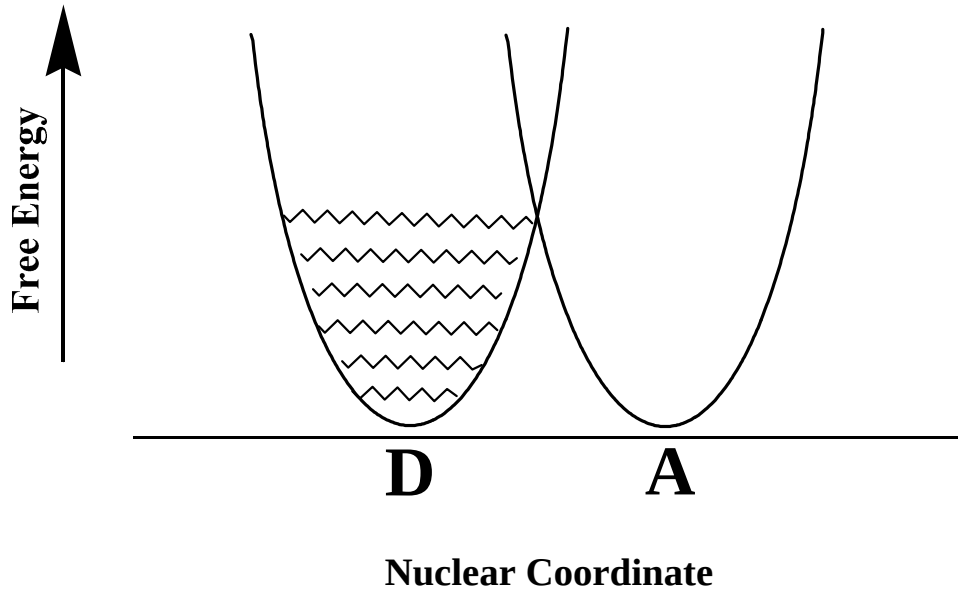

Figure 1.3. Migration of an electron from state D to state A was described by the interaction of the two harmonic wells.

Pictorially, the electronic states were represented classically by harmonic wells. (Figure 1.3) One-dimensional slices through the potential energy hypersurfaces as in Figure 1.3 are often shown, although the complete description incorporated 3N dimensions where N = number or atoms in the donor-acceptor sites plus the surrounding solvent molecules. Migration of an electron from state D to state A was described by the interaction of the two harmonic wells. Marcus theory was considered semi-classical since the vibrational states among local covalent nuclei were expressed quantum mechanically and the configuration of the solvent nuclei were treated classically.

The classical Marcus equation has two parts, the pre-exponential, κ, and the exponential term, called the nuclear term. (Equation 1.2a and 1.2b) The exponential term describes how the positioning of the surrounding nuclei related to the ET rate. The pre-exponential factor, κ, quantifies the probability that, upon initiation, an electronic transition will proceed in the forward direction. It was conceived as a normalization constant similar to the pre-exponential factor in the Arrhenius equation used in transition state theory.

The two components of κ are the frequency factor, $4\pi^3/h^2\lambda k^oT$, and the electronic coupling factor, H_{DA}. (Equation 1.2b) The frequency factor relates the vibrational tendencies of a donor-acceptor system to the probability of ET. This frequency factor is usually incorporated as a constant, 10^{-13} sec^{-1}. This number represents the *classical* "attempt frequency." This is the number of times per second that an electron attempts to jump from D to A based on molecular vibrational states. This constant may or may not change with intersite separation. Usually, it is assumed to be distant independent and therefore has no bearing on relative rates. The H_{DA} term was insignificant mathematically ($H_{DA} = 1$) for neighboring donor-acceptor sites. However, the value of H_{DA} becomes extremely important when donor-acceptor sites are separated. In fact, Marcus showed that the electronic coupling term, H_{DA}, virtually overshadowed all the other terms in the Marcus equation when donor-acceptor sites are situated far apart in space.

1.3.2. The Electronic Coupling Factor, H_{DA}

Although Marcus theory does not consider orbital energies from first principles, a discussion of H_{DA} from the standpoint of first order perturbation theory has proved helpful. Consider the electronic coupling factor, H_{DA}, between the donor and acceptor sites, D and A. Assuming that the electronic wavefunctions at the donor site D and acceptor site A are Ψ_A and Ψ_B, one could express their mathematical relationship as an energy matrix. Figure 1.4 shows the energy matrix for the simple donor-acceptor pair using Ψ_D and Ψ_A as the basis set. The off-diagonal terms, $\Psi_D\Psi_A$ and $\Psi_A\Psi_{D,}$ are the "transfer integrals" also known as the "overlap integrals," to draw a parallel with simple Hückel theory. The magnitude of the overlap integral was proportional to the electronic coupling factor, $H_{DA,}$ and therefore, κ. Figure 1.5 illustrates how the time-scale and *mechanism* for this simple ET reaction depends on the pre-exponential, κ. Marcus predicted three regimes that represent the spectrum of κ-values that can appear in the Marcus Equation. These regimes are illustrated in Figure 1.5.

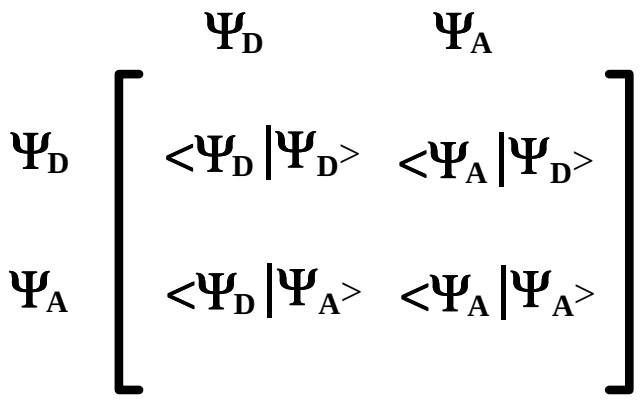

Figure 1.4. The energy matrix for a donor-acceptor system using Ψ_D and Ψ_A as a basis set. Off diagonal terms, $\Psi_D\Psi_A$ and $\Psi_D\Psi_A$, represent the overlap integrals (or transfer integrals). The overlap integrals describe the magnitude of orbital overlap, and is proportional to the electronic coupling factor, H_{DA}, and therefore κ.

Case 1, $\kappa = 1.0$.

Mathematical explanation: Marcus showed that when the electronic coupling factor, H_{DA} was extremely large, the pre-exponential factor, κ, was not rate-limiting. Marcus used κ = 1.0 in Equation 1.2a to express this fact. This indicated a 100% probability that once initiated, an electron would proceed from the donor to the acceptor orbital. In this regime k_{ET} was dependent only on the reaction free energy, ΔG^o, and the reorganization energy, λ.

$$k_{ET_{Case1}} = 1.0 \times \exp\left(\frac{-\left(\Delta G^o + \lambda\right)^2}{4\lambda\, k_B T} \right) \qquad \text{(Equation 1.3)}$$

Physical picture: Marcus showed that when the electronic coupling factor, H_{DA} was extremely large, the two "wells" or electronic states mixed very effectively, as shown in Figure 1.5, Case 1. The consequence of such efficient mixing of states was that no kinetic barrier to ET develops between the donor and acceptor sites, resulting in a 100% probability the electron can migrate from donor to acceptor (κ = 1.0). In the ideal case, where ΔG^o = 0, ET happens so fast, an unpaired electron is effectively delocalized in the

ground state. The ET transition proceeds along a *confined* potential energy surface; therefore this mechanism was considered adiabatic- Greek for "*confined*."

Case 2, $\kappa < 1.0$.

Mathematical explanation: Marcus showed that when the electronic coupling factor, H_{DA} was modest, the pre-exponential factor, κ, was rate-limiting along with the nuclear term. Marcus used $\kappa < 1.0$ to express this fact. There was a less than 100% probability that an electron will proceed from the donor to the acceptor orbital. According to Equation 1.2a and 1.2b, the rate of ET was dependent, on κ, as well as ΔG^o and λ. By the reasoning outlined above, this ET reaction was considered adiabatic.

$$k_{ET_{Case\ 2}} = \kappa \times \exp\left(\frac{-\left(\Delta G^o + \lambda\right)^2}{4\lambda\, k_B T} \right); \quad \kappa < 1.0 \qquad \text{(Equation 1.4)}$$

Physical picture: Marcus showed that when the electronic coupling factor, H_{DA} was modest, the two "wells" or electronic states could mix, although not as effectively as in Case 1. (Figure 1.5) The consequence of this type of mixing was the development of a kinetic barrier between the donor and acceptor sites, resulting in a <100% probability the electron could migrate from donor to acceptor ($\kappa < 1.0$). These types of ET reactions were theoretically analogous to unimolecular chemical reactions obeying first-order or (pseudo first-order) reaction kinetics. Application of traditional transition state theory to the ET reaction was appropriate in most cases.[9]

Case 3, $\kappa << 1.0$.

Mathematical explanation: Marcus showed that when the electronic coupling factor, H_{DA} was extremely small, the pre-exponential factor, κ, alone was rate-limiting. In the face of a negligibly small κ-value, the exponential nuclear term in Equation 1.2a and 1.2b was set to 1.0 by Marcus; indicating that the probability of ET was solely determined by the

pre-exponential term, **κ,** comprised of the frequency factor and the electronic coupling factor, H_{DA}. As previously mentioned, H_{DA} is the critical parameter in long range ET and dominates the ET rate for long range ET. Therefore, long range ET rates are proportional to the strength of the electronic coupling between donor and acceptor.

$$k_{ET_{Case\,3}} = \kappa \times 1.0 \approx H_{DA} \qquad \text{(Equation 1.5)}$$

Physical picture: When the electronic coupling factor, H_{DA} was negligibly small, the two "wells" or electronic states could not mix due to poor orbital overlap. (Figure 1.5) The consequence of this lack of mixing was virtually a zero probability of overcoming the barrier between the two states. To circumvent the insurmountable barrier, an alternative "pathway" for ET was proposed by Marcus. Here, the electron was vibronically excited and then made a vertical jump up to the acceptor site's potential energy surface. The activation energy for this process is represented in Figure 1.5 by the solid arrow in Case 3. This vertical jump theory permitted the electron to "tunnel" from potential energy surface to potential energy surface (donor-to-acceptor) in the absence of any orbital mixing. Since the electron was not confined to a single potential energy surface, ET in this regime is considered non-adiabatic- Greek for "not confined." The hashed arrow in Figure 1.5, Case 3, represents the magnitude of the nuclear reorganization energy, λ. The solid line indicates the magnitude of the activation energy, E_a. Marcus theory predicts that the activation energy, E_a for nonadiabatic ET is ¼ the nuclear reorganization energy. This quantity can be derived by analytical geometry on the overlapping parabolic representations of the electron energy in Marcus model for ET. (Figure 1.5, Case 3)

Long range ET reactions in organic media generally fall into the last two categories. It is not hard to rationalize why long range ET reactions fall into the second and third coupling regimes, since the overlap integral, and therefore the electronic coupling, for orbitals that are far apart in space should understandably be modest.

Biologically relevant long range ET reactions typically fall into the third coupling regime. These ET reactions exhibit negligibly small electronic coupling between

donor-acceptor sites and undergo non-adiabatic ET. Instead of proceeding along a single energy hypersurface the electron must jump or (tunnel) from donor site to acceptor site. For this reason, biologically relevant long range ET is often referred to as "tunneling."

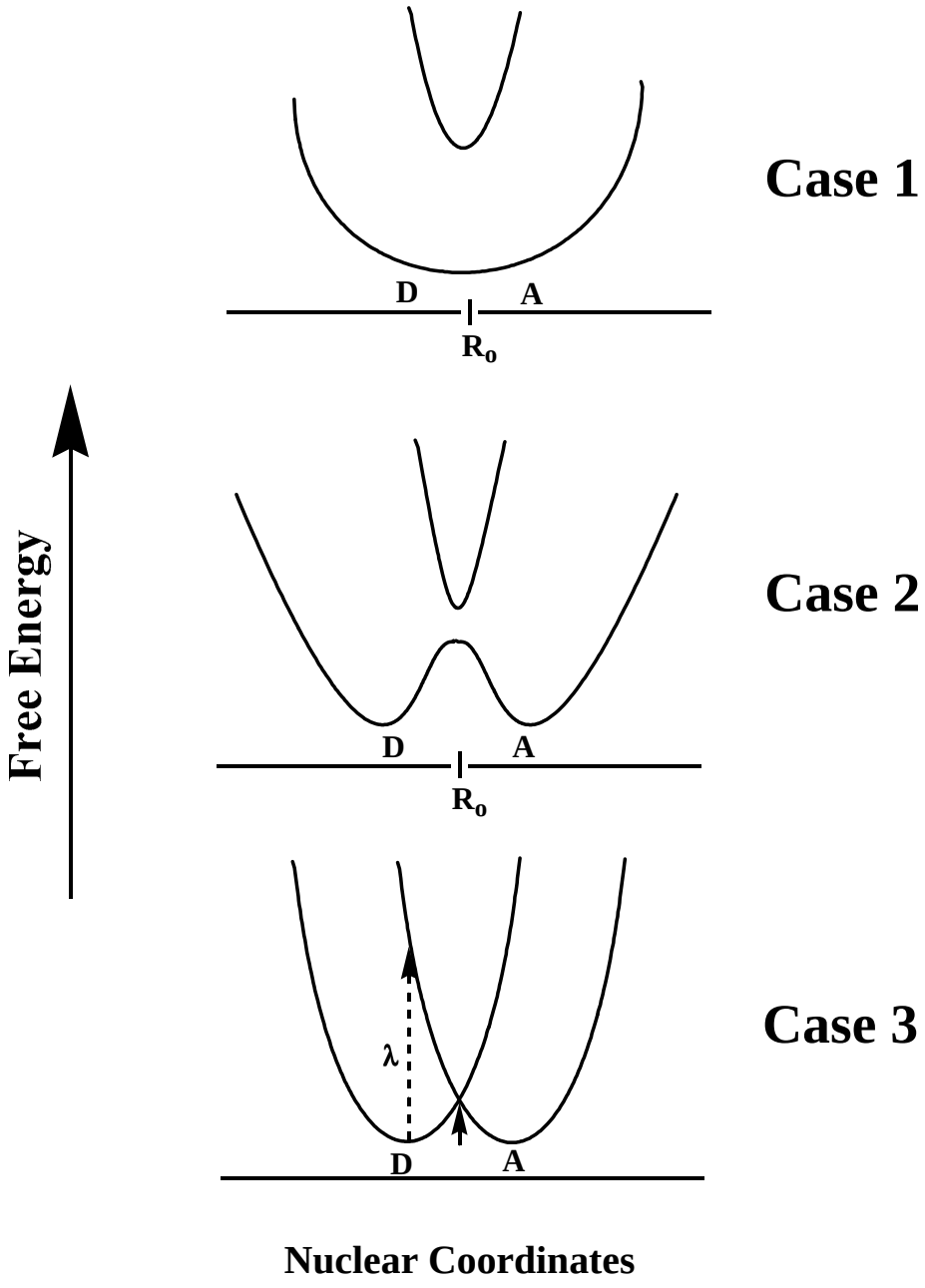

Figure 1.5. Electronic coupling regimes for ET between donor-acceptor sites in the simplest case, where $\Delta G^o = 0$. Case 1: $\kappa = 1.0$. Case 2: $\kappa < 1.0$. Case 3: $\kappa << 1.0$. For Case 3, the solid arrow represents the vertical jump necessary for non-adiabatic ET. The length of the arrow is proportional to the activation energy. The hashed arrow represents the nuclear reorgannization energy, λ.

As demonstrated for Case 3 ET, the influence of electronic interactions usually dominates nuclear reorganization energy and changes in ET reaction free energy. There are exceptions. Consideration of nuclear reorganization and ET reaction free energy may be important, especially for long range ET in DNA.[10-19] For this reason, a brief account of semi-classical Marcus theory from the standpoint of nuclear reorganization and reaction free energy is presented below.

1.3.3. The Nuclear Factor

The semi-classical Marcus equation for ET incorporated, in addition to the pre-exponential electronic term, κ, and an exponential term, the Nuclear Factor. (Equation 1.2a and 1.2b) The Nuclear Factor described the dependence of k_{ET} on the re-positioning energy of nuclei surrounding the donor-acceptor sites, λ, and the ET reaction free energy change, ΔG^o. In some cases, these factors are assumed to be negligible for electron tunneling in biomacromolecules. (Section 1.3.2) There is indeed an exception to this rule. Marcus predicted that for non-adiabatic ET (this usually means long range ET) where the reaction driving force, $-\Delta G^o$, is extremely large, the nuclear factor may confer a significant influence on k_{ET}. This is a manifestation of the Marcus inverted region.

$$k_{ET} = \left(\frac{4\pi^3}{h^2 \lambda k_B T} \right) (H_{DA})^2 \exp\left(\frac{-(\Delta G^o + \lambda)^2}{4\lambda k_B T} \right) \qquad \text{(Equation 1.2a)}$$

or

$$k_{ET} = \kappa \exp\left(\frac{-(\Delta G^o + \lambda)^2}{4\lambda k_B T} \right) \qquad \text{(Equation 1.2b)}$$

Upon quantitative analysis of the exponential term in Equation 1.2a (or 1.2b), a maximum in the function existed when $\lambda = -\Delta G^o$. Under those circumstances, the classical Marcus scheme predicts an effective $E_a = 0$. (Figure 1.6) This meant that as the driving force for an ET reaction increases, k_{ET} increased, passes through an inflection point, and then decreases. This was perhaps the most provocative prediction that came out of Marcus theory; the so-called Marcus "inverted region." The practical implication of Marcus' prediction was the existence of an inflection point in the k_{ET} versus $-\Delta G^o$ graph.

Experimental evidence for the "inverted region" remained elusive until Miller and coworkers confirmed the existence of the "inverted region" in a seminal report in 1979.[20,21] The experiments that illustrated the Marcus "inverted region" employed long range intramolecular ET reactions within rigid organic molecules. Figure 1.6 illustrates the concept of the Marcus "inverted region" for non-adiabatic ET reactions.

Additionally, Marcus assumed that a major contribution to the reorganization energy, λ, was that of the solvent nuclei. This prediction has been borne out experimentally as well. Several groups showed that the characteristic free energy maximum (the inflection point in the k_{ET} versus $-\Delta G^o$ plot) can be attenuated by changes in solvent polarity.[22-25] The implications of this rule in biological ET was striking. By manipulating the solvent environment around a redox unit, Nature could favor certain ET pathways over competing ET pathways, even if the latter were thermodynamically favored. This observation underscored the concept that driving force alone does not dictate ET pathways.

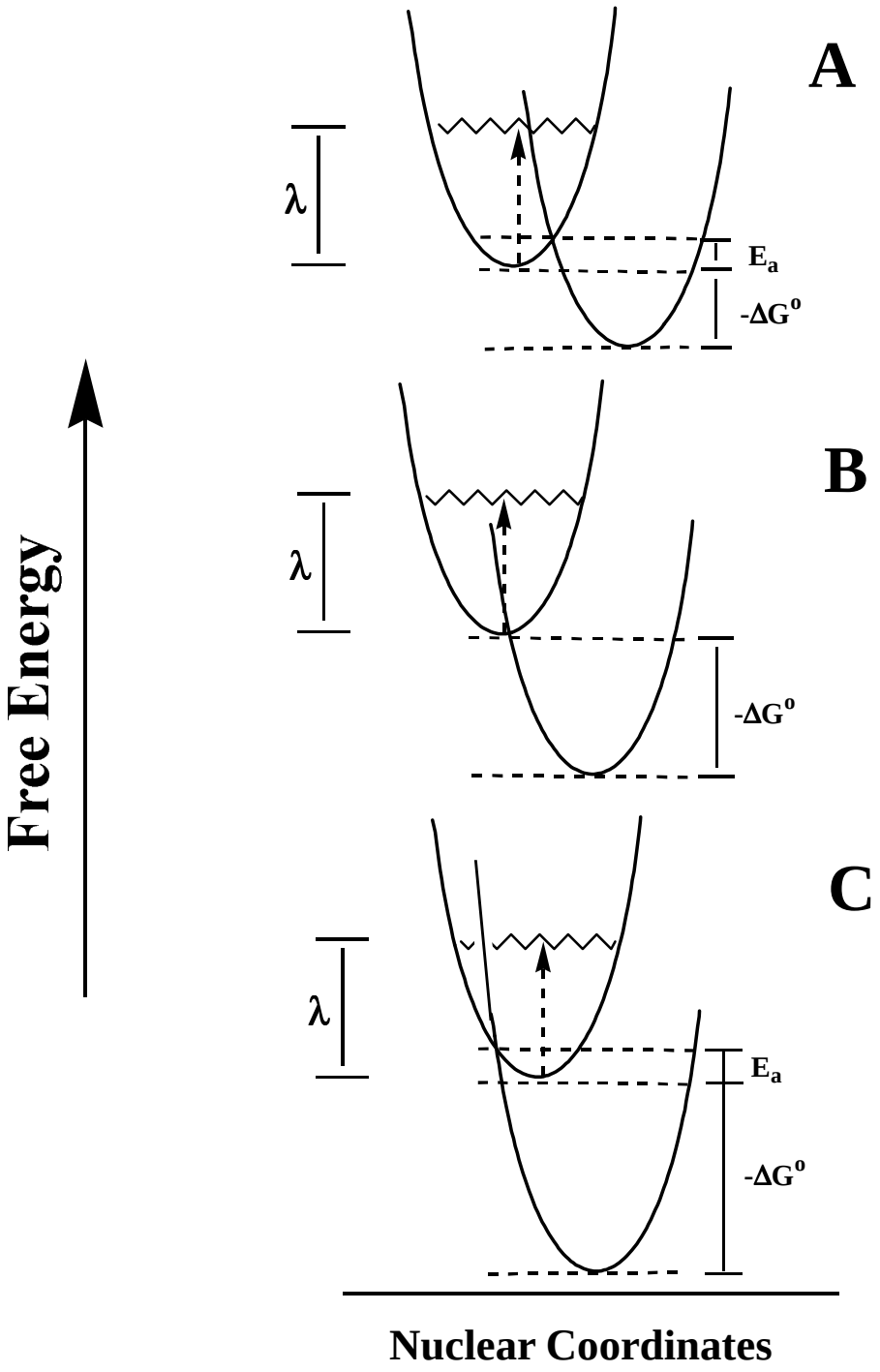

Figure 1.6. A classical one-dimensional representation of the Marcus "inverted region," A) $-\Delta G^o < \lambda$, activation barrier is present; B) $-\Delta G^o = \lambda$, activation barrier disappears, and C) $-\Delta G^o > \lambda$, activation barrier reappears.

1.3.4. β Within the context of Marcus theory

Origin of β

Historically, long range ET in organic media had been examined from the standpoint of how k_{ET} changed with donor-acceptor separation. Typically, k_{ET} decays exponentially with distance. The distance-dependence of the decay was considered to be a manifestation of the "conductivity" of the intervening medium. Accordingly, Marcus theory predicted that the rate-distance-dependence would be reflected largely in the pre-exponential electronic coupling factor, H_{DA}, within **κ**. It is helpful to point out here that the distance-dependence of the nuclear reorganization energy, λ, may play a part. For any experimental determination of β, distance-dependence of the reorganization energy must be ruled out. Despite this caveat, the distance-dependence of H_{DA} was expressed commonly as an exponential function of the intersite separation distance. (Equation 1.6a and Equation 1.6b) The exponential scaling factor, **β**, indicated the strength of the exponential decay. A small **β** indicated that H_{DA} dropped off slowly with distance; indicative of highly "conductive" medium. A large **β** indicated that H_{DA} dropped off quickly with distance, indicative of poorly "conductive" medium.

$$H_{DA}^{\ 2} = H_{DA_o}^{\ 2} \exp\left(-\beta\left(R - R_o\right)\right) \qquad \text{(Equation 1.6a)}$$

or

$$H_{DA} = H_{DA_o} \exp\left(-\beta\left(R - R_o\right)/2\right) \qquad \text{(Equation 1.6b)}$$

Direct measurement or calculation of H_{DA} is extremely difficult. Direct measurement of k_{ET} is straightforward by comparison. Therefore, researchers made the approximation that $H_{DA} \sim k_{ET}$. (Equation 1.7) Here, k_{ET} is the experimental ET rate constant, k_{ET_O} is the ET rate constant for the edge-to-edge donor-acceptor configuration, R is the distance separating donor and acceptor and R_O is the donor-acceptor distance in the edge-to-edge configuration.

$$k_{ET} = k_{ET_o} \exp(-\beta(R - R_o)) \qquad \text{(Equation 1.7)}$$

Interpretation of β

In practice, a graph relating log k_{ET} to the donor-acceptor site separation will give a straight line, the slope of which is **-β**. The value **β**, indicates the steepness of the slope – thus the strength of the distance-dependence. The approximation leading to Equation 1.6a and 1.6b stems from the semi-classical Marcus equation for non-adiabatic ET. (Equation 1.2b) Close examination of this equation revealed that the approximation required an assumption that the contribution from the nuclear factor (λ and ΔG^o) remains constant with increasing distance. Marcus showed that this assumption was valid for **κ** <<< 1.0. This was "usually" the case for long range ET pathways in rigid organic and biological ET systems.

Anomalies in measured **β**-values in duplex DNA have been documented, fueling a controversy about the relative "conductivity" of stacked DNA base pairs. One explanation for scattered **β**-values was the poorly defined distance-dependence of $-\Delta G^o$ and λ, resulting in the invalid or improper application and interpretation of **β**. Other researchers have questioned the validity of treating long range ET as a direct through-space interaction. Use of **β** implies transfer over the shortest straight-line distance from donor to acceptor. However, the possibility of meandering bonded pathways exists as well.

Alternative representations for β

Figure 1.7 demonstrates an alternative mechanism for ET in which charge hops down a pathway of covalent chemical bonds- instead of following the geometrically shortest through-space pathway. This type of pathway would prevail when a superexchange mechanism dominates the ET transfer process. For such a scenario, the ET rate is mapped against the number of intervening bonds in a pathway, rather than the straight-line distance. The distance-dependence of the electronic coupling factor is

expressed as a function of bond number instead of intersite distance.[26] (Equation 1.8a and 1.8b) Here N = the number of bonds in the ET pathway. This through-bond pathway will be discussed in detail in Section 1.4.3.

$$H_{DA}^{\ 2} = H_{DA\,o}^{\ 2}\exp\left(-\beta\left(N-1\right)\right) \qquad \text{(Equation 1.8a)}$$

or

$$H_{DA} = H_{DA\,o}\exp\left(-\beta\left(N-1\right)/2\right) \qquad \text{(Equation 1.8b)}$$

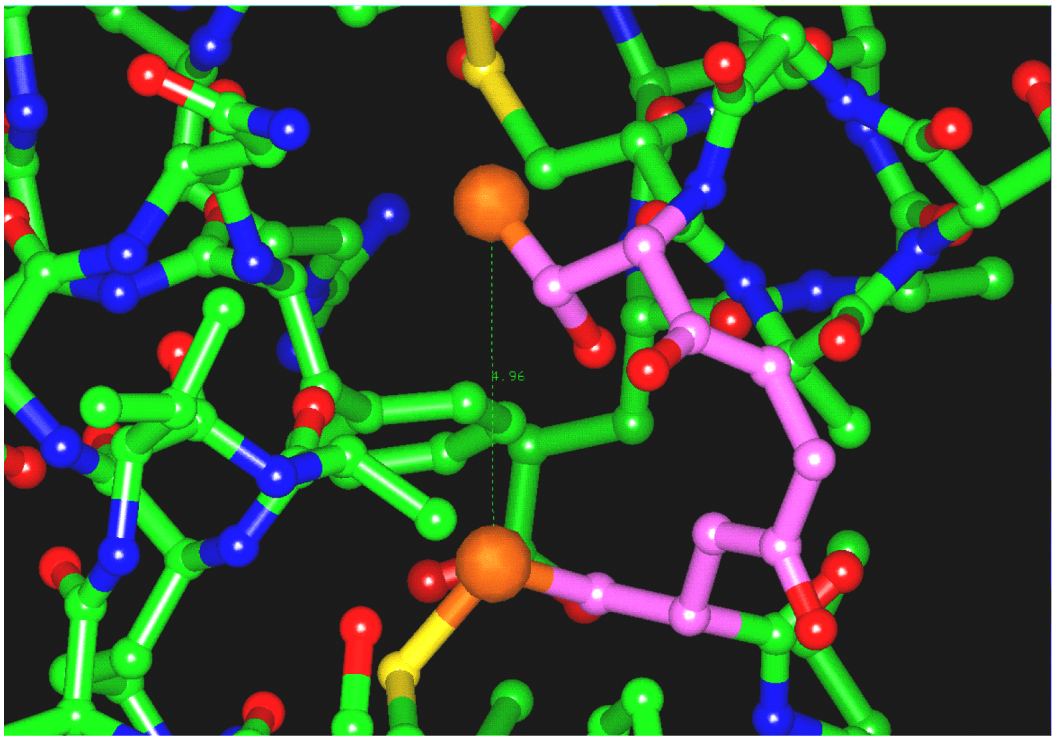

Figure 1.7. A hypothetical through-bond pathway within a protein matrix (colored pink). The orange-colored donor-acceptor sites are not real redox center, but help to illustrate pathways length-scales. The site-to-site through-space pathway is 4.96 Å. The through-bond pathway is ~15 Å.

1.4. Mechanisms for long range ET

1.4.1. General Considerations

Generally, β-values for σ-bonded organic media (biological and synthetic) fall within a small range, about 0.85-1.5 $Å^{-1}$. In a landmark report in 1993, Barton and coworkers measured an unprecedented β-value of 0.2 $Å^{-1}$ for ET over extreme distances (>35 Å) through the major axis of a duplex DNA.[14] Since this discovery, others have reported various values ranging from 0.65-1.4 $Å^{-1}$ for analogous (not identical) systems. These anomalies forced a reconsideration of the current models and theories for long range ET in supramolecular systems. Controversy surrounded the meaning and validity of experimentally measured β-values. At the heart of the debate was the general consensus that a need exists to discover details of the mechanism(s) directing long range ET.

1.4.2. Through-space

There are in fact three known mechanisms of ET over large distances. The zeroth order interaction between any donor-acceptor pair is the overlap of their electronic wavefunctions through-space. This through-space mechanism is expected to exhibit a strong exponential distance-dependence, reflecting the exponential decrease in orbital density with distance. Many researchers find it hard to rationalize this mechanistic pathway for ET in intermediate – long distance transfer regimes.

1.4.3. Through-bond (superexchange)

To some, a more plausible explanation for long range ET in the 5-15 Å regime is a through-bond superexchange mechanism, in which interactions among electronic wavefunctions located along the intervening ET bridge are considered to help electronically couple the donor-acceptor sites. Researchers invoke the superexchange mechanism to explain exponentially decaying distance or bond number-dependent rate constants. Typically, β-values quantify the strength the exponential decay, and thus the "conductivity" of the medium.

Early on the concept of a through-bond superexchange pathway was a provocative one. In 1986, Closs and coworkers obtained direct experimental evidence that a through-bond coupling mechanism dominates through-space coupling.[24] These researchers examined the electronic coupling factor, H_{DA}, (as deduced by ET rates) for two decalin isomers (Figure 1.8) in which the donor-acceptor separation distance varied by a factor of 2. (Figure 1.8) The researchers found that the electronic coupling factor was nearly constant for the two decalin systems depicted in Figure 1.8. In fact, a slightly stronger coupling was found in the extended molecule. (63 versus 58 cm^{-1}; with the smaller and weaker coupling factor measured for the diaxial substituted decalin system.)

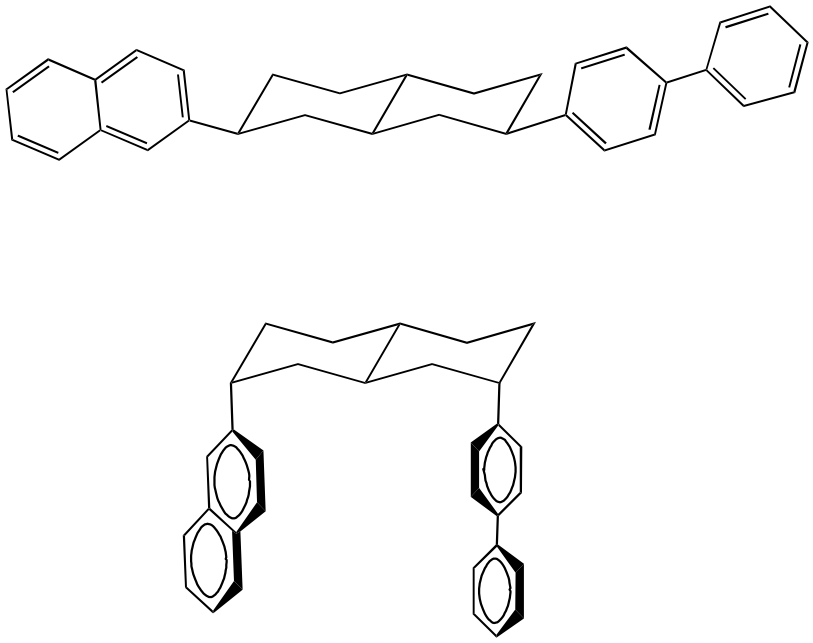

Figure 1.8. Decalin isomers used to examine the relative contributions from through-space and through-bond mechanisms.[24] The center-to-center distance between donor and acceptor is 12.5Å (top) and 6.2Å (bottom).

1.4.4. Electron hopping

A third mechanistic pathway evolved recently, as a result of experimental results that could not be explained from the standpoint of a superexchange mechanistic pathway. These experiments, in particular, involved ET over very large pathways – which incorporated energetically low lying states along the pathway. Electron migration in these systems were hypothesized to occur by a hopping mechanism, whereby the electron migrated from the donor site to acceptor site via a series of hops to low lying intermediate states along the pathway. Long range ET via this hopping mechanism exhibited a very shallow distance-dependence for k_{ET}, instead of the strong exponential decay in k_{ET} characteristic for ET via superexchange.[13]

1.5. Structure-property relationships in long range ET

1.5.1. General Considerations

Figure 1.9 maps β-values measured for various conductive media relative to a perfect vacuum. Trends in the measured β-values generally correlate to the efficiency of communication among orbitals along a pathway. Additionally, several hypotheses have emerged concerning the wildly scattered β-values shown in Figure 1.9 for duplex DNA. Understanding precisely how the chemical features within an ET transfer system influence "conductivity," expressed as β, along a pathway is critical for predicting, controlling and harnessing long range ET both biological macromolecules and novel organic architectures.

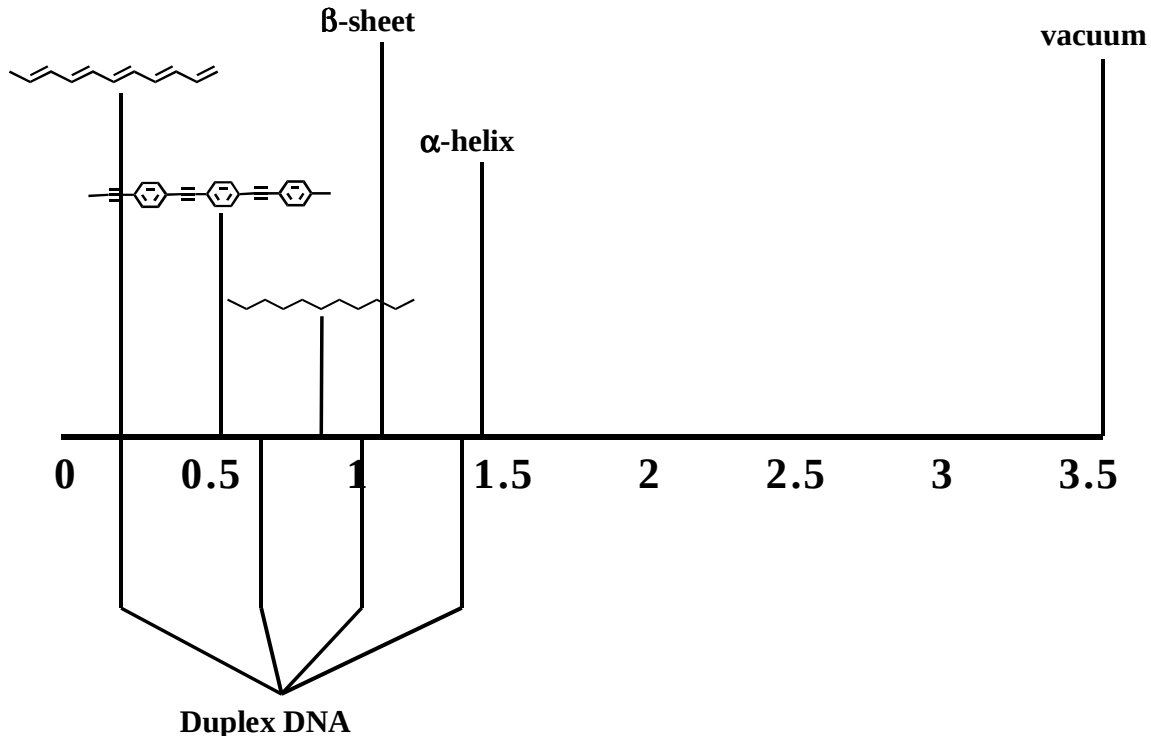

Figure 1.9. Experimental distance-decay constants, β, measured for various long range ET media.

1.5.2. Orbital hybridization

One of the most obvious parameters influencing long range ET in organic media is the hybridization of the intervening carbon atoms in a hydrocarbon chain. Systematic investigations of the structure-property relationships from this standpoint have been carried out in well-characterized crystalline self-assembled monolayers of ferrocene-terminated alkanethiols on gold.[24,27-37] Interfacial ET through a well-ordered alkanethiol monolayer occurs via a superexchange mechanism, and can be measured systematically as a function of alkane chain length. Chidsey and coworkers have calculated **β**-values using theory incorporating McConnell's superexchange model.[38] Their predictions agree reasonably well with experiment and reveal hybridization[39] and conformation-dependent **β**-values. Table 1.1 illustrates these trends.

Table 1-1. Exponential Decay Coefficients (β) reported by Chidsey et al. for interfacial ET through ferrocene-terminated alkanethiol self-assembled monolayers on gold.

hydrocarbon repeat unit	**β** ($Å^{-1}$)(Calc'd)	**β** ($Å^{-1}$)(Exptl)	Exptl error
trans ($-CH_2CH_2-$)	0.83	0.9[a]	0.1
($-C_6H_4C{\equiv}C-$) $\theta = 90^o$	0.97		
($-C_6H_4C{\equiv}C-$) θ = distribution	0.51	0.57[b,c]	0.02
($-C_6H_4C{\equiv}C-$) $\theta = 0^o$	0.39		
trans (-CH=CH-)	0.31	>0.2[d]	

[a] Reference 24, 27-37. [b] Experimental torsion angle (θ) distribution s unquantified, best correlation for uniform distribution. [c] Reference 38. [d] Reference 39.

1.5.3. Protein secondary structure

Overview

In proteins, the through-bond ET pathways connecting donor to acceptor are not well ordered crystalline hydrocarbon media. Rather, they are intricate three-dimensional networks of amino acid residues. Nevertheless, some simple structure-property relationships exist and have been employed successfully in theoretical models for predicting β-values in proteins.

Tunneling Pathway Model

In 1991, Beretan and coworkers published on a landmark electron-tunneling pathway model.[40] The key feature of this model was the incorporation of non-bonded and hydrogen-bonded units in through-bond ET pathways. Even more important was the recognition that electronic coupling over a hydrogen bond was worth only about ½ of the electronic coupling over a covalent bond. This rudimentary model, relating bond strength to microscopic "conductivity," was critical to the predictive power of the electron-tunneling pathway model.

Influence of protein secondary structure on β

The Beretan/Onuchic model provided a theoretical window into the center of the protein matrix. Previously, amino acid networks were viewed as a homogeneous continuum. The new tunneling model allowed for systematic consideration of structurally unique through-bond ET pathways in proteins. Predicting structure-property relationships

relating protein secondary structure to conductivity was the natural next step. The Beretan/Onuchic model predicted that conductivity through β-sheet pathways surpassed that for α-helix pathways of comparable lengths. This prediction was borne out experimentally in 1992.[41,42] Specifically, experiments revealed the **β**-value for a α-helix barrel and β-sheet pathway is 1.4 $Å^{-1}$ and 1.0 $Å^{-1}$ respectively. These represented typical **β**-values for long range ET in proteins.

1.5.4. In Duplex DNA

Overview

From the standpoint of biological ET, it was interesting to consider the relative conductivity of DNA and amino acid protein matrices. In 1993, Barton and coworkers measured an unprecedented **β**-value of <0.2 $Å^{-1}$ for donor-acceptor distances >35 Å in a donor-DNA-acceptor model system.[14] This observation opened up the possibility for a new paradigm- in which duplex DNA was viewed much like a highly conductive "molecular wire." Later studies performed on similar model systems revealed much higher **β**-values- supporting that duplex DNA was only about as conducting as other biological superstructures. In Duplex DNA, **β**-values of ~0.65–1.0 $Å^{-1}$ are observed for duplex DNA versus **β**-values of ~1.0–1.5 $Å^{-1}$ for proteins.

Several explanations for the spread in **β**-values for donor-DNA-acceptor systems have arisen. Critics generally fall into two categories- those that consider DNA a highly conductive "molecular wire" and those that do not. The former rationalizes the scattered **β**-values by invoking a novel supramolecular structure-property relationship relating the orderliness of the base stacking to the conductivity of the duplex. The latter dismiss this notion citing that conflicting **β**-values reflect poor interpretation of experimental measurements. Both viewpoints are considered here.

Influence of base-stacking on β

Recently, Barton and coworkers reported on the discovery of a novel supramolecular structure-property relationship relating the efficiency of long range ET through duplex

DNA to the orderliness of the base-stack.[10,43] In another report, dramatic attenuation of β was observed upon introducing a poorly stacking base analog into the helical axis.[44] The influence of stacking interactions was offered as an explanation for wildly varying β-values calculated for donor-DNA-acceptor model systems over the past few years. The notion, if true, that DNA is essentially a molecular wire "gated" by disruptions in the π-bonded base stack has far-reaching implications for biological and supramolecular ET motifs.

Opponents of the "molecular wire" paradigm for duplex DNA model systems emphasize a lack of thorough understanding of the donor-DNA-acceptor models considered in the literature; resulting in apples to oranges comparisons. These researchers generally view duplex DNA as an insulator that is comparable to amino acid protein matrices; displaying a β ~1.0. One critical contributor to inconsistent β-values, in their viewpoint, is the varying influences that the donor-acceptor probe molecules have on the intrinsic electronics, energetics, and structure of duplex DNA. Barton recently demonstrated variation in β as a function of the redox potential of the intercalated probe molecule.[44] Recently, a comprehensive survey of the mechanistic models and methods relating to DNA "conductivity" appeared.[45] The newest theories for explaining DNA β-values are intricate and highly speculative at present. As this topic is highly controversial and involved, these ideas will not be explicitly outlined here.

Influence of base sequence on β

Meggars and coworkers recently reported yet another novel structure-property relationship relating the rate of hole transport to DNA base-pair sequence.[13] Here, the long range ET rate of a hole originating at an oxidized guanine base was measured. Long-distance ET over 2, 3 and 4 AT base pairs showed strong distance-dependence. (β = 0.7 $Å^{-1}$). Substitution of any one of the AT base pairs with a GC pair resulted in a significant increase in transport rate. (2 orders of magnitude)

This rate increase was reconciled by the authors by considering an alternative hopping mechanism, an alternative to through-bond superexchange mechanistic pathway. A

two-step hopping ET process was considered - whereby the hole hops from donor to an intervening guanine base to acceptor site. The hopping mechanism, in contrast to a superexchange mechanism, is facilitated by low oxidation potentials of states along the pathway. In the Meggars work, donor and acceptor are both guanine derivatives. Therefore, oxidation potentials of intervening guanine residues met this criterion. This hopping mechanism is shut down when GC base pairs are completely omitted, leaving only high potential AT base pairs in the pathway. DNA sequence-specificity in long range ET rate and mechanistic pathway was a poignant demonstration of Nature's ability to prescribe the electronic properties of supramolecular systems with subtle changes in primary structure.

1.6. References and Notes

1)Marcus, R. A. *J. Chem. Phys.* **1956**, *24*, 966-978.

2)Marcus, R. A. *Disc. Faraday Soc.* **1960**, *29*, 21-31.

3)Marcus, R. A. *J. Chem. Phys.* **1965**, *43*, 679-701.

4)Hopfield, J. J. *Proc. Natl. Acad. Sci.* **1974**, *71*, 3640-3644.

5)Moser, C. C.; Keske, J. M.; Warneke, K.; Farid, R. S.; Dutton, P. L. *Nature* **1992**, *355*, 796-802.

6)McConnell, H. M. *J. Chem. Phys.* **1961**, *35*, 508-515.

7)The notion of superexchange was first conceived by Anderson to explain antiferrimagnetic coupling over long distances in organic media.

8)Marcus, R. A. *Ann. Rev. Phys. Chem.* **1964**, *15*, 155-196.

9)Weaver, M. J. *Chem. Rev.* **1992**, *92*, 463-480.

10)Kelley, S. O.; Holmlin, E. D.; Stemp, D. A.; Barton, J. K. *J. Am. Chem. Soc.* **1997**, *119*, 9861-9870.

11)Lewis, F. D.; Wu, T.; Zhang, Y.; Letsinger, R. L.; Greenfield, S. R.; Wasielewski, M. R. *Science* **1997**, *277*, 673-676.

12)Lewis, F. D.; Letsinger, R. L. **1998**, *3*, 215-221.

13)Meggers, E.; Michel-Beyerle, M. E.; Giese, B. *J. Am. Chem. Soc.* **1998**, *1200*, 12950-12955.

14)Murphy, C. J.; Arkin, M. R.; Jenkins, N. D.; Ghatlia, N. D.; Bossman, S. H.; Turro, N. J.; Barton, J. K. *Science* **1993**, *262*, 1025-1029.

15)Netzel, T. L. *JBIC* **1998**, *3*, 210-214.

16)Priyadadarshy, S.; Risser, S. M.; Beretan, D. N. *JBIC* **1998**, *3*, 196-200.

17)Ratner, M. *Nature* **1999**, *397*, 480-481.

18)Taubes, G. *Science* **1997**, *275*, 1421.

19)Turro, N. J.; Barton, J. K. *JBIC* **1998**, *3*, 201-209.

20)Miller, J. R.; Beitz, J. V. *J. Chem. Phys.* **1979**, *74*, 6476.

21)Miller, J. R.; Beitz, J. V.; Huddleston, R. K. *J. Am. Chem. Soc.* **1981**, *106*, 5057.

22)Mooney, W. F. *private communication* .

23)Miller, L. T.; Calcaterra, G. L.; Closs, G. L. *J. Am. Chem. Soc.* **1984**, 3047.

24)Closs, G. L.; Calcaterra, N. J.; Green, N. J.; Penfield, J. R.; Miller, J. R. *J. Chem. Phys.* **1986**, *90*, 3673.

25)Calcaterra, L. T.; Closs, G. L.; R., M. J. *J. Am. Chem. Soc.* **1983**, *105*, 670.

26)Closs, G. L.; Miller, J. R. *Science* **1988**, *240*, 441-447.

27)Smalley, J. F.; Feldberg, S. W.; Chidsey, C. E. D.; Linford, M. R.; Newton, M. D.; Liu, Y.-P. *J. Phys. Chem.* **1995**, *99*, 13141.

28)Dubois, L. H.; Nuzzo, R. H. *Ann. Rev. Phys. Chem.* **1992**, *43*, 437.

29)Finklea, H. O.; Hanshew, D. D. *J. Am. Chem. Soc.* **1992**, *114*, 3173.

30)Creager, S. E. *private communication* .

31)Carter, M. T.; Rowe, G. K.; Richardson, J. N.; Tender, L. M.; Terill, R. H.; Murray, R. W. *J. Am. Chem. Soc.* **1995**, *117*, 2896.

32)Becka, A. M.; Miller, C. J. *J. Phys. Chem.* **1992**, *96*, 2657.

33)Xu, J. L., H. -L.; Zhang, Y. J. *J. Phys. Chem.* **1993**, *97*, 11497.

34)Yonemoto, E. H.; Schmel, R. H.; Hubig, S. M.; Riley, R. L.; Iverson, B. L.; Mallouk, T. E. *J. Am. Chem. Soc.* **1994**, *116*, 4786.

35)Johnson, M. D.; Miller, J. R.; Green, N. S.; Closs, G. L. *J. Phys. Chem.* **1989**, *93*, 1173.

36)Miller, J. R.; Closs, G. L. *J. Phys. Chem.* **1993**, *97*, 13042.

37)Li, T. T. T.; Weaver, M. J. *J. Am. Chem. Soc.* **1984**, *106*, 6107.

38)Sachs, S. B.; Dudek, S. P.; Hsung, R. P.; Sita, L. R.; Smalley, J. F.; Newton, M. D.; Feldberg, S. W.; Chidsey, C. E. D. *J. Am. Chem. Soc.* **1997**, *119*, 10563-10564.

39)Woitellier, S.; Launey, J. P.; Spangler, C. W. *Inorg. Chem.* **1989**, *28*, 273.

40)Beretan, D. N.; Betts, J. N.; Onuchic, J. N. *Science* **1991**, *252*, 1285.

41)Betts, J. N.; Beretan, D. N.; Onuchic, J. N. *J. Am. Chem. Soc.* **1992**, *114*, 4043-4046.

42)Onuchic, J. N.; Beretan, D. N.; Winkler, J. R.; Gray, H. B. *Ann. Rev. Biophys. Biomol. Struc.* **1992**, *21*, 349-377.

43)Kelley, S. O.; Jackson, N. M.; Hill, M. G.; Barton, J. K. *Angew. Chem. Int. Ed.* **1999**, *38*, 941-949.

44)Kelley, S. O.; Barton, J. K. *Science* **1999**, *283*, 375-381.

45)Wilson, E. K., *DNA Conductance Convergence* in C&E News; August 23, 1999; 77:34, **1999,** 43-48

CHAPTER 2

STRUCTURE-PROPERTY RELATIONSHIPS FOR ATTENUATION OF CHARGE TRANSFER KINETICS IN ALTERNATIVELY STIFF AND FLEXIBLE METALLO-DENDRIMERS

This work was done in close collaboration with Dr. Michael W. Hager. Additionally, the synthetic efforts of Dr. Kang Yi Chen and Mr. Brandon L. Parkhurst as well as resources from the Supercomputing Center of North Carolina (RTP, NC) impacted this work and are gratefully acknowledged.

This work was the subject of a publication, Gorman, C. B.; Smith, J. C.; Hager, M. W.; Parkhurst, B. L.; Sierzputowska-Gracz, H.; Haney, C. A. *J. Am. Chem. Soc.* **1999**, *in press*.

2.1. Introduction

The hyperbranched structure of dendrimers is now an increasingly precedented motif employed by researchers utilizing this architecture in applications such as molecular recognition[1-8] surface modification,[9-16] asymmetric synthesis[17-23] and small molecule encapsulation.[24-27] Metallodendrimers, in particular, have received attention as functional, supramolecular objects. Several modes of metal-incorporation into dendritic architectures have emerged. Herein, we have employed a redox-active inorganic iron-sulfur cluster as the dendrimer core. A "cluster encapsulation" motif, as such, offers control over the microenvironment surrounding the inorganic core.

Several encapsulation motifs specifically for redox-active core dendrimers have emerged as well. Design motifs have been conceived with an eye toward mimicking metallo-proteins,[28-32] demonstrating single-molecule information storage schemes[33] or investigating novel opto-electronic materials.[34] The metallodendrimers employed in this study are particularly relevant on two fronts: as metallo-protein analogues and as a prototype molecule in single-molecule information storage schemes.

In such a scheme, the presence or absence of single electrons on individual molecules encode binary information. This scheme would represent the smallest possible switch and nominally the way to implement the highest density memory.[35] To a chemist, this idea translates very naturally into the notion of an array of oxidized and reduced molecules. Placing oxidized molecules in close proximity to reduced molecules to create this ordered array invites rapid electron transfer between the "0"s and "1"s, scrambling information. Thus, molecular structure-property relationships that govern the rate of electron transfer between redox centers will be required to implement a one electron = one bit information storage scheme in a rational way.

2.2. Results and Discussion

2.2.1. $[Fe_4S_4\text{-}(Sdend)_4][Bu_4N]_2$ –Stiff and Flexible Metallo-Dendrimers

Flexible redox-active core dendrimers

We hypothesized that ligand structure has an important effect on electron transfer rate attenuation in the redox-core dendrimers prepared in our lab. Moreover, we predicted that this effect is likely due to the conformation that the rigid and flexible dendrimer molecules adopt. Previously, the Gorman Group has prepared and studied flexible and redox active, metal cluster core dendrimers to discern qualitatively the relative rate of electron transfer to/from encapsulated centers.[33,36] These dendrimers represent topologically well-defined architectures designed to isolate the redox state of the core — effectively attenuating the rate of electron transfer to/from the molecular center to some degree.

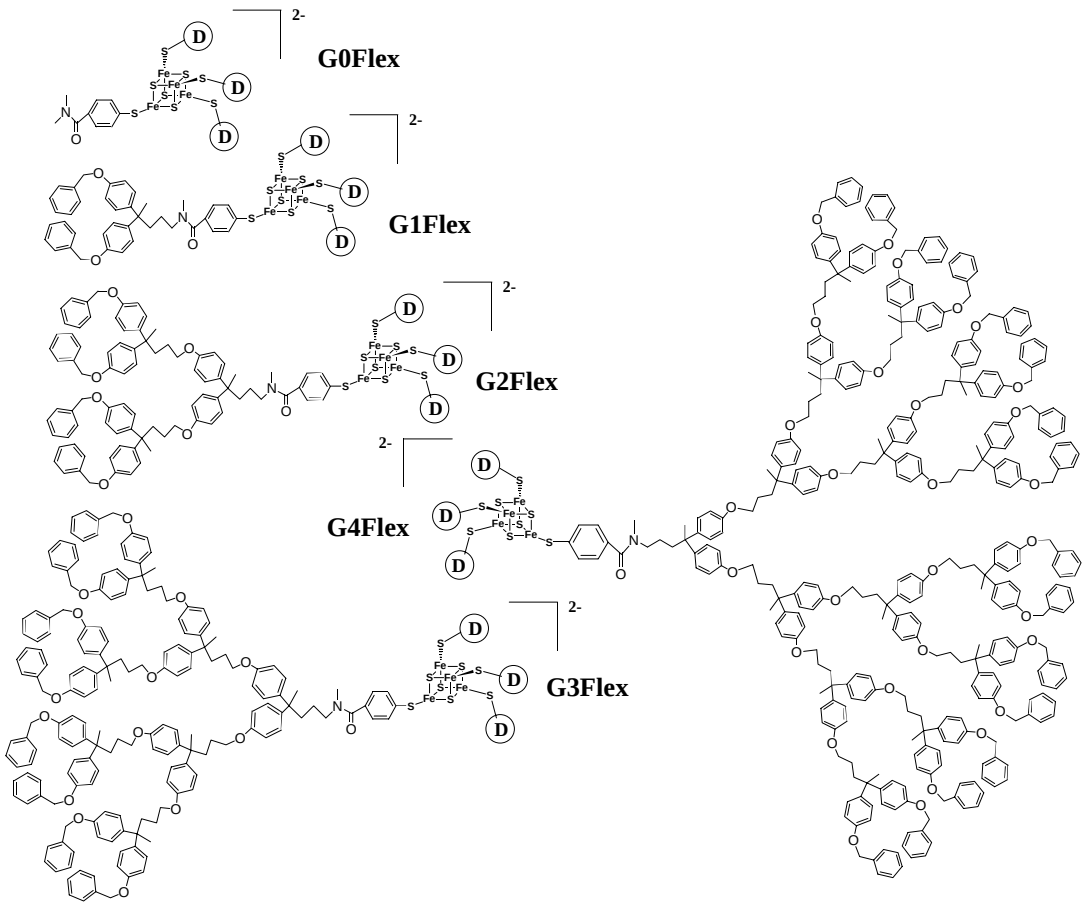

Figure 2.1. Flexible dendrimers considered in this study. One arm of each structure is drawn out fully. The three other arms are identical to the one shown but are abbreviated as a circled-D for ease of visualization.

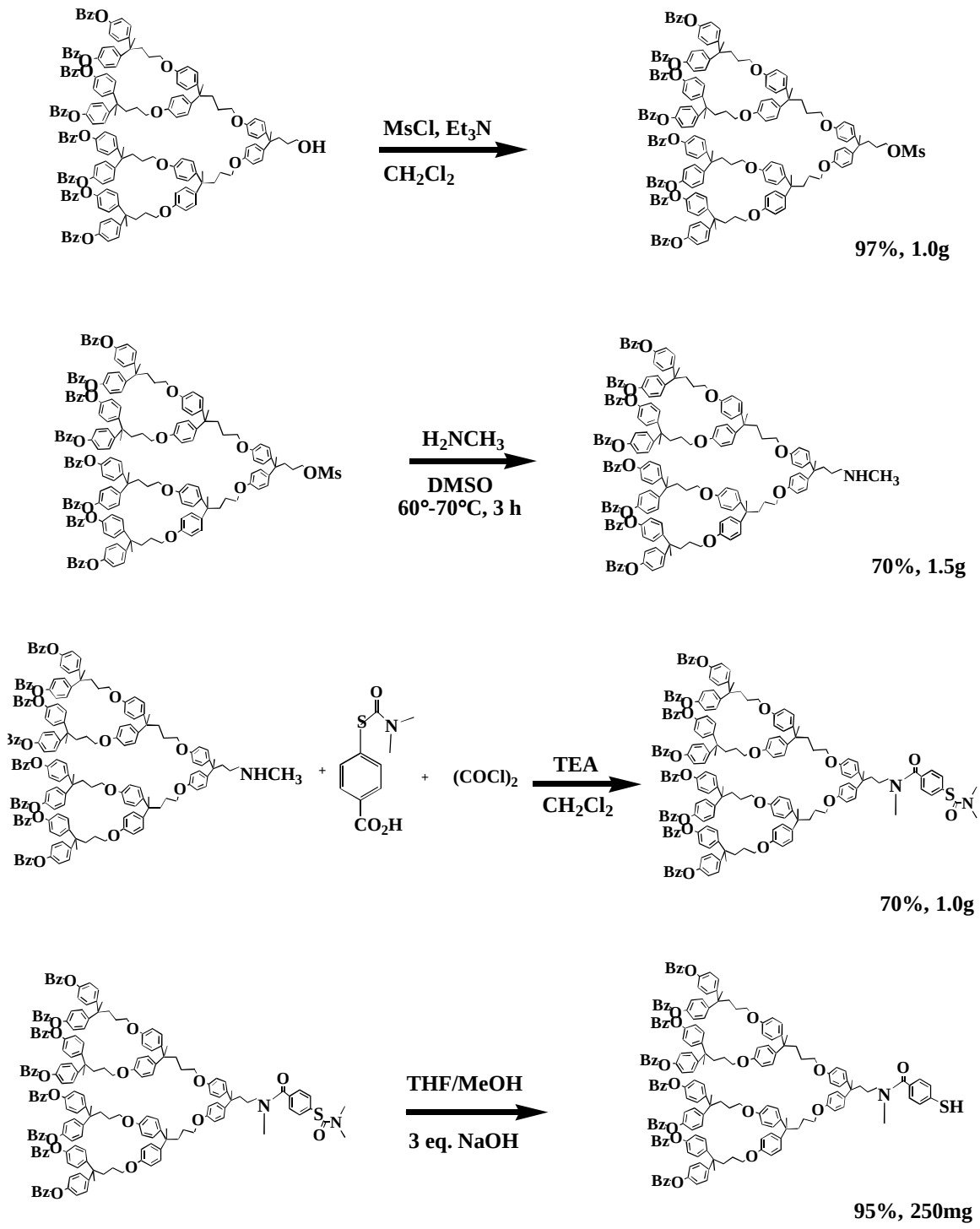

Scheme 2-1. Preparation of the generation 3 dendritic thiol. Purified yields are reported.

A synthetic protocol for the synthesis of dendrimers of the type $[Fe_4S_4\text{-}(S\text{-}$**GnFlex**$)_4][[Bu_4N]_2$ was worked out previously by Dr. Kang Yi Chen and Mr. B. L.

Parkhurst.[33, 36] Their generous donation of both materials and methods permitted further physical characterization and study. Sufficient quantities of each generation were available for physical study, with the exception of the generation 3 dendrimer.

Generation 3 was prepared and characterized by the author according to the previously outlined synthetic protocol. Preparation of the dendritic thiol ligand proceeded in high yield. (Scheme 2-1.) Subsequently, the dendritic thiol was used to produce the $[Fe_4S_4(S\text{-}\mathbf{GnFlex})_4][Bu_4N]_2$ in a ligand exchange reaction. (Scheme 2-2). Diagnostic Fermi Contact shifted aromatic proton resonances located adjacent to the $[Fe_4S_4]$ cluster indicated reaction completion during ligand exchange. The $[Fe_4S_4(S\text{-}G3Flex)_4][Bu_4N]_2$ product (85% isolated yield) was characterized by ^{1}H-NMR spectroscopy and elemental analysis.

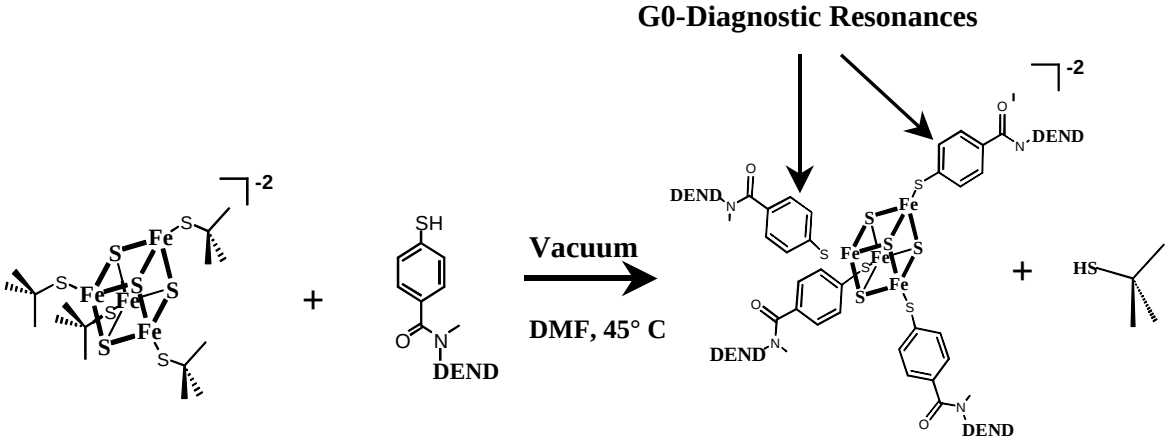

Scheme 2-2. Ligand exchange reaction where DEND represents 3 generations. The dianionic clusters each carry two tetrabutylammouniun cations.

Rigid redox-active core dendrimers

To compare with the flexible iron-sulfur core dendrimers discussed in Section 2.2.1, a series of iron-sulfur core dendrimers were prepared by Dr. Michael W. Hager. These

consisted of rigid phenylacetylene-type ligands. (Figure 2.2) The naming convention adopted here was chosen so that flexible and rigid molecules of the same generation have similar molecular weights. Dendrimers composed of this repeat unit had previously been reported by Moore et al.[37,38]

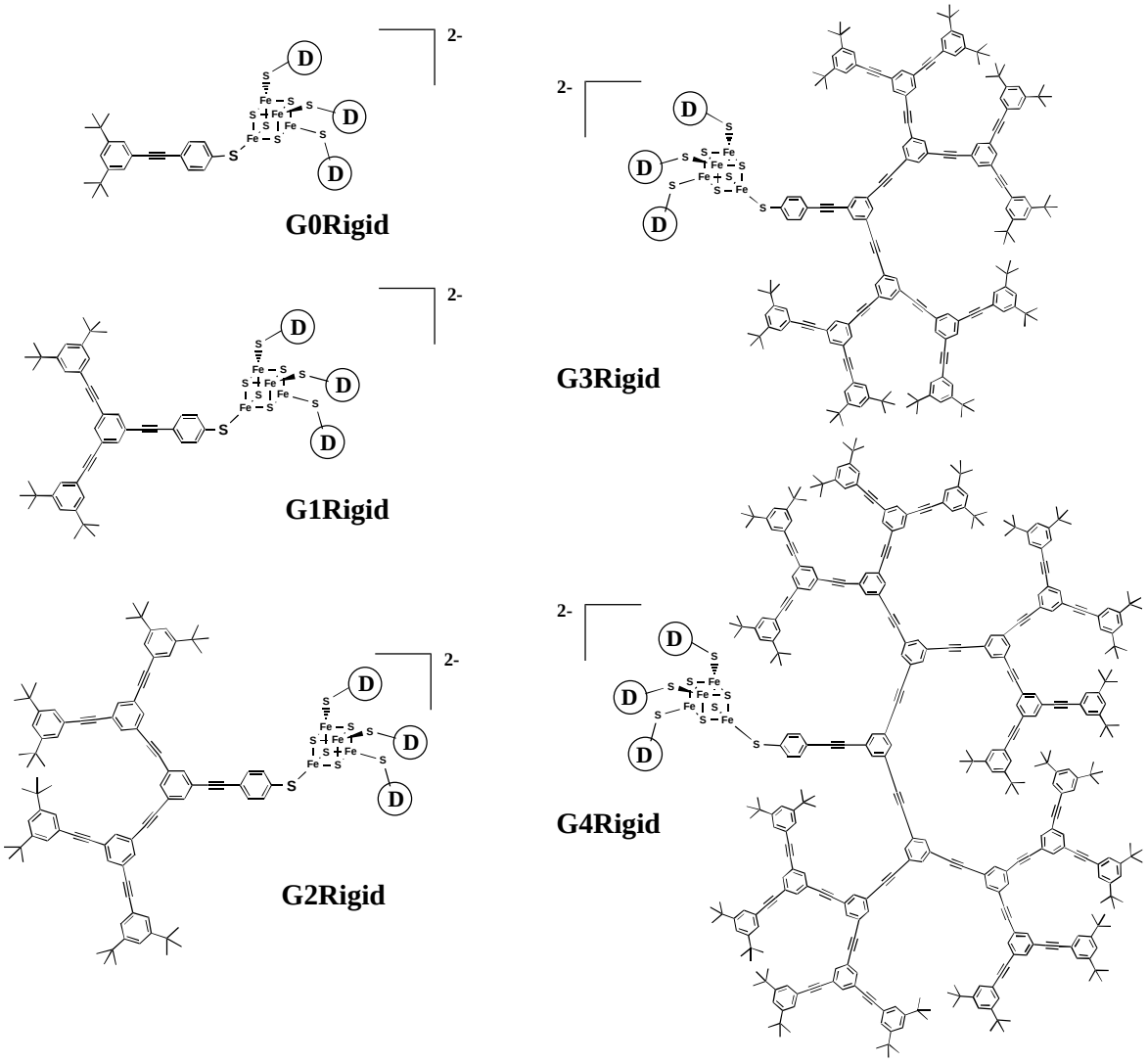

Figure 2.2. Rigid dendrimers prepared and considered in this study. One arm of each structure is drawn out fully. The three other arms are identical to the one shown but are abbreviated as a circled-D for ease of visualization.

2.2.2. Measuring Heterogeneous Electron Transfer Rate Constants for $[Fe_4S_4(Sdend)_4][Bu_4N]_2$ Metallo-Dendrimers

Measurement of Molecular Diffusion Coefficients

Diffusion coefficients of these dendrimers in dilute solution were determined using two complementary methods: by pulsed field gradient spin echo proton NMR (PFGSE - ^{1}H NMR) and electrochemically by chronoamperometry. (Table 2-1) With these values in hand, electrochemistry was used to determine heterogeneous electron transfer rate constants. These values in combination with an appropriate model provided an indication of molecular size. This estimated size was correlated with modeling results.

PFGSE-NMR relates the magnitude of a spin echo ($I(2\tau)$) as a function of an applied gradient magnetic field through the Stejskal-Tanner equation

$$I(2\tau) = I(0)e^{-\gamma^2 g^2 \delta^2 (\Delta - \delta/3) D} \qquad \text{(Equation 2.1)}$$

where γ is the magnetogyric ratio and δ denotes the duration of the magnetic field gradient pulses of amplitude *g* separated by a time interval Δ. The results of these experiments are shown in Figure 2.3.

PFGSE-NMR had been used previously by Newkome and Johnson[39,40] and Ihre et al.[41] to determine diffusion coefficients and hydrodynamic radii of dendrimers. For non-interacting objects diffusing in a medium of viscosity η, the hydrodynamic radius is given by the Stokes-Einstein equation

$$R_H = k_b T / 6\pi\eta D \qquad \text{(Equation 2.2)}$$

where k_b is Boltzmann's constant, T is the temperature, and D is the experimental molecular diffusion coefficient. Ihre et al. found a good correlation between measured and estimated radii for such dendrimers assuming a hard-sphere model. We found such correlations to be very solvent and molecule dependent as discussed in Section 2.4.

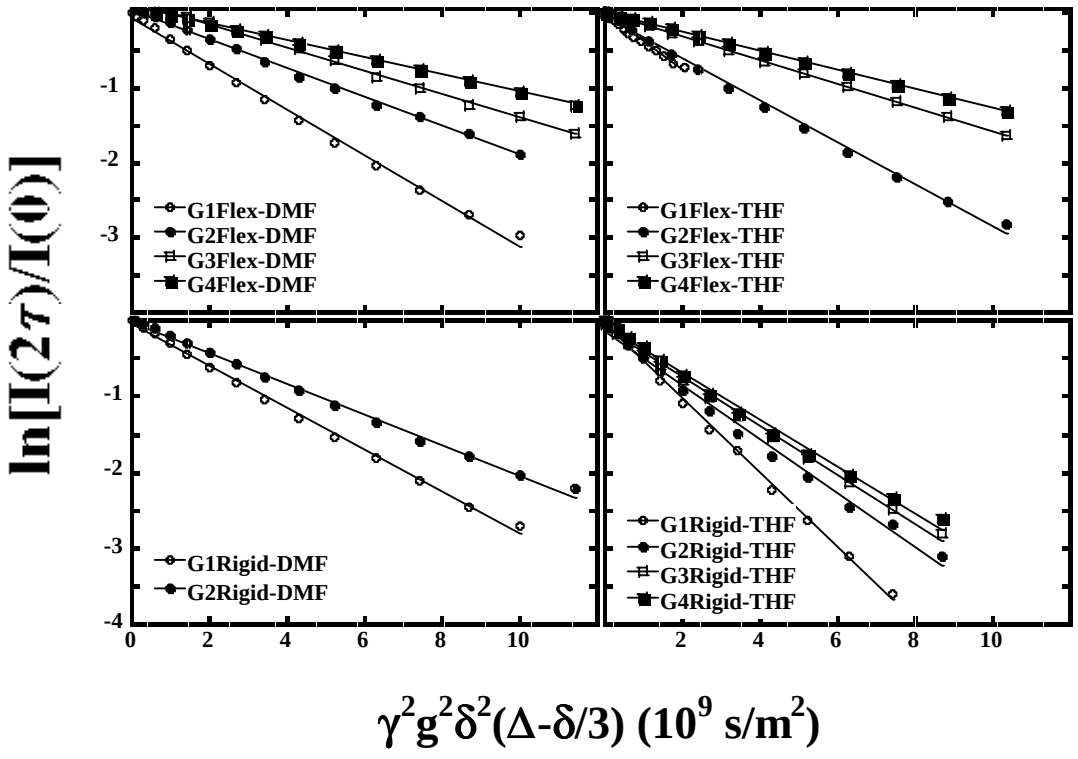

Figure 2.3. Stejskal-Tanner Plots for $[Fe_4S_4\text{-}(S\text{-}Dend)_4][Bu_4N]_2$ –Stiff and Flexible Metallo-Dendrimers.

To our knowledge, quantitative electrochemical techniques have been used only in one example to obtain diffusion information for redox-active dendrimers. In this case, Cardona and Kaifer[31] used a digital simulation of cyclic voltammetric data to obtain this value, the heterogeneous electron transfer rate constant (k) and the transfer coefficient (α). We chose to use chronoamperometry as this technique requires a diffusion coefficient as the only free parameter in a fit of these data.

Diffusion coefficients could also be obtained using any of several electrochemical techniques. The technique chosen here was chronoamperometry. Iron-sulfur core dendrimers have a quasi-reversible reduction from the dianionic to trianionic forms. Upon a potential step from well positive to well negative of this reduction potential, the current versus time response of any reversible or quasi-reversible system can be described by the Cottrell equation[28,29]

$$i(t) = \frac{nFAD^{1/2}C}{\pi^{1/2}t^{1/2}} \qquad \text{(Equation 2.3)}$$

where n is the number of electrons transferred (n = 1 here), F is Faraday's constant, A is the electrode area, C is the bulk solution concentration and t is time after the step. For the molecules under study here, the flexible dendrimers up to **G3Flex** in size and the rigid dendrimers **G1Rigid** and **G2Rigid** had quasi-reversible electrochemical behavior in DMF solution and were thus amenable to study by this technique. To our knowledge, quantitative electrochemical techniques have been used only in one example to obtain diffusion information for redox-active dendrimers. In this case, Cardona and Kaifer[30] used a digital simulation of cyclic voltammetric data to obtain this value, the heterogeneous electron transfer rate constant (k) and the transfer coefficient (α). We chose to use chronoamperometry as this technique requires a diffusion coefficient as the only free parameter in a fit of these data. The results of chronoamperometry experiments are illustrated in Figure 2.4 and in Table 2-1.

Several trends were noted in the data shown in Table 2-1. As would be expected, a decrease in diffusion coefficient was found with increasing molecular size within a given series of molecules. In comparing the flexible series with the rigid series of metallodendrimers, the most notable contrast in diffusion behavior was observed as solvent was varied. As THF and DMF have different viscosities, diffusion coefficients determined in these two solvents are not comparable. Thus, hydrodynamic radii were calculated using Equation 2.2 and these were compared.

The flexible series of dendrimers displayed a large change in hydrodynamic radius in different solvents. Specifically, these molecules appeared much larger in THF than in DMF, probably due to greater "solvent swelling" in the former solvent compared with the latter. Note that the data obtained in THF were at a tenfold lower concentration than those obtained in DMF. Initially, we were concerned about comparing these two sets of data because of this difference.

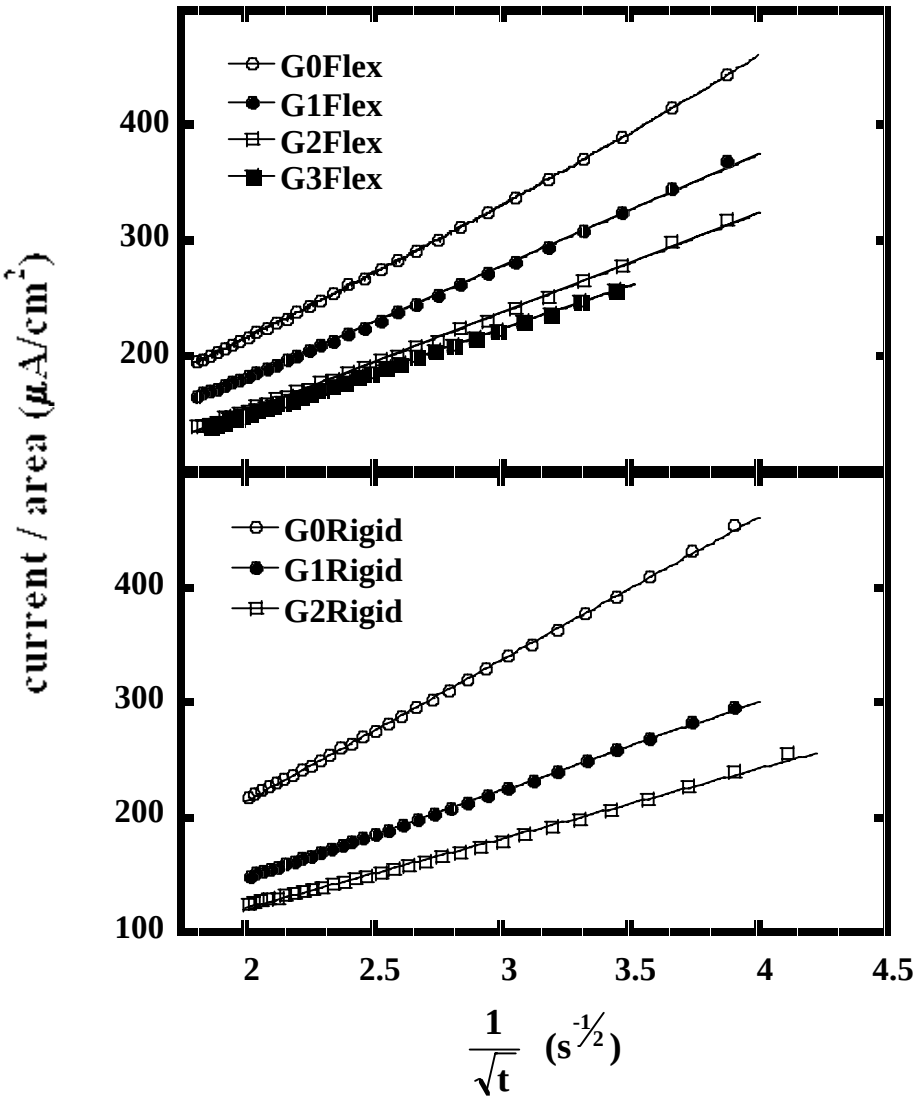

Figure 2.4. Cottrell plots for $[Fe_4S_4\text{-}(S\text{-}Dend)_4][Bu_4N]_2$ –Stiff and Flexible Metallodendrimers.

However, these solutions should all be dilute enough that intermolecular interactions are negligible. However, if concentration were an issue, a decrease in intermolecular interactions in the more dilute THF solutions would result in an increase in the apparent diffusion coefficient. This supposed increase in apparent diffusion coefficient would decrease the apparent hydrodynamic radius calculated. However, the hydrodynamic radii in THF were found to be greater than those in DMF. Thus, any concentration effect is apparently not a concern. The data obtained by chronoamperometry suggest a further

decrease in hydrodynamic radius in DMF/electrolyte (100mM tetraethylammonium tetrafluoroborate, TEAF) solution compared to the neat DMF solution used for the PFGSE experiments. The increase in ionic strength alone will make the solution slightly more viscous. This viscosity increase would increase the apparent hydrodynamic radius as per equation 2.2. However, since the opposite was observed, these data suggest that these molecules further contract in DMF solution containing electrolyte. This postulated size difference may be a factor in the difference in effective reduction/oxidation kinetics of these molecules in different solvents.

Table 2-1. Diffusion Coefficients, D_o(cm^2/s) obtained from Pulsed Field Gradient Spin Echo NMR Spectroscopy (PFGSE) and Chronoamperometry (CA) and corresponding Stokes-Einstein Radius, R_H.

Structure	D_o (x 10^6 cm^2/s) PFGSE 1mM DMF [a]	R_H (Å) DMF [ab]	D_o (x 10^6 cm^2/s) PFGSE 0.1mM THF [a]	R_H (Å) THF [ab]	D_o (x 10^6 cm^2/s) CA 1mM DMF [a]	R_H (Å) DMF [ab]	Molecular Model Rg (Å)[e]
G1Flex	3.10 (0.07)	8.80 (0.11)	3.76 (0.20)	12.63 (0.61)	3.47 (0.16)	7.85 (0.37)	7.75
G2Flex	2.06 (0.22)	13.22 (0.91)	2.83 (0.20)	16.76 (1.09)	2.51 (0.38)	10.86 (1.94)	10.84
G3Flex	1.69 (0.20)	16.04 (1.23)	1.86 (0.48)	25.48 (5.22)	2.02 (0.49)	13.49 (4.02)	13.07
G4Flex	1.37 (0.38)	19.93 (3.99)	1.33 (0.08)	35.80 (0.10)	---- [c]	---- [c]	16.92
G1Rigid	2.72 (0.12)	10.04 (0.23)	4.84 (0.09)	9.81 (0.18)	2.17 (0.46)	12.56 (3.36)	15.02
G2Rigid	2.11 (0.05)	12.92 (0.19)	3.88 (0.40)	12.22 (1.13)	1.89 (0.37)	14.43 (3.50)	18.70
G3Rigid	---- [d]	---- [d]	3.28 (0.58)	14.46 (2.16)	---- [d]	---- [d]	20.89
G4Rigid	---- [d]	---- [d]	3.01 (0.22)	15.78 (1.09)	---- [d]	---- [d]	24.84

[a]Values in parentheses represent the magnitude of the 90% confidence intervals of these values. [b]Calculated from equation 2.2. [c]Irreversible electrochemistry prevented this value from being determined. [d]Insufficiently soluble. [e]Average of all structures within a Boltzmann cutoff (10 kcal/mol @ 500 K) of the lowest energy structure found in the conformational search.

In contrast to the above results, the rigid dendrimers showed little change in computed hydrodynamic radius as a function of solvent. This observation indicates that these molecules do not change substantially in size or shape, consistent with the rigid and thus "shape persistent"[42-44] nature of these molecules.

When considering the flexible dendrimers in the most compact form studied (i.e., in DMF/electrolyte), the computed hydrodynamic radii of the these molecules correlated well with the radii of gyration calculated using molecular dynamics simulations. This correlation should exist only if these molecules were behaving as hard spheres in which the interaction with solvent was minimal. In contrast, the rigid dendrimers did not exhibit this correlation, suggesting a non-spherical/non-compact shape for these molecules. Shape rather than degree of solvation is suggested to be most important in interpreting the diffusion data for the rigid dendrimers as little change in molecular size was observed in different solvents. These conclusions also will be shown to be consistent with simulations described in Sections 2.4 and 2.5.

Determination of heterogeneous electron transfer rate constant, k

The general question as to how macromolecular architectures quantitatively affect electron transfer to/from incorporated redox species has not been probed in detail. As described in Section 2.1, the quantitative electrochemical behavior of dendrons containing focal, redox-active (ferrocenyl) groups has been described.[31] Several redox-active porphyrin-core and metal tris-bipyridine-core dendrimers have been prepared and their redox potentials determined by cyclic voltammetry,[28,29,32,45-58] but no quantitative electrochemistry experiments have been reported on these molecules to our knowledge.

To probe how the electron transfer rate of the redox-active core is affected by various dendritic architectures, heterogeneous electron transfer rate constants (k_0) were determined for these molecules. These determinations were made in two ways: (1) via a Nicholson analysis of the cyclic voltammograms (CVs) of these molecules taken at a number of scan rates and (2) by an iterative fit of their Osteryoung square wave voltammograms (OSWV) (Section 2.8 for details). The results of these experiments are shown in Table 2-2.

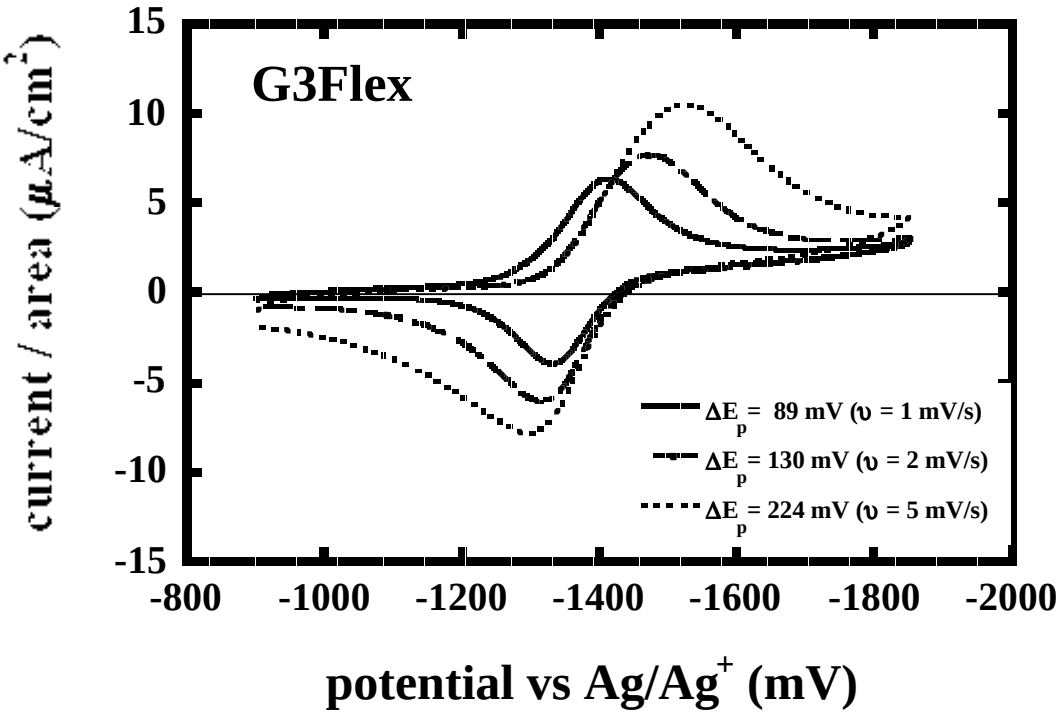

Figure 2.5. Cyclic voltammograms for millimolar samples of G3Flex in DMF electrolyte solution (100mM tetraethylammonium tetrafluoroborate, TEAF). Slow scan rates were necessary to obtain reversible electron transfer kinetics.

The Nicholson analysis of CVs is straightforward but becomes difficult as rate of electron transfer tends towards irreversible behavior. Under these conditions, the peak separation between the cathodic and anodic peaks increases and the peaks broaden, making it difficult to assign the exact applied bias for I_{pc} and I_{pa}. This behavior is illustrated in Figure 2.5 where the CVs of **G3Flex** are shown at 1, 2 and 4 mV/s scan rate, respectively. These data also illustrate the extent to which this experiment can be pushed — very slow scan rates were required to determine the value of k_0 for **G3Flex**. The electrochemical behavior of **G4Flex** was strictly irreversible. Thus the value of k_0 for this molecule could not be determined without a fit of the cyclic voltammetry data.

Cyclic voltammetry provided an indication as to whether electron transfer rates were measured under the condition that the species was behaving as a freely diffusing redox probe. The kinetic analyses used here assume this behavior. Dendrimer adsorption to

electrodes has been observed previously[59] and is therefore a concern when macromolecular electrochemistry is performed. Plots of peak reductive current (from cyclic voltammetry) versus the square root of scan rate should be linear if the redox probe is freely diffusing. Indeed (Figure 2.6) this behavior is observed for the flexible dendrimers and in rigid dendrimers up to the second generation. However, with the molecule **G3Rigid**, a substantial deviation from linearity was observed. This molecule was also observed to be much less soluble in DMF. The molecule **G4Rigid** was so insoluble in DMF that cyclic voltammetry results could not be obtained. Thus, due to this experimental limitation, quantitative determination of electron transfer rate constants of these larger rigid dendrimers was prohibited.

Table 2-2. Heterogeneous electron transfer rate constant (k_0), reduction potential ($E_{1/2}$) and α for the one electron redox couple $[Fe_4S_4(S\text{-Dend})_4]^{2-/3-}$

Structure	k_0 (x 10^3 cm/s) CV[a]	$E_{1/2}$ (mV) CV[a]	k_0 (x 10^3 cm/s) OSWV[a]	$E_{1/2}$ (mV) OSWV[a]	α OSWV[a]
G0Flex	8.63 (0.83)	-1352 (3)	7.43 (1.31)	-1344 (4)	0.57 (0.07)
G1Flex	8.36 (0.89)	-1360 (6)	6.15 (0.64)	-1359 (9)	0.54 (0.06)
G2Flex	3.59 (0.33)	-1366 (10)	3.29 (0.44)	-1374 (13)	0.33 (0.01)
G3Flex	0.51 (0.22)	-1371 (19)	0.76 (0.03)	-1374 (28)	0.29 (0.05)
G4Flex	irrev.	irrev.	0.13 (0.06)	N. A.[b]	0.47 (0.01)
G0Rigid	8.95 (0.96)	-1354 (4)	6.24 (0.59)	-1351 (5)	0.56 (0.08)
G1Rigid	5.13 (1.11)	-1323 (16)	4.12 (0.78)	-1322 (14)	0.54 (0.04)
G2Rigid	2.13 (0.36)	-1329 (13)	2.35 (0.09)	-1324 (9)	0.37 (0.03)

[a]The magnitude of the 90% confidence interval is indicated in parentheses. [b]Not determined in a fit of an irreversible wave.

In a mixture of 25 % pyridine and 75% DMF (v/v), the molecule **G3Rigid** was soluble enough for electrochemistry and could be compared to **G3Flex**. The results of cyclic voltammetry (Figure 2.7) indicate that although **G3Flex** displays quasi-reversible behavior, the behavior of **G3Rigid** is irreversible. This result indicates that electron transfer is at least an order of magnitude slower for **G3Rigid** than for **G3Flex** under these conditions. Rate constants were not calculated in these cases due to concerns about error associated with uncompensated solution resistance in this lower dielectric solvent system.

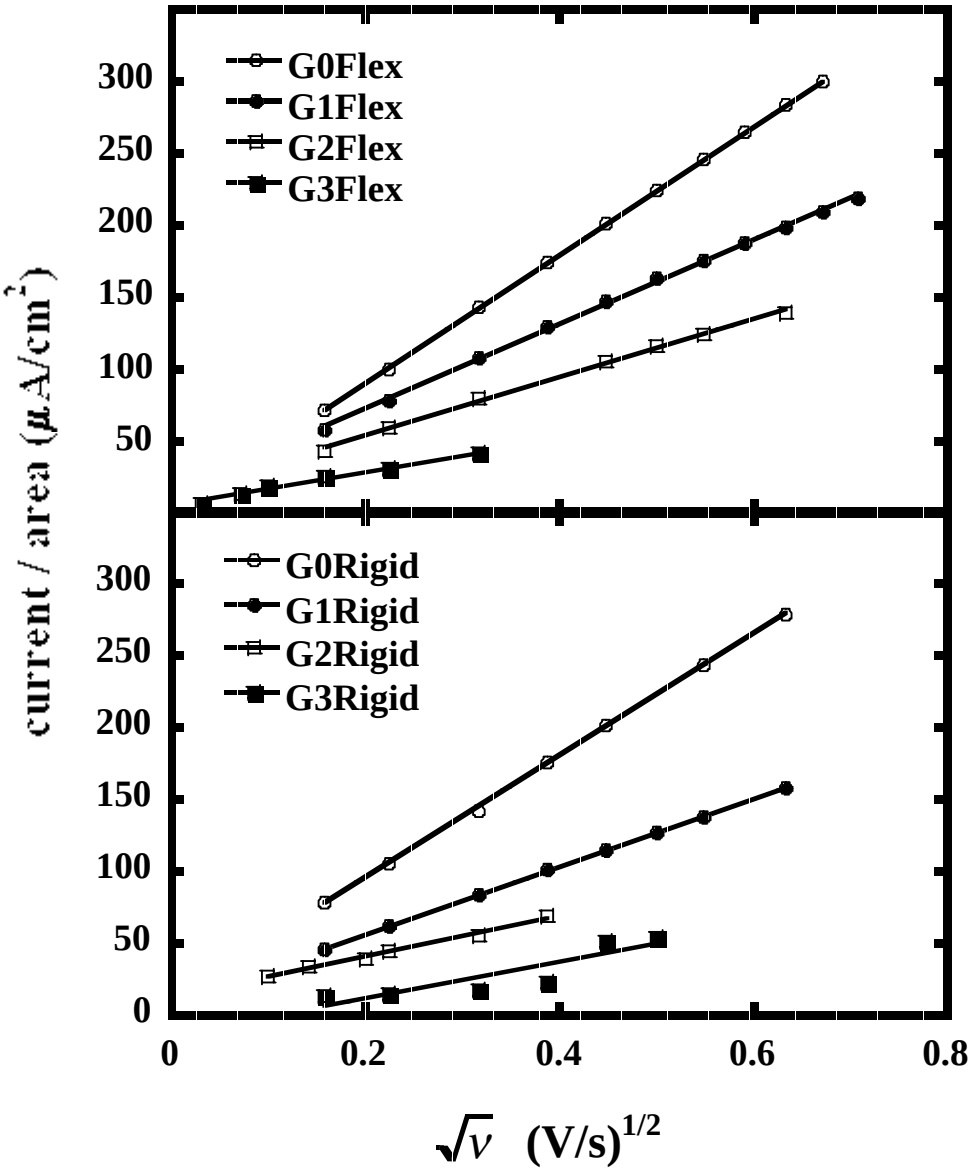

Figure 2.6. Plots of peak reductive current (from cyclic voltammetry) versus the square root of scan rate for $[Fe_4S_4\text{-}(S\text{-}Dend)_4][Bu_4N]_2$ –Stiff and Flexible Metallodendrimers. All voltammograms were performed with 1 mM sample concentration except G3Rigid which was performed at 0.5 mM.

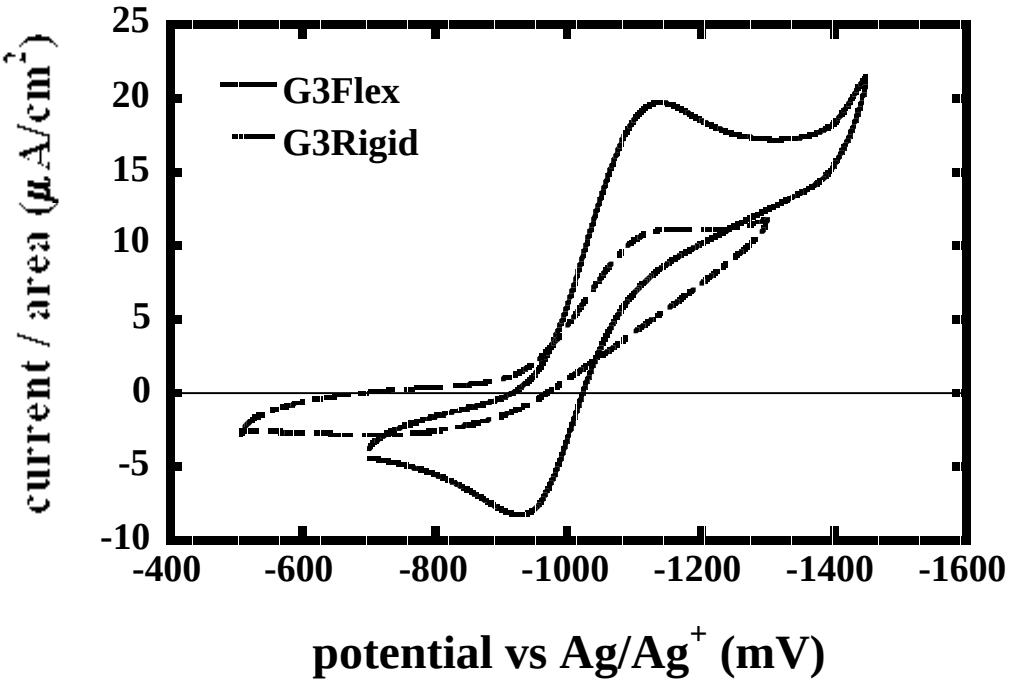

Figure 2.7. CVs taken in 25% pyridine/75% DMF (v/v) at a scan rate of 2 mV/s illustrating irreversible electron transfer for G3Rigid but still quasi-reversible electron transfer for G3Flex.

The most confident measurements of electron transfer rates came from Osteryoung square wave voltammograms (Figure 2.8). These data were fit to obtain the data shown in Table 2-2. The behavior of **G4Flex** was fit to an irreversible model to obtain a rate constant.[60] The position of the current maximum moves from molecule to molecule and for **G4Flex,** it shifts substantially. This behavior is expected due to a change in electron transfer rate and does not reflect a large change in the thermodynamic redox potential.[60]

The change in thermodynamic redox potential in this series of molecules was, if anything, small. This result was initially surprising as investigations on porphyrin-core dendrimers concluded that a dendritic architecture could result in a large change in redox potential.[28] The redox potential of iron-sulfur clusters is rather sensitive to environmental changes.[61-63] This result suggests that these particular dendrimers attenuate electron transfer without substantially changing the local environment in which the redox species resides. This idea will be developed further in following sections.

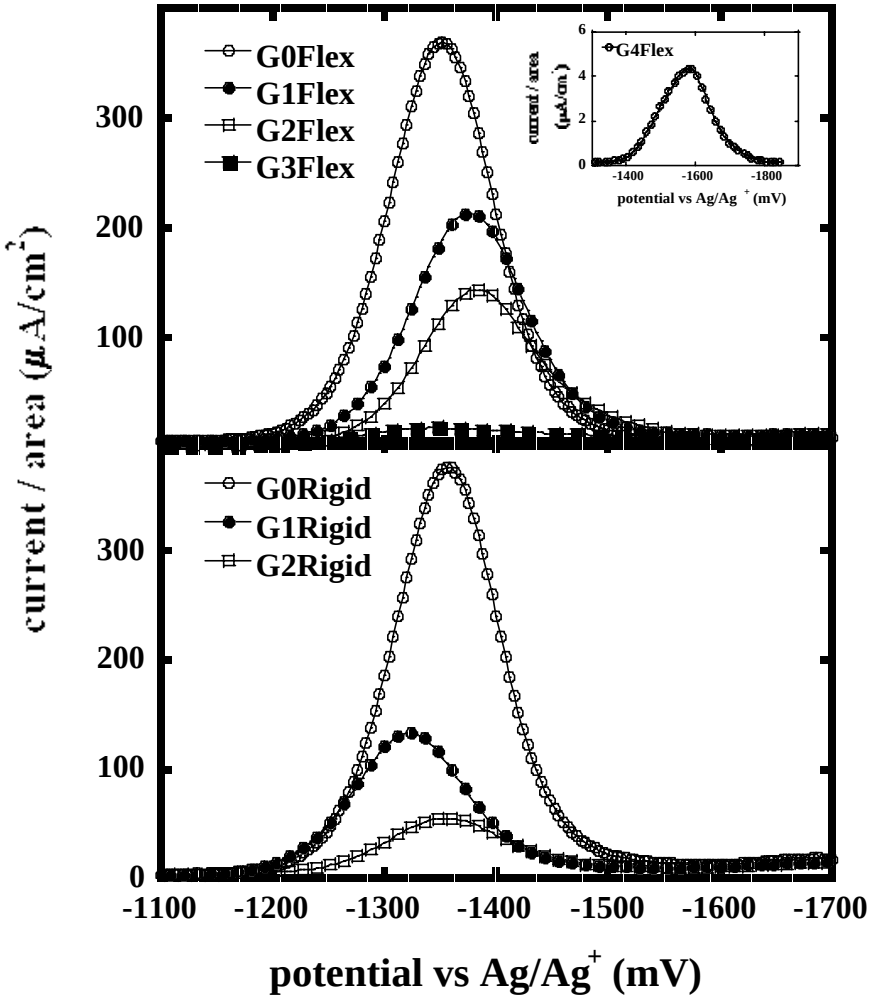

Figure 2.8. Osteryoung square wave voltammograms for $[Fe_4S_4$-(S-Dend)$_4][Bu_4N]_2$ –Stiff and Flexible Metallodendrimers. Vertical expansion of the voltammogram is shown for G4Flex. (Inset, top)

Several interesting changes were observed in electron transfer rate both as molecules of different molecular weight and as the rigid and flexible molecules were compared. Qualitative comparison of their cyclic voltammograms indicates attenuation of electron transfer. With increasing generation, the peak splitting increases and the magnitude of the peak current decreases. (Figure 2.9)

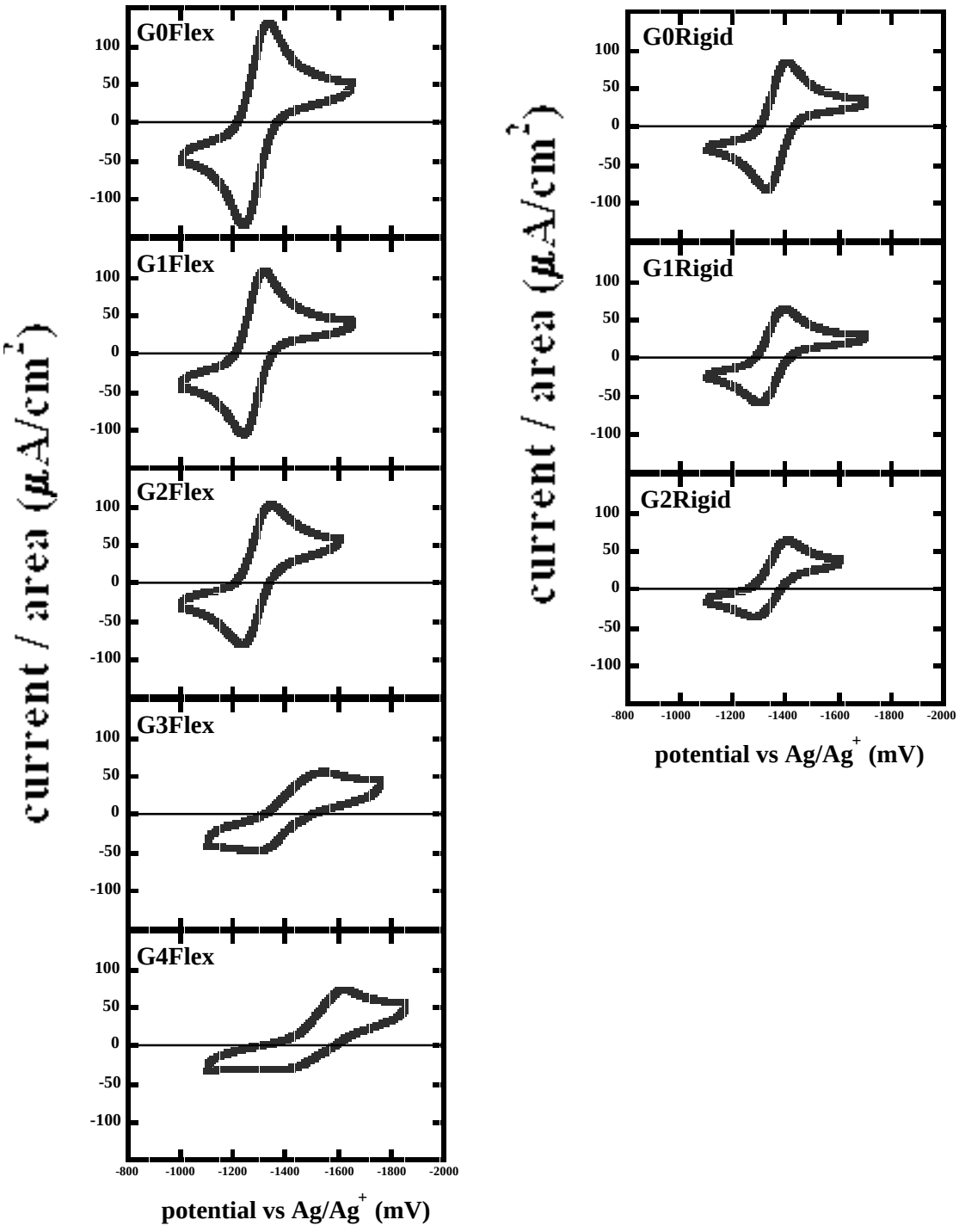

Figure 2.9. Cyclic voltammograms for $[Fe_4S_4\text{-}(S\text{-}Dend)_4][Bu_4N]_2$ –Stiff and Flexible Metallodendrimers. Millimolar samples of dendrimer in DMF/electrolyte solution (100mM-tetraethylammonium tetrafluoroborate, TEAF) were used. Scan rates shown at 100mV/s.

Figure 2.10 graphically illustrates the attenuation in heterogeneous electron transfer rate as a function of molecular size and type. Since the two series of molecules are dissimilar in structure, molecular weight was chosen as the variable by which to compare them. Arguably, this parameter is most significant from the standpoint of molecular design as it represents a scale of synthetic effort. Although fewer data are available to assess quantitatively the attenuation in the rigid series of dendrimers, the rigid molecules clearly have lower electron transfer rates than the flexible molecules for a given molecular weight. Clearly, there is an architectural difference that is important in governing this variance. Thus, it was of interest to generate models of the dendrimers in an effort to shed some light on structural differences in these molecules and to rationalize these differences in electron transfer rate.

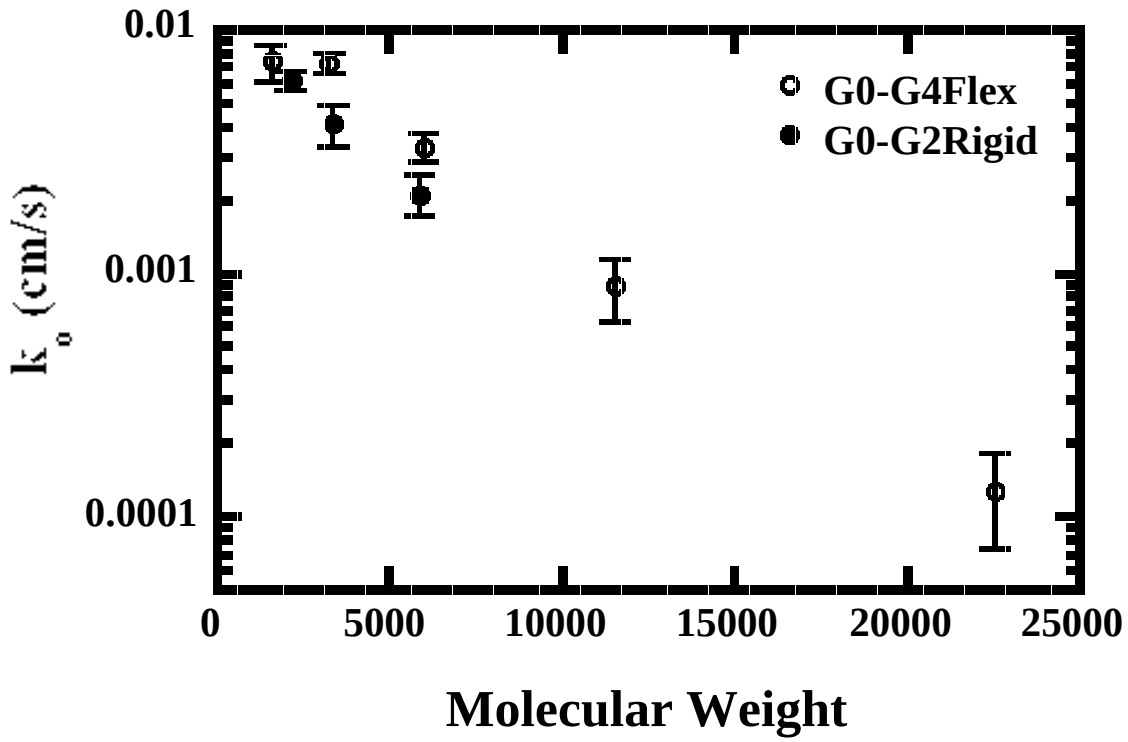

Figure 2.10. Electron transfer rate constants for $[Fe_4S_4$-(S-Dend)$_4][Bu_4N]_2$ –Stiff and Flexible Metallodendrimers as a function of molecular size and type.

2.2.3. Illustration of Dendrimer Conformation with Molecular Structures Derived from Computational Conformational Searching

Dendrimers are conformationally complex and no structural data such as crystal structures are available that indicate minimum energy conformations for these molecules. Thus, the most important task in conducting a realistic simulation of dendrimer structure is finding the lowest energy minima in the potential space of such molecules. Thus, we turned to the technique of conformational searching in an attempt to generate a family of structures representative of the low energy conformations of the dendrimers.[64-66] In performing these computations, we stress their correspondence with available experimental data and chemical intuition. Thus, one can regard these results as a proposed model of dendrimer conformation.

Our first interest in evaluating the results of these simulations was to determine the relative correlation between these results and available experimental data. The radii of gyration of the models obtained from these simulations are compared with the hydrodynamic radii obtained from NMR and electrochemistry experiments (Table 2-1). A good correlation is expected if the model is reasonably spherical in shape and of the same size as the molecule (i.e., a non-interacting hard-sphere model). In the case of the flexible dendrimers, an excellent correlation between computationally determined radii of gyration and electrochemically-determined hydrodynamic radii was found. This suggests that vacuum models can be reasonable approximations of the molecules investigated in DMF electrolyte solution.

Poorer correlations were found for the flexible models with molecules in solution (particularly THF) suggesting solvent swelling in this solvent. Poor correlation was found between measured hydrodynamic radii and computed radii of gyration for the rigid molecules. This observation is not surprising given the open, non-spherical shape of the rigid molecules (Figure 2.13). Unfortunately, there is no straightforward way to calculate a hydrodynamic radius from these models, so no further correlations can be made in this regard.

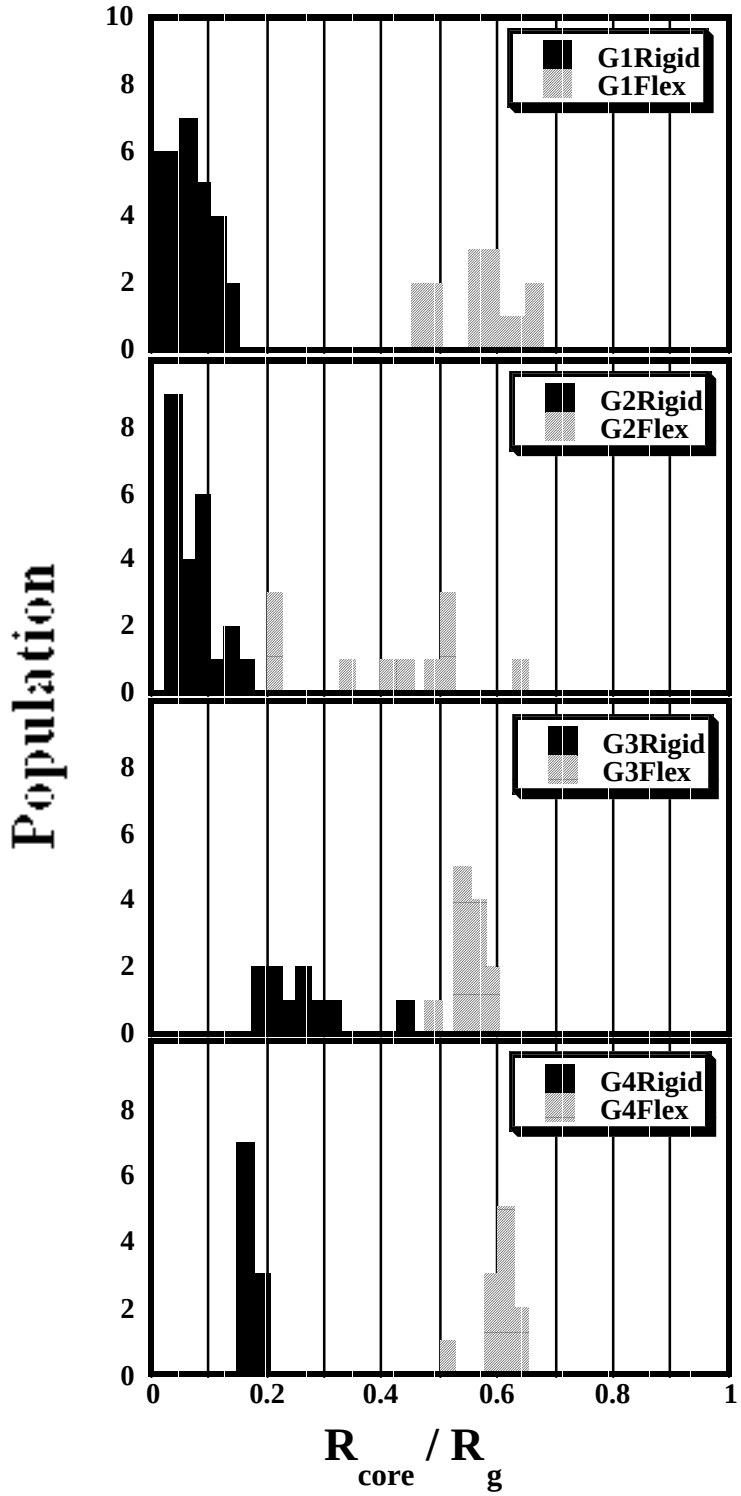

Figure 2.11. Relative occurrence of conformers correlated with relative core offset. R_{core} refers to the distance between the center of the cubic core and the center of mass of the molecule. R_g refers to the Radius of Gyration of the molecular model. Bars in each histogram represent the number of structures found in a conformation search that were within a Boltzmann cutoff (10 kcal/mol) of the minimum energy structure found.

The most significant correlation between flexible and rigid dendrimers is the relative position of the iron-sulfur core in each type of dendrimer model. The number of low energy conformers within a Boltzmann cutoff of 10 kcal/mol @500K of the lowest energy conformer were correlated with the relative offset of the core. (Figure 2.11) An offset of zero would find the core at the center of mass of the molecule. An offset of one would find the core at the edge of the molecule. One can see a substantially more offset core in all of the flexible models compared with all of the rigid models. In pictorial representations of the lowest energy conformations of **G4Rigid** and **G4Flex** (Figure 2.13) the core is observed to be very centrally located in the rigid molecule but virtually at the molecular edge in the flexible molecule.

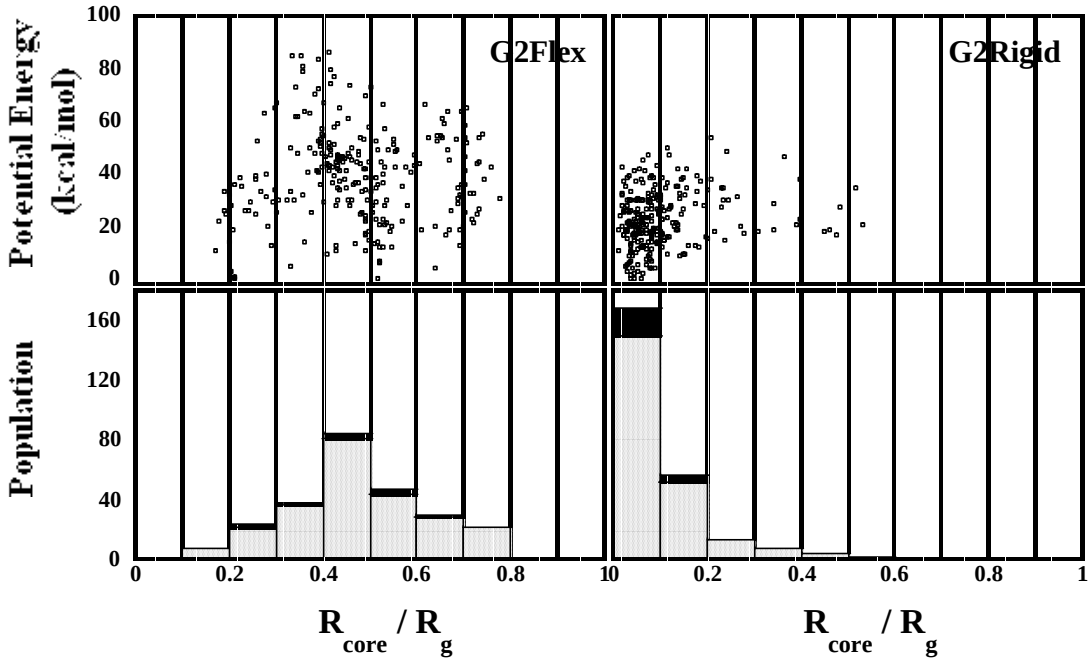

Figure 2.12. Correlation of relative potential energy with geometry in a set of 250 minimum energy structures found during conformational searches of models of G2Rigid and G2Flex. R_{core} refers to the distance between the center of the cubic core and the center of mass of the molecule. R_g refers to the Radius of Gyration of the molecular model. Dark bars in each histogram highlight structures within a Boltzmann cutoff (10 kcal/mol) of the minimum energy structure found.

Significant changes in the core position within the flexible dendrimers probably occur on the time scale of the electrochemical experiment and are thus important to the encapsulation behavior observed here. This idea is borne out by the data shown in Figure 2.12. Considering all the structures found during the conformational search, **G2Flex** is found in a wider range of geometries than is **G2Rigid**. As indicated in Figure 2.11, this trend persists for the other generations of molecules. Although room temperature molecular dynamics simulations are restricted, practically, to nanosecond and shorter time scales, dynamics on longer time scales have been inferred using high temperature simulations.[52] In the case of the conformational search performed here, periodic minimization "grounds" the conformations considered, insuring that the high temperature dynamics do not proffer unrealistic geometries. The idea that the flexible dendrimers have a much more mobile core than do the rigid dendrimers is intuitive: the rigid dendrimers are plausibly much more shape persistent[42-44,68] and thus do not change shape nearly as much over time. Thus, they provide a system for encapsulation that is more ideal from both a static and dynamic viewpoint.

2.2.4. Relationship between Molecular Structure and Electron Transfer Rate Attenuation

Correlation of the results of these simulations with the electron transfer rate data suggest the possibility that a component of electron transfer in the flexible dendrimers occurs on asymmetric conformers such as those shown in Figure 2.13. In contrast, in the stiff dendrimers, the redox core is held much more rigidly in the center of the molecule. This observation seems to rationalize the difference in relative electron transfer rates between rigid and flexible dendrimers. The flexible dendrimers effectively encapsulate the molecular core less than the rigid dendrimers. Note that the open structure of the **G4Rigid** model in Figure 2.13 argues against the notion that access of the counterion to the redox unit is rate-limiting.

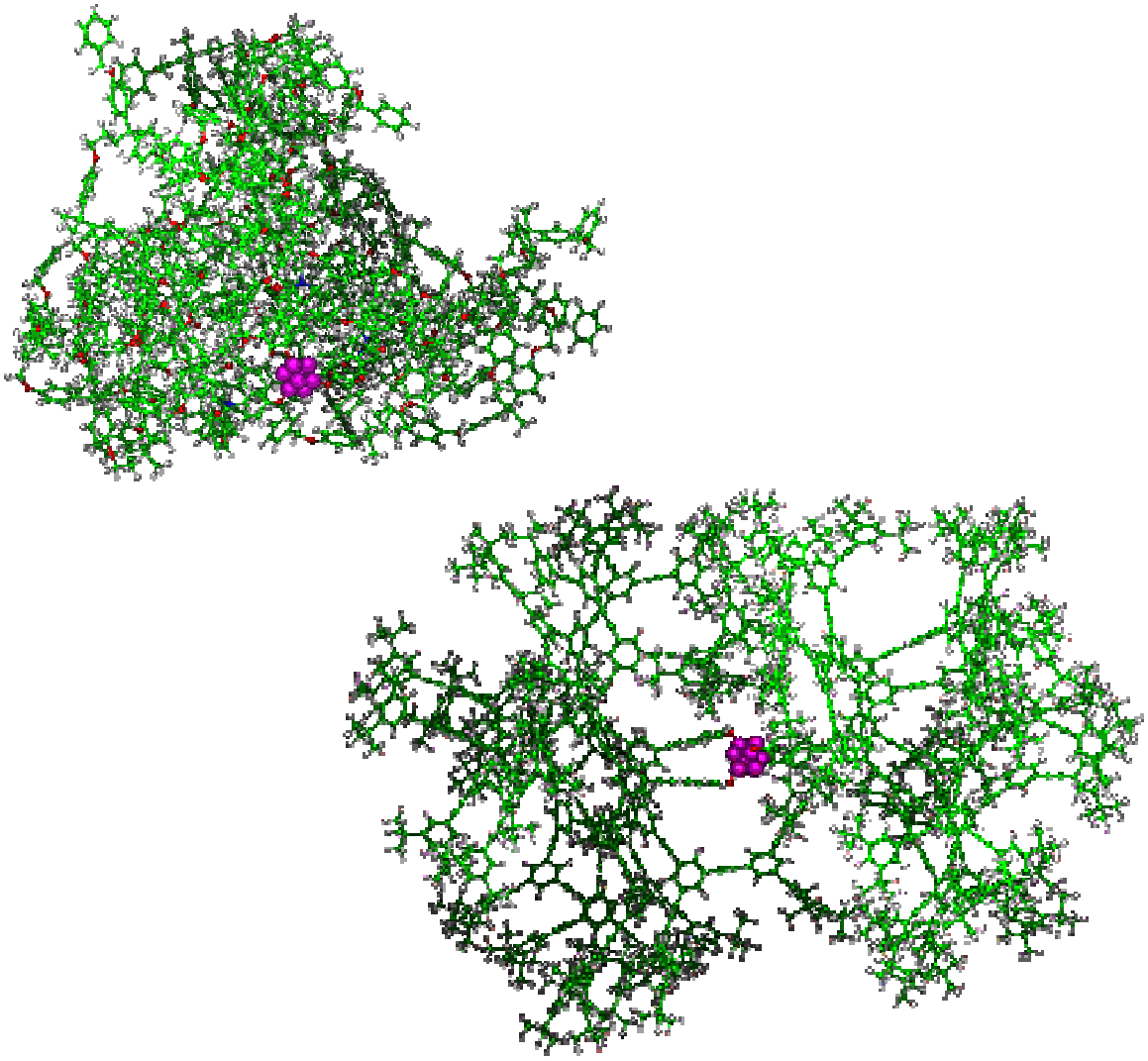

Figure 2.13. Ball and stick models of the lowest energy conformations found for G4Flex (top, left) and G4Rigid (bottom, right) during the respective conformational searches. The redox-active [Fe_4S_4] core is enlarged and colored pink.

Naturally, the electron transfer rates measured experimentally here will represent some average over the orientations of the molecule with respect to the electrode and some average over the different conformations accessible to the molecules. Further discussion of each of these points is warranted. Is consideration of an orientational average important in rationalizing relative electron transfer rates? Perhaps not. Murray, et al. recently published results on the electrochemistry of ferrocene-terminated, 8-carbon

alkanethiol-capped gold colloids of similar size to the molecules studied here.[67] A singular, multi-electron redox wave was observed for ca. 15 surface-bound ferrocenes. The interpretation of this result was that the rotational motion of this particle was much faster than the time-scale of the electrochemical experiment and thus the multiple, serial electron transfers appeared as one redox wave. This phenomenon plausibly would give rise to electrochemical behavior in our system that is also the result of rapid orientational averaging. Assuming a series of dendrimers in which the redox core is confined to a point at the molecular surface, the electron transfer rate would vary, at most, as the relative surface area of the molecules (slow rotation limit) and, at least would be invariant with molecular size (fast rotation limit). Clearly, the electron transfer rate is attenuated more than both scenarios for the flexible dendrimers studied here. This result indicates that, although these models help to paint a picture that distinguishes the flexible from the rigid dendrimers, they are static models, and that other dynamic behaviors are important here. Specifically, those behaviors related to the movement of the core within the architecture.

Significant changes in the core position within the flexible dendrimers probably occur on the time scale of the electrochemical experiment and are thus important to the encapsulation behavior as suggested by the range of minimum energy conformations illustrated in Figure 2.11 and 2.12. The idea that the flexible dendrimers have a much more mobile core than do the rigid dendrimers is intuitive: the rigid dendrimers are plausibly much more shape persistent[42-44,68] and thus do not change shape nearly as much over time. Thus, they provide a system for encapsulation that is more ideal from both a static and dynamic viewpoint.

Up until this point, it has been inferred that encapsulation is due to steric shielding of the redox couple from the electrode. The rigid dendrimers encapsulate the core better than the flexible dendrimers of a similar molecular weight as evidenced by attenuation of electron transfer rates. This conclusion merely indicates that the rigid architectures separate the redox unit more efficiently from the electrode. However, one can also ask how the differing dendrimer units mediate electron transfer over comparable distances.

Electron transfer rate measurements on redox active proteins[69-71] and the subsequent analysis of these rates with distance[72-75] suggests the dominance of a through-bond superexchange pathway for electron transfer. Distance-dependence of electron transfer rate, rather than being a measure of synthetic effort as was argued for molecular weight earlier, is interesting from the standpoint of understanding how units mediate electron transfer. In the case of these molecules, no truly accurate measure of distance is available. However, one might approximate core to perimeter distance using the results of the conformational searches presented. Using the radius of gyration as effectively an upper limit for the distance-dependence of electron transfer, this relation was calculated. The results of this analysis are shown in Figure 2.14.

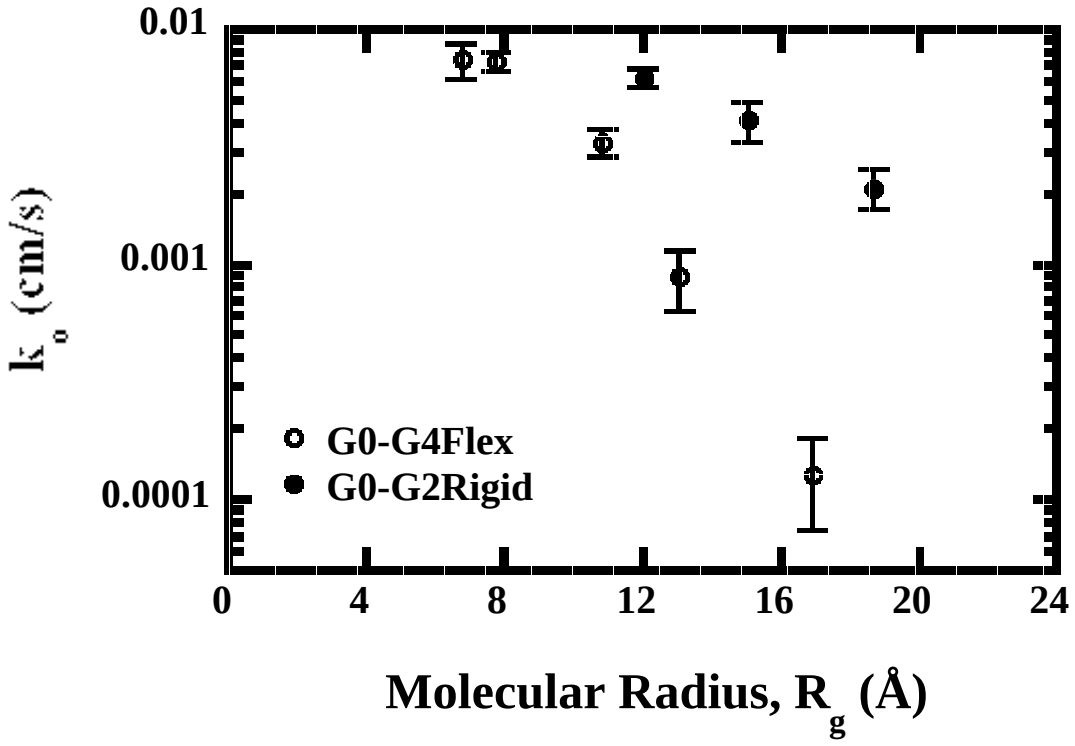

Figure 2.14. Distance-dependence of electron transfer rate constants for $[Fe_4S_4$-(S-Dend)$_4][Bu_4N]_2$ – Stiff and Flexible Metallodendrimers using radius of gyration as an effective distance parameter.

The most interesting conclusion of this data is that rigid dendrimers pass electrons more efficiently than flexible dendrimers on a distance-weighted basis. This is in contrast to the relative behaviors of these series of molecules on a molecular weight-weighted basis.

Phenylacetylene linkages have been discussed as molecular wires previously.[76] It is noted that these architectures are cross conjugated (e.g., meta-linked) and that coupling of the donor and acceptor to the conjugated bridge may be more important parameters than the coupling within the conjugated bridge when determining electron transfer rates.[77] However, despite these caveats, the phenylacetylene architecture has higher energy filled and lower energy unfilled states and it requires passage of the electron through fewer bonds per unit distance than does the flexible architecture. Thus, we feel that finding this difference is not particularly unintuitive.

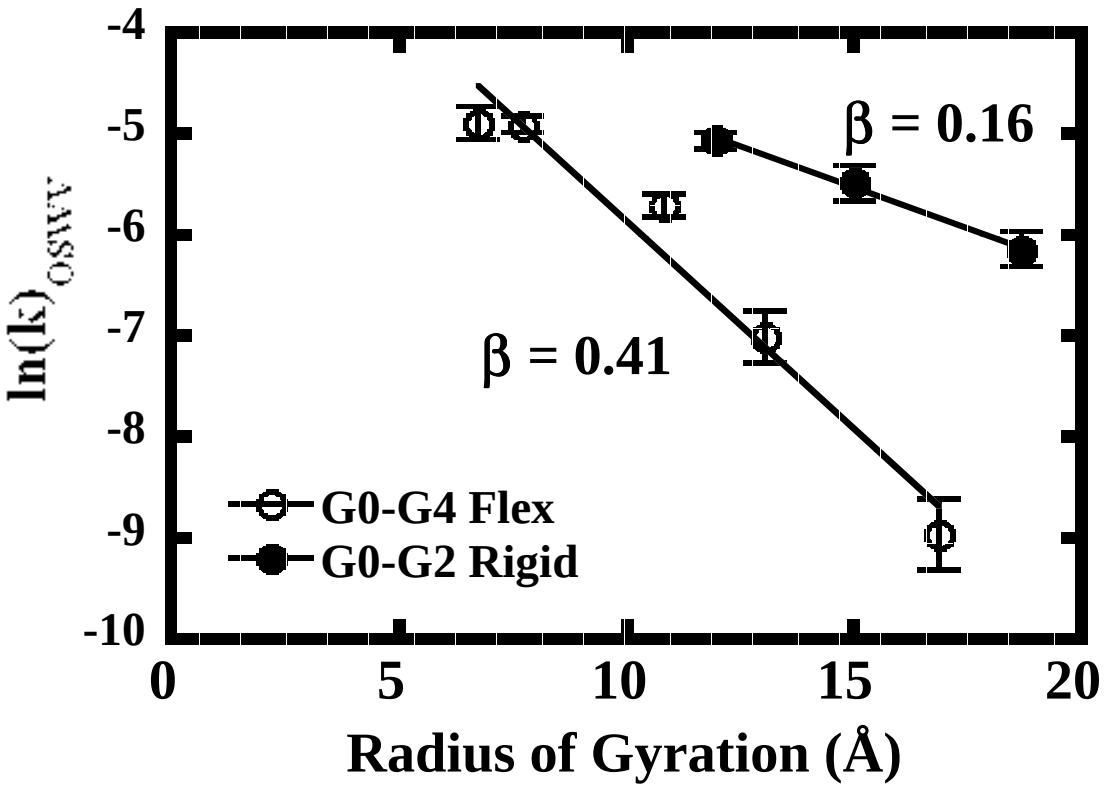

Figure 2.15. Effective β (the slope of -ln(k_0) versus distance) can be calculated as for the rigid series and flexible series using Radius of Gyration to approximate ET pathway distance.

Indeed, an effective β (the slope of -ln(k_0) versus distance) can be calculated as for the rigid series and flexible series. (Figure 2.15) An approximated distance representative of the ET pathway length must be derived. An upper limit to this length is the molecular radius of the metallodendrimer. The molecular Radius of Gyration (Rg) for each model

was used to derive the distance-decay parameter, β. A value of 0.16/Å for the rigid series and 0.40/Å for the flexible series was calculated. Obviously, these β-values must be compared cautiously with other values tabulated in the literature. Indeed, they are too small. One would expect a β-value for the rigid dendrimers closer to 0.57/Å (the value reported for electron transfer through phenylacetylene units) and a β of 0.9/Å for the flexible dendrimers (the value reported for electron transfer through saturated units).[76] These differences suggest that the electron is being transferred over a distance shorter than that indicated by the radius of gyration of the molecule.

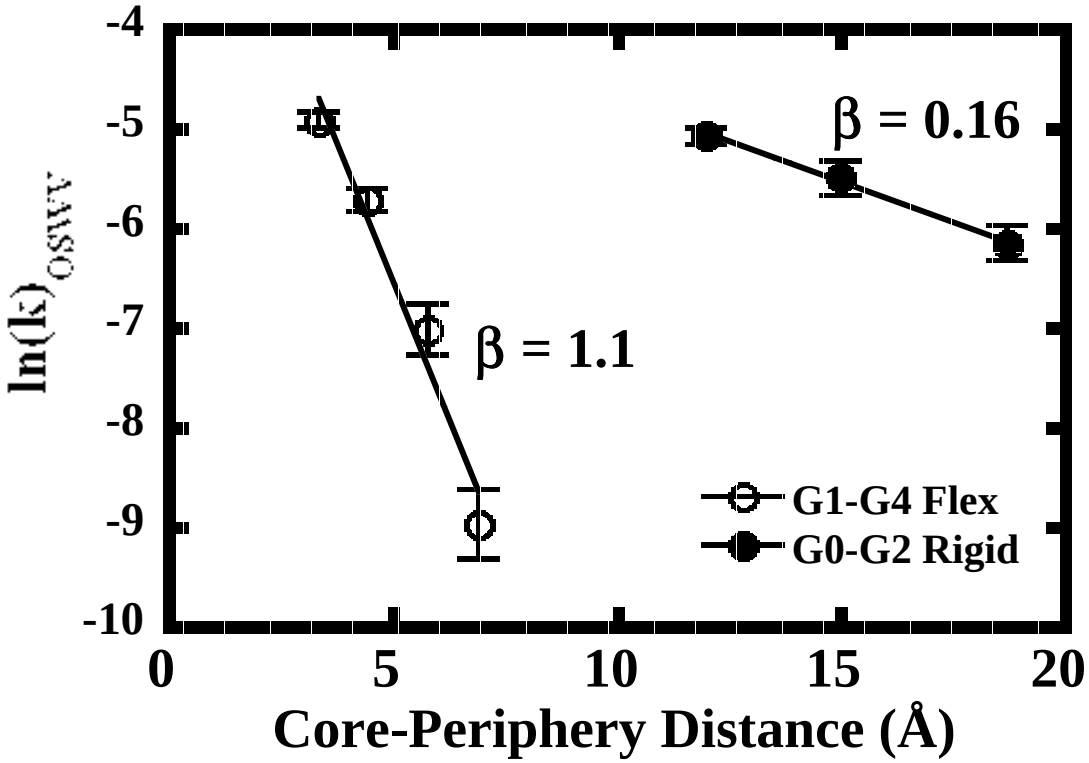

Figure 2.16. Effective β (the slope of -ln(k_0) versus distance can be calculated as for the rigid series and flexible series using core-periphery distance to approximate ET pathway distance. G0Flex was omitted as this molecule was not amenable to this treatment.

This shorter distance, the "core-periphery distance," was approximated in an effort to calculate more realistic β-values. (Figure 2.16) Here, the mathematical difference between the Radius of Gyration (R_g) and the core displacement from the molecular center-of-mass was used. For each model, this calculation was performed for all

structures within a 10 kcal Boltzmann cutoff structures, and averaged. An average core-periphery distance is important in the case of the conformationally flexible dendrimers; where this distance may vary over time in solution. Indeed, β-values calculated for the flexible series align reasonably with values reported in the literature.[76] The β-value for the rigid series did not change. This conclusion is somewhat obvious given central positioning of the redox-active core in the shape persistent rigid dendrimers.

These two β-values illustrate an important difference between these two types of molecules. The *apparent* "conductivity" in flexible metallodendrimers is reflective of that in proteins (~ 1/Å); whereas the *apparent* "conductivity" in the rigid metallodendrimers is an order of magnitude higher. In fact, the apparent "conductivity" in the rigid series rivals that for polyacetylene. (~ 0.2 /Å)

Such high transmission per unit in the case of the rigid dendrimers is not chemically intuitive. This is perhaps a signal that the pathway distances used for the rigid dendrimers are poorly approximated. Alternative pathways for ET in the rigid dendrimer series could be at play. A "through-space" ET event, in which an electron jumps directly from the core to the poised platimum electrode is possible. Note, however, the efficiency of ET through a solvent matrix will pale in comparison to that for a through-bond superexchange pathway. Because of these issues, the β-values in Figures 2.15 – 2.16 (especially those for the rigid dendrimers) should be considered with caution. Nevertheless, the qualitative trend in β-values is consistent with the chemical structure of the repeat units; and can serve to compare with structural metallodendrimer analogues in the future.

2.3. Conclusions

Dendrimer structures can encapsulate electroactive centers and attenuate electron transfer to/from these centers. There exist real molecular structure-property relationships for this attenuation behavior as evidenced by the very different behaviors observed in flexible and rigid dendrimer structures. Although the flexible dendrimers do attenuate electron transfer, this behavior does not arise from the type of steric shielding that one would

expect if one considered the geometric structure of the dendrimer to resemble its topological structure. Rather, the results presented here suggest that the core is mobile within the structure of the flexible dendrimers, and its dynamics are probably the most important parameter in governing encapsulation in this series of molecules. In contrast, the rigid dendrimers are more shape persistent and represent architectures in which the electron transfer rate attenuation is much more easily explained by steric shielding. Overall, the rigid series of dendrimers offers the better strategy for electron encapsulation on a molecular weight scale.

When the distance-dependence of electron transfer was approximated, however, the rigid dendrimers potentially may act as better mediators of electron transfer per unit distance; given the apparent attenuation of β in these structures. In fact, β in the rigid series is attenuated by an order of magnitude, when the ET pathway distance calculations incorporate offset core positions. Here, the apparent "conductivity" of the flexible series mimics that for protein matrices (~ 1/Å). The apparent "conductivity" in the rigid series is extremely high; rivaled only by polyacetylene and Duplex DNA (under specific circumstances). (Figure 2.17) This idea that the ET properties of synthetic metalloprotein mimics can be tailored by the primary structure is reminiscent of Nature's mechanism for supramolecular control.

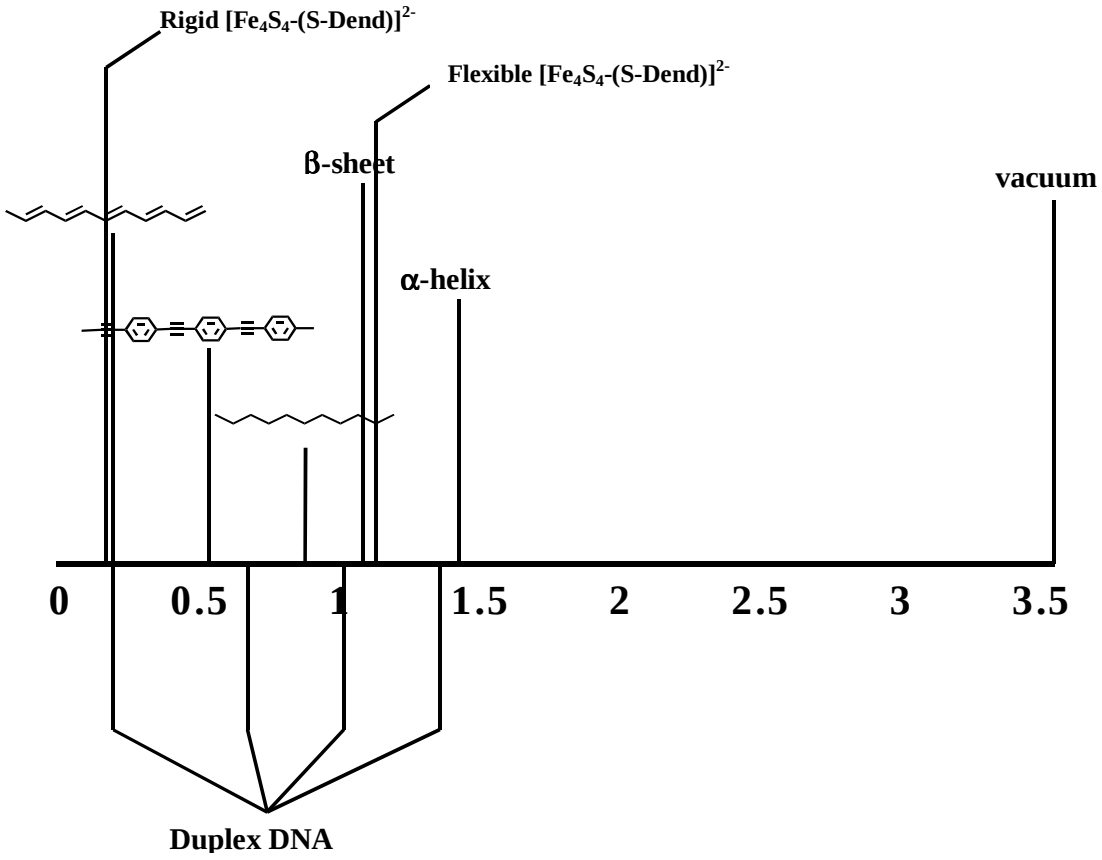

Figure 2.17. Distance-decay parameter, β, for $[Fe_4S_4\text{-}(S\text{-}Dend)_4][Bu_4N]_2$ –Stiff and Flexible Metallodendrimers relative to previously studied organic media.

2.4. Experimental

Instrumentation for Routine Characterization: All syntheses that were air and/ or moisture sensitive were either performed using standard Schlenk techniques under argon, or in a nitrogen-filled Vacuum Atmospheres drybox. ^{1}H NMR spectra were obtained with either a Gemini spectrometer operated at 300 MHz or a Varian spectrometer operating at 300 MHz. Chemical shifts were referenced to the chemical shifts of the residual protons of the NMR solvents.

Materials: All chemicals were purchased from Aldrich and used without further purification unless otherwise indicated. All deuterated solvents were purchased from

Cambridge Isotope Laboratories. Dimethylformamide-d_7 was used without further purification. Tetrahydrofuran, tetrahydrofuran-d_8 and diethyl ether were distilled from sodium benzophenone ketyl. Dimethyl sulfoxide and dimethyl sulfoxide-d_6 were distilled from calcium hydride. Dimethylformamide was distilled from Linde 4Å molecular sieves. All solvents used in the drybox were subjected to a minimum of three freeze-pump-thaw cycles before use to remove any dissolved oxygen. Ferrocene was recrystallized from ethanol. Tetraethylammonium tetrafluoroborate (TEAF) was recrystallized thrice from methanol and dried overnight under vacuum at 120°C.

Electrochemical apparatus. Electrochemical experiments were carried out on a Bioanalytical Systems CV-50W Voltammetric Analyzer. The three-electrode cell consisted of a Pt disk working electrode with geometric area = 0.0201cm^2, a Pt auxiliary electrode, and a homemade non-aqueous $Ag^+/AgNO_3$ reference electrode (Ag wire contacting a DMF solution of 0.01M $AgNO_3$ and 0.1M supporting electrolyte, tetraethylammonium tetrafluoroborate). All electrochemical experiments were carried out in a nitrogen filled drybox at room temperature. Millimolar concentrations of the analytes were dissolved in DMF or 25% pyridine/75% DMF (v/v), which contained 0.1 M tetraethylammonium tetrafluoroborate (TEAF) supporting electrolyte.

Initially, Pt disk working electrodes were polished with 1-micron diamond paste (BAS) followed by 0.25-micron diamond suspension (BAS). Prior to each experiment, the Pt working electrode was cycled continuously at 100 mV/s in blank electrolyte solution to obtain the double layer capacitance response. If any faradaic signal was observed, the Pt disk was re-polished as indicated above.

The freshly prepared, homemade nonaqueous $Ag^+/AgNO_3$ reference electrode was calibrated against ferrocene before each experiment ($E_{1/2}$ = 32 mV for 4mM in 0.1 M TEAF/DMF solution, average of 10 experiments) to provide a Fc/Fc^+ reference potential for each voltammetric experiment. The value of this reference was set to 32 mV versus this Fc/Fc^+ for all subsequent experiments. Ferrocene was not used as an internal reference to exclude the possibility of interacting with the macromolecular analyte.

Cyclic Voltammetry. Electron transfer rate constants were calculated using the method of Nicholson.[78] by using working curves that relate ΔE_p to the kinetic parameter Ψ. The rate-constant was determined by the following equation:

$$k^o = \Psi\left[D_o \pi \upsilon \left(\frac{nF}{RT}\right)\right]^{\frac{1}{2}} \qquad \text{(Equation 2.3)}$$

where Ψ is the kinetic parameter related to ΔE_p, D_o is the diffusion coefficient (cm^2/s), ν is the potential sweep rate (V/s), n is the number of electrons passed, F is Faraday's constant, R is the gas constant, and T is the cell temperature. Potential sweep rates ranged from 25 to 500 mV/s for analytes displaying quasi-reversible electrochemical behavior at these scan rates. However, **G3Flex** displayed ΔE_p > 190 mV at a sweep rate of 25 mV/s. Quasi-reversible kinetics were observable for this molecule only at very slow sweep rates (< 3 mV/s).

Osteryoung square wave Voltammetry. Osteryoung square wave Voltammetry[79-81] was performed using a step height of 4 mV, a sweep width amplitude of 25 mV, and a frequency of 15 Hz. Difference current was iteratively fit using FSQPLT software (provided by John J. O'Dea of the J. Osteryoung Group) to yield $E_{1/2}$, α, and log (κ/sqrt(t_d)). Electron transfer constant was calculated from the relation,

$$\log\left(\kappa\sqrt{t_d}\right) = \log\frac{k_o}{\sqrt{D_o}}\sqrt{t_d} \qquad \text{(Equation 2.4)}$$

where t_d is the experimental pulse period, D_o is the molecular diffusion coefficient, and κ is the reduced rate constant.

Chronoamperometry. Chronoamperometry was carried out using a pulse width of 500 ms and a potential step height of 800 mV centered around $E_{1/2}$ for each molecule studied.

Care was taken in choosing an experimental pulse width. Small pulse widths suffer from excess non-faradaic current or non-steady-state cell conditions. Large pulse widths suffer from effects of convection and migration. A pulse width was 500 ms was chosen as this pulse-width resided in the pulse-width independent region of the chronoamperometric diffusion-time plot. Linear portions of the Cottrell plots were iteratively fit using the Cottrell equation to yield the reported diffusion coefficient for each analyte.

Pulsed-Field-Gradient, Spin-Echo NMR. All experiments were carried out at 25 °C using a Bruker 500 MHz spectrometer (1996) with an Oxford narrow bore magnet (1989), SGI INDY host workstation, and XWINNMR software. The instrument was equipped with a three-channel gradient control unit (GRASPIII), variable-temperature unit, pre-cooling and temperature stabilization unit, and three frequency channels with waveform memory and amplitude shaping unit. A 5-mm i.d. ^{1}H/BB(^{109}Ag-^{31}P) triple-axis gradient probe (ID500-5EB, Nalorac Cryogenic Corp.) was used for all ^{1}H diffusion measurements. The probe was equipped with actively shielded gradient coils. The gradient strength was calibrated using literature values for water diffusion in $^{1}H_2O/^{2}H_2O$ mixtures. All samples were prepared in a nitrogen atmosphere in sealed NMR-tubes.
The longitudinal eddy current (LED) pulse sequences was used in all PFGSE experiments.[82,83] The experimental data was collected by varying the pulse gradient (g = 5-53 G/cm over 16 increments) in the y-direction, and keeping the duration of the gradient pulse, (δ = 5 ms) and the pulse interval, (Δ = 28 ms) constant. The attenuation of signal intensities was tabulated by measuring the peak height at each pulse gradient. Stejskal-Tanner plots were generated. A nonlinear least-squares fitting procedure was carried out on the attenuation of signal intensities to evaluate the diffusion coefficient. Error in determining diffusion coefficients was primarily that in determining relative signal intensity and error is reflected in parentheses in Table 2-1.

Flexible Iron-Sulfur Cluster Dendrimers: Unless stated otherwise, the flexible series of dendrimers were available from a preliminary study.[33] Synthetic protocol therein were followed for generating additional material.

Rigid Iron-Sulfur Cluster Dendrimers: The synthesis and characterization of the rigid series of dendrimers was carried out by Dr. Michael W. Hager and reported in the literature.[86]

Computational Protocol. Atomistic dendrimer models were employed during high temperature searching and quenched molecular dynamics.[87-89] (Appendix I) Molecular forces were described using the DISCOVER CVFF (Consistent Valence Forcefield) all-atom forcefield. Hydrogen atoms were represented explicitly, and all atom centers were described using standard potentials terms. The unparameterized atomic centers in the dianionic Fe_4S_4 core were represented as sp^3 carbon atoms; thus no charge on this core was considered and no counterions were included. No cross terms were taken into account.

All minimizations were performed using a combination of steepest-descents and conjugate gradients algorithms. The appropriate number of minimization steps were performed to obtain an RMS deviation < 0.1 kcal/mol•Å for the first and second generation models and an RMS deviation of < 0.2 kcal/mol•Å for the third and fourth generation models. Long range van der Waals and Coulombic interactions were neglected beyond a certain point, specified by the "cutoff distance." Neighbor lists were updated by specifying a buffer width of 0.5 Å. This is the range outside of the cutoff distance within which atoms are updated after every iteration. In all calculations, non-bonded interactions were cut off beyond 8.0 Å (cutoff = 8.0 Å), a switching function was applied over the last 3.5 Å (swtdis = 3.5 Å). Goddard et al. showed that minimization error associated with a nonbonded cutoff is more dependent on the spline width (the distance over which nonbonded energy function is smoothed to zero); rather than the cut off value.[84] Error associated with the cutoff distance was minimized by using an optimal spline width of 0.44 times length of the cut off distance. Nonbonded interactions were considered in this way during all molecular dynamics simulations as well.

Molecular dynamics simulations were done with bond lengths constrained to their equilibrium distances using the RATTLE algorithm.[85] In this way, an integration timestep of 2 fs can be used without introducing significant instability or inaccuracy into the integration process. Additionally, all simulations were done at constant temperature (NVT ensemble) in which the system is coupled to a heat bath using the method, "direct velocity scaling." Direct velocity scaling uniformly scales all atom velocities simultaneously according to the equation

$$\left(\frac{v_{new}}{v_{old}}\right)^2 = \frac{T_{target}}{T_{system}} \qquad \text{(Equation 2.5)}$$

where *v* is atom velocity and *T* is temperature. This scaling occurs only if the designated temperature of the system changes more than 10 K between two integration steps. This temperature criterion is explicitly specified within the DISCOVER 97.0 program as the parameter, "temperature window."

All models, input files, and scripts were constructed on an Indigo2 Silicon Graphics workstation using the MSI BUILDER and DISCOVER3 modules with the InsightII graphical user interface; where all rendering was performed as well. Calculations and scripts were run on SGI Origin 2000 workstation cluster at the North Carolina Supercomputing Center (Research Triangle Park, NC) using MSI DISCOVER version 97.0 in standalone mode.

Data analysis of structure sets included calculation of potential energy and several geometric parameters. Energetic and geometric properties of all conformers were calculated and catalogued using a script written in-house using BTCL language and run within the DISCOVER 97.0 standalone environment. This script is given below. Geometric properties calculated were: molecular radius of gyration, R_g; core displacement from the molecular center-of-mass, R_{core}; and the three principle moments

of inertia, $I_x < I_y < I_z$. From these data the following geometric properties can be calculated: relative core offset, R_{core} / R_g; and molecular eccentricity, I_z / I_x.

```
1     for {$i = 1} {$i < 26} {incr i} {
2     for {$k = 1} {$k < 5} {incr k} {
3     readFile coordinate filename = struc$i$k.cor
4     subset define Subset "*:*:$i$k" "C*,H*,N*,O*"
5     pseudoAtom define com$i$k "*:*:$i$k" weight Mass
6     molGeom get coords com "com$i$k"
7     molGeom get coords dendcoords "*:*:$i$k"
8     geometry radii distance $com $dendcoords
9     vector v "[object radii]"
10    vector v2 "[object radii]"
11    vector v3 multiply $v $v2
12    vector v4 sum $v3
13    vector v5 1548
14    vector Rg2 divide $v4 $v5
15    vector Rg sqrt $Rg2
16    set radius [vector Rg]
17    geometry prin principalAxes $dendcoords moment moinertia
18    set axes [object moinertia]
19    subset define Subset "*:1:$i$k" "O*"
20    pseudoAtom define cen$i$k "*:1:$i$k" weight Mass
21    molGeom get coords center "cen$i$k"
22    geometry offset distance $center $com
23    set core [object offset]
24    set energy [readFile coordinate filename = struc$i$k.cor]
25    puts file3 "struc$i$k $energy $radius $core $axes"
26    unset com
27    unset dendcoords
28    unset v
29    unset v2
30    unset v3
31    unset v4
32    unset v5
33    unset Rg2
34    unset Rg
35    unset radius
36    unset radii
37    unset prin
38    unset moinertia
39    unset axes
40    unset center
41    unset offset
42    unset core
43    unset energy
44    }}
```

Quenched molecular dynamics is a conformational searching method designed to search the conformational space of a molecular model. *Here, we do not employ an arbitrary starting structure.* Two search routines were administered for each model considered.

First, a high temperature (1000K or higher) coarse-grained search, generating 100 minimized conformations, was performed. The lowest energy conformer from this set was the starting point for quenched molecular dynamics. These two conformational searching routines are described in detail in Appendix I.

2.5. References and Notes

1)Zeng, F.; Zimmerman, S. C. *Chem. Rev.* **1997**, *97*, 1681-1712.

2)Zanini, D.; Roy, R. *J. Am. Chem. Soc.* **1997**, *119*, 2088-2095.

3)Walliman, P.; Seiler, P.; Diederich, F. *Helvetica Chimica Acta* **1996**, *79*, 779-788.

4)Valério, C.; Fillaut, J.-L.; Ruiz, J.; Guittard, J.; Blais, J.-C.; Astruc, D. *J. Am. Chem. Soc.* **1997**, *119*, 2588-2589.

5)Turro, N. J.; Barton, J. K.; Tomalia, D. A. *Acc. Chem. Res.* **1991**, *24*, 332-340.

6)Newkome, G. R.; Woosley, B. D.; He, E.; Moorefield, C. N.; Güther, R.; Baker, G. R.; Escamilla, G. H.; Merrill, J.; Luftman, H. *Chem. Commun.* **1996**, 2737-2738.

7)Mattei, S.; Seiler, P.; Diederich, F.; Gramlich, V. *Helvetica Chimica Acta* **1995**, *78*, 1904-1911.

8)Lhotak, P.; Shinkai, S. *Tetrahedron* **1995**, *51*, 7681-7696.

9)Bruening, M. L.; Zhou, Y.; Aguilar, G.; Agee, R.; Bergbreiter, D. E.; Crooks, R. M. *Langmuir* **1997**, *13*, 770-778.

10)Bar, G.; Rubin, S.; Cutts, R. W.; Taylor, T. N.; Zawodzinski Jr., T. A. *Langmuir* **1996**, *12*, 1172-1179.

11)Bruening, M. L.; Zhou, Y.; Zhao, M.; Crooks, R. M.; Bergbreiter, D. E. *Proc. PMSE* **1997**, *77*, 77-78.

12)Liu, Y.; Zhao, M.; Bergbreiter, D. E.; Crooks, R. M. *J. Am. Chem. Soc.* **1997**, *119*, 8720-8721.

13)Sheiko, S. S.; Muzafarov, A. M.; Winkler, R. G.; Getmanova, E. V.; Eckert, G.; Reineker, P. *Langmuir* **1997**, *13*, 4172-4181.

14)Tsukruk, V. V.; Rinderspacher, F.; Bliznyuk, V. N. *Langmuir* **1997**, *13*, 2171-2176.

15)Zhou, J.; Hu, Z.; Münck, E.; Holm, R. H. *J. Am. Chem. Soc.* **1996**, *118*, 1966-1980.

16)Wells, M.; Crooks, R. M. *J. Am. Chem. Soc.* **1996**, *118*, 3988-3989.

17)Brunner, H.; Bublak, P. *Synthesis* **1995**, *January 1995*, 36-38.

18)Brunner, H. *J. Organomet. Chem.* **1995**, *500*, 39-46.

19)Butz, T.; Murer, P.; Seebach, D. *Proc. PMSE* **1997**, *77*, 132-133.

20)Mak, C. C.; Chow, H.-F. *Macromolecules* **1997**, *30*, 1228-1230.

21)McElhanon, J. R.; Wu, M.-J.; Escobar, M.; McGrath, D. V. *Macromolecules* **1996**, *29*, 8979-8982.

22)McElhanon, J. R.; Wu, M.-J.; Escobar, M.; Chaudhry, U.; Hu, C.-L.; McGrath, D. V. *J. Org. Chem.* **1997**, *62*, 908-915.

23)Seebach, D.; Herrmann, G. F.; Lengweiler, U. D.; Bachmann, B. M.; Amrein, W. *Angew. Chem. Int. Ed. Engl.* **1996**, *35*, 2795-2797.

24)Jansen, J. F. G. A.; de Brabander-van den Berg, E. M. M.; Meijer, E. W. *Science* **1994**, *266*, 1226-1229.

25)Jansen, J. F. G. A.; Janssen, R. A. J.; de Branbander-Van den Berg, E. M. M.; Meijer, E. W. *Adv. Mater.* **1995**, *7*, 561-564.

26)Jansen, J. F. G. A.; Meijer, E. W.; de Branbander-Van den Berg, E. M. M. *J. Am. Chem. Soc.* **1995**, *117*, 4417-4418.

27)Miklis, P.; Çagin, T.; Goddard III, W. A. *J. Am. Chem. Soc.* **1997**, *119*, 7458-7462.

28)Dandliker, P. J.; Diederich, F.; Gross, M.; Knobler, C. B. *Angew. Chem. Int. ed.* **1994**, *33*, 1739.

29)Dandliker, P. J.; Diederich, F.; Gisselbrecht, J.-P.; Louati, A.; Gross, M. *Angew. Chem. Int. Ed. Engl.* **1995**, *34*, 2725-2728.

30)Dandliker, P. J.; Diederich, F.; Zingg, A.; Gisselbricht, J.-P.; Gross, M.; Louati, A.; Sanford, E. *Helv. Chim. Acta* **1997**, *80*, 1773-1801.

31)Cardona, C. M.; Kaifer, A. E. *J. Am. Chem. Soc.* **1998**, *120*, 4023-4024.

32)Pollak, K. W.; Leon, J. W.; Fréchet, J. M. J.; Maskus, M.; Abruña, H. D. *Chem. Mater.* **1998**, *10*, 30-38.

33)Gorman, C. B.; Parkhurst, B. L.; Chen, K.-Y.; Su, W. Y. *J. Am. Chem. Soc.* **1997**, *119*, 1141-1142.

34)Kawa, M.; Fréchet, J. M. J. *Chem. Mater.* **1998**, *10*, 286-296.

35)Gorman, C. B. *Adv. Mater.* **1997**, *9*, 1117-1119.

36)Chen, K.-Y.; Gorman, C. B. *J. Org. Chem.* **1996**, *61*, 9229-9235.

37)Bharathi, P.; Patel, U.; Kawaguchi, T.; Pesak, D. J.; Moore, J. S. *Macromolecules* **1995**, *28*, 5955-5963.

38)Xu, Z.; Kahr, M.; Walker, K. L.; Wilkins, C. L.; Moore, J. S. *J. Am. Chem. Soc.* **1994**, *116*, 4537-4550.

39)Newkome, G. R.; Young, J. K.; Baker, G. R.; Potter, R. L.; Audoly, L.; Cooper, D.; Weis, C. D.; Morris, K.; Johnson Jr., C. S. *Macromolecules* **1993**, *26*, 2394-2396.

40)Young, J. K.; Nelson, J. C.; Moore, J. S. *J. Am. Chem. Soc.* **1994**, *116*, 10841-10842.

41)Ihre, H.; Hult, A. *Proc. PMSE* **1997**, *77*, 71-72.

42)Moore, J. S. *Acc. Chem. Res.* **1997**, *30*, 402-413.

43)Morgenroth, F.; Reuther, E.; Müllen, K. *Angew. Chem. Int. Ed. Engl.* **1997**, *36*, 631-634.

44)Morgenroth, F.; Kübel, C.; Müllen, K. *J. Mater. Chem.* **1997**, *7*, 1207-1211.

45)Tomoyose, Y.; Jiang, D.-L.; Jin, R.-H.; Aida, T.; Yamashita, T.; Horie, K.; Yashima, E.; Okamoto, Y. *Macromolecules* **1996**, *29*, 5236-5238.

46)Jin, R. H.; Aida, T.; Inoue, S. *J. Chem. Soc., Chem. Commun.* **1993**, 1261-1263.

47)Sadamoto, R.; Tomioka, N.; Aida, T. *J. Am. Chem. Soc.* **1996**, *118*, 3978-3979.

48)Dandliker, P. J.; Diederich, F.; Gross, M.; Knobler, C. B.; Louati, A.; Sanford, E. M. *Angew. Chem. Int. Ed. Engl.* **1994**, *33*, 1739-1741.

49)Collman, J. P.; Fu, L.; Zingg, A.; Diederich, F. *Chem. Commun.* **1997**, 193-194.

50)Jiang, D.-L.; Aida, T. *Chem. Commun.* **1996**, 1523-1524.

51)Gorman, C. B. *Adv. Mater.* **1998**, *10*, 295-309.

52)Bhyrappa, P.; Young, J. K.; Moore, J. S.; Suslick, K. S. *J. Am. Chem. Soc.* **1996**, *118*, 5708-5711.

53)Tomioka, N.; Takasu, D.; Takahashi, T.; Aida, T. *Angew. Chem. Int. Ed. Engl.* **1998**, *37*, 1531-1534.

54)Norsten, T.; Branda, N. *Chem. Commun.* **1998**, 1257-1258.

55)Nierengarten, J.-F.; Schall, C.; Nicoud, J.-F. *Angew. Chem. Int. Ed. Engl.* **1998**, *37*, 1934-1935.

56)Kraus, G. A.; Louw, S. V. *J. Org. Chem.* **1998**, *63*, 7520-7521.

57)Kimura, M.; Nakada, K.; Yamaguchi, Y.; Hanabusa, K.; Shirai, H.; Kobayashi, N. *Chem. Commun.* **1997**, 1215-1216.

58)Brewis, M.; Clarkson, G. J.; Goddard, V.; Helliwell, M.; Holder, A. M.; McKeown, N. B. *Angew. Chem. Int. Ed.* **1998**, *37*, 1092-1094.

59)Takada, K.; Díaz, D. J.; Abruña, H. D.; Cuadrado, I.; Casado, C.; Alonso, B.; Morán, M.; Losada, J. *J. Am. Chem. Soc.* **1997**, *119*, 10763-10773.

60)Osteryoung, J.; O' Dea, J. J. ; Marcel Dekker: New York, 1986; Vol. 14.

61)Que Jr., L.; Bobrik, M. A.; Ibers, J. A.; Holm, R. H. *J. Am. Chem. Soc.* **1974**, *96*, 4168-4177.

62)Hill, C. L.; Renaud, J.; Holm, R. H.; Mortenson, L. E. *J. Am. Chem. Soc.* **1977**, *99*, 2549-2557.

63)DePamphilis, B. V.; Averill, B. A.; Herskovitz, T.; Que Jr., L.; Holm, R. H. *J. Am. Chem. Soc.* **1974**, *96*, 4159-4167.

64)Al-Obeidi, F.; O'Connor, S.; Job, C.; Hruby, V.; Pettitt, M. *Journal of Peptide Research* **1998**, *51*, 420-431.

65)O'Connor, S.; Smith, P.; Al-Obeidi, F.; Pettitt, B. M. *J. Med. Chem.* **1992**, *35*, 2870-2881.

66)Sun, Y.; Kollman, P. A. *J. Comput. Chem.* **1992**, *13*, 33-40.

67)Green, S. J.; Pietron, J. J.; Stokes, J. J.; Hostetler, M. J.; Vu, H.; Wuelfing, W. P.; Murray, R. W. *Langmuir* **1998**, *14*, 5612-5619.

68)Pesak, D. J.; Moore, J. S. *Angew. Chem. Int. Ed. Engl.* **1997**, *36*, 1636-1639.

69)Winkler, J. R.; Gray, H. B. *Chem. Rev.* **1992**, *92*, 369-379.

70)Wuttke, D. S.; Bjerrum, M. J.; Winkler, J. R.; Gray, H. B. *Science* **192**, *256*, 1007-1009.

71)Langen, R.; Chang, I. J.; Germanas, J. P.; Richards, J. H.; Winkler, J. R.; Gray, H. *Science* **1995**, *268*, 1733-1735.

72)Beratan, D. N.; Onuchic, J. N.; Winkler, J. R.; Gray, H. B. *Science* **1992**, *258*.

73)Beratan, D. N.; Skourtis, S. S. *Curr. Opin. Chem. Biol.* **1998**, *2*, 234-243.

74)Risser, S. M.; Beratan, D. N.; Onuchic, J. N. *J. Phys. Chem.* **1993**, *97*, 4523-4527.

75)Skourtis, S. S.; Beretan, D. N. *J. Phys. Chem. B* **1997**, *97*, 1215-1234.

76)Sachs, S. B.; Dudek, S. P.; Hsung, R. P.; Sita, L. R.; Smalley, J. F.; Newton, M. D.; Feldberg, S. W.; Chidsey, C. E. D. *J. Am. Chem. Soc.* **1997**, *119*, 10563-10564.

77)Davis, W. B.; Svec, W. A.; Ratner, M. A.; Wasielewski, M. R. *Nature* **1998**, *396*, 60-63.

78)Nicholson, R. S. *Anal. Chem.* **1965**, *37*, 1351-1354.

79)O' Dea, J. J.; J., O.; Osteryoung, R. A. *Anal. Chem.* **1981**, *53*, 695-701.

80)Turner, J. A.; Christie, J. H.; Yukovic, M.; Osteryoung, R. A. *Anal. Chem.* **1977**, *49*, 1904-1908.

81)Brewis, M.; Clarkson, G. J.; Holder, A. M.; McKeown, N. B. *Chem. Commun.* **1998**, 969-970.

82)Gibbs, S. J.; Johnson, J., C. S. *J. Magn. Reson.* **1991**, *93*, 395-402.

83)Zeng, L.; Stejskal, E. O. *Applied Spectroscopy* **1996**, *50*, 1402-1407.

84)Ding, H.-Q.; Karasawa, N.; Goddard III, W. A. *Chem. Phys. Lett.* **1992**, *193*, 197-201.

85)Anderson, H. C. *J. Comp. Phys.* **1983**, *52*, 24-34.

86) Gorman, C. B.; Smith, J. C.; Hager, M. W.; Parkhurst, B. L.; Sierzputowska-Gracz, H.; Haney, C. A. *J. Am. Chem. Soc.* **1999**, *in press*.

87) Sun, Y.; Kollman, P.A. *J. Comput. Chem.* **1992**, *13*, 33-40.

88) O'Connor, S. D.; Smith, P. E.; Al-Obeidi, F.; Pettitt, B. M.. *J. Med. Chem.* **1992**, *35*, 2870-2881.

89) Al-Obeidi, F.; O'Connor, S. D.; Job, C.; Hruby, V. J.; Pettitt, B. M. *J. Peptide Res.* **1998**, *51*, 420-431.

CHAPTER 3

USE OF A PARAMAGNETIC CORE TO AFFECT LONGITUDINAL NUCLEAR RELAXATION IN DENDRIMERS — A TOOL FOR PROBING DENDRIMER CONFORMATION

This work was done in close collaboration with Dr. Michael W. Hager. Additionally, the synthetic efforts of Dr. Kang Yi Chen and Mr. Brandon L. Parkhurst and discussions with Professor Ed Stejskal impacted this project. These contributions are gratefully acknowledged.

This work was the subject of a publication, Gorman, C. B.; Hager, M. W.; Parkhurst, B. L.; Smith, J. C. *Macromolecules* **1998**, *31*, 815-822.

3.1. Introduction

Probing the conformation of dendrimers in various environments is an important step in understanding and predicting their behavior. Several demonstrations have suggested uses for dendrimers in such areas as molecular recognition,[1-3] surface modification,[4-7] asymmetric synthesis[8,9] and small molecule encapsulation.[10,11] In order to develop structure-property relationships for dendrimer conformation and to engage in rational design strategies for new dendritic structures, several methods for probing conformation have emerged. These include the study of their viscosity behavior,[12-14] and the use of solvatochromic,[15] electrochemical,[16,17] photochemical[18-20] nuclear magnetic resonance [10,20-22] and electron paramagnetic resonance[23-25] probes.

The redox-active core dendrimers, $[Bu_4N]_2[Fe_4S_4(S\text{-}Dend)_4]$, were synthesized previously by the Gorman Group.[26] Iron-sulfur clusters,"Fe_4S_4" are ubiquitous in nature where they function as electron transfer and storage sites as well as active sites and structure-enforcing units in enzymes.[27-29] The $[Fe_4S_4(S\text{-}R)4]^{2-}$ moiety has also been the subject of several model studies that helped to define its reactivity, electrochemical and magnetic behavior.[30-34] Inorganic cluster cores can be used to prepare highly symmetrical dendrimers as well as dendrimers with electroactive, luminescent and/or paramagnetic centers.

It is this latter property that is the subject of this particular study. Iron-sulfur clusters containing the $[Fe_4S_4(SR)_4]^{2-}$ (R = heretofore a small alkyl or aryl group) moiety are paramagnetic with a magnetic moment of approximately 2 Bohr magnetons at room temperature.[27,35] This core results in small Fermi contact shifts and line broadening of the ^1H NMR signals of protons a few bonds away from it. [26,33] This feature was utilized as spectroscopic evidence for the formation of iron-sulfur core dendrimers. The paramagnetic core of the molecule can also influence the longitudinal relaxation time constants (T_1) of nuclei in the dendrimer.

NMR techniques have been used previously to probe dendrimer and dendron (e.g. a structure composed of one arm of a dendrimer) conformation, respectively. Meltzer et al. [36,37] employed ^{13}C NMR to probe relaxation in PAMAM-type dendrimers, but only the terminal and internal nuclei were chemical shift distinguishable in this case. In the work reported here, the chemical shifts of the protons in all different generations of each molecule are distinguishable. Wooley et al.[38] employed REDOR NMR on dendrons in the solid state and came to the conclusion that the terminal generations (e.g. those at the topological periphery) of a nuclear spin labeled dendron were found to come into close contact with a differently nuclear spin labeled focal point. Although the dendrons in this study[38] and the dendrimers reported here had similar molecular weights, these two types of molecules are topologically very different.

3.2. Results and Discussion

3.2.1. Paramagnetic versus Diamagnetic Dendrimers

The molecules under study are shown in Figure 3.1. Specifically, dendrimers of generations 1-3 were synthesized that contained either a paramagnetic $[Fe_4S_4(SR)_4]^{2-}$ (FeS) core or a diamagnetic tetraphenylmethane (TPM) core. Generally, paramagnetism in NMR spectroscopy is the effect of an unpaired electron on surrounding NMR active nuclei. In the FeS core dendrimers, an unpaired electron resides at the Fe_4S_4 core. Its influence on the surrounding ^1H nuclei is central to this study.

Both the FeS and TPM dendrimers have similar ligands about the core and a similar symmetry at the core. As a clear, graphical representation of these molecules is difficult, only one of the four dendrons comprising the dendrimer is shown in detail in Figure 3.1. The other three dendron arms around the core are abbreviated (as a circled D) but have the same structure as the fully drawn dendron. The designations G0, G1 ..., Gn refer to the aromatic protons at the n-th branch point (generation) in the molecule. The designation “Term.” refers to the topologically peripheral C_6H_5 groups. (Figure 3.1) The superscripts A and B merely denote the more upfield and downfield signals respectively

in the AA'XX' pattern for the different *para*-substituted phenyl rings considered. Throughout this paper, the term "generation" will be used to denote a group of repeat units at the same topological branch point within a given dendrimer rather than to refer to the number of branch points in the dendrimer.

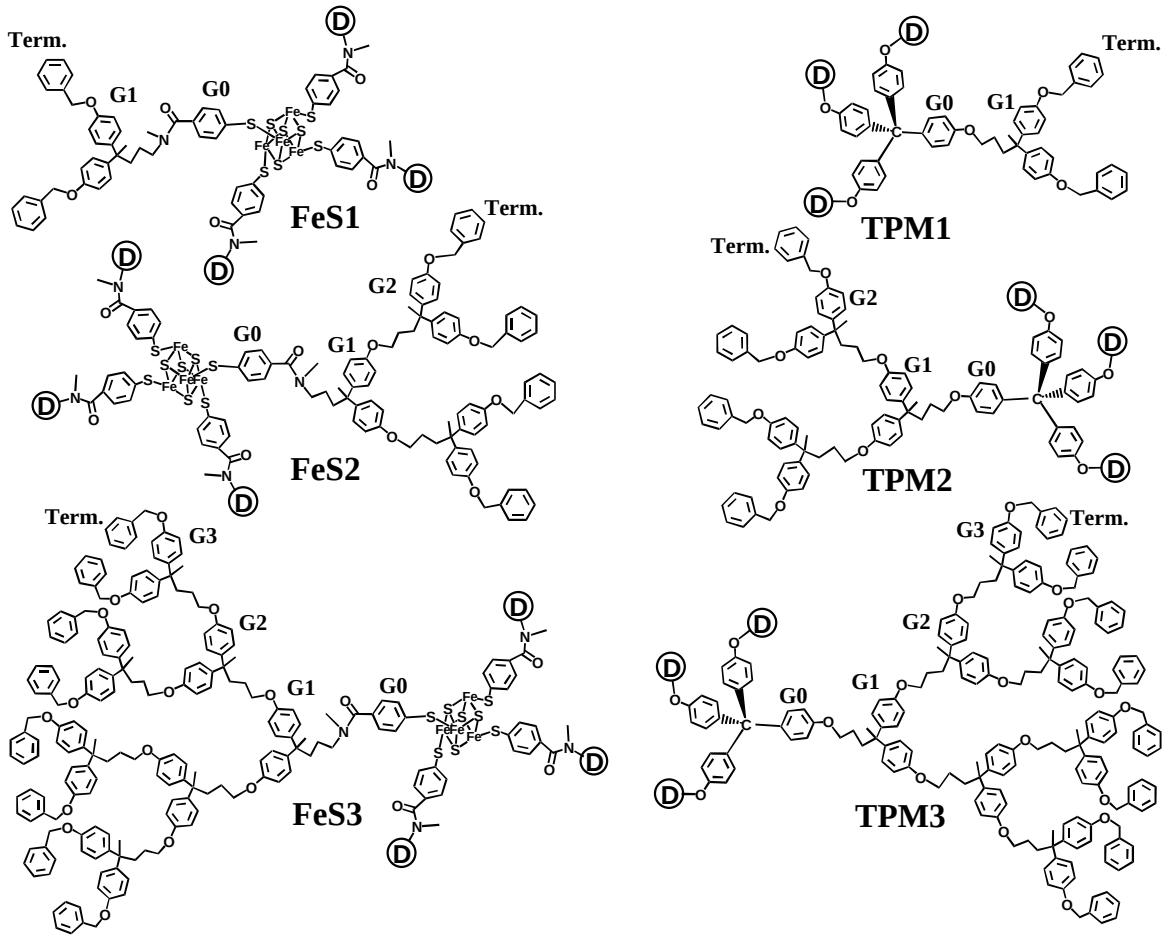

Figure 3.1. Molecules considered in this study. The FeS-type molecules are dianions and are prepared as bis(tetrabutylammonium) salts.

FeS core dendrimers **FeS1**, **FeS2**, and **FeS3** (Figure 3.1) were available from a previous study.[26] Synthesis of the TPM dendrimers was carried out by Dr. Michael W. Hager. Synthetic schemes and details have been reported.[39]

In this study, a paramagnetic core $Fe_4S_4(SR)_4^{2-}$ was used to probe the average proximity of nuclei in the dendrimer with respect to the molecular core. By comparing the longitudinal relaxation time constants (T_1) of structurally similar dendrimers in which the core is alternatively paramagnetic and diamagnetic, the relative contribution of the paramagnetic center to the overall relaxation was determined.

This comparison is possible due to the influence that the paramagnetic core has on surrounding nuclei. In general, the nuclei that experience paramagnetism exhibit shortened T_1 relaxation time constants. Only those nuclei found very close to a paramagnetic site will be affected. In fact, the efficiency of paramagnetic relaxation effects (and therefore T_1 reduction) will decay as $1/r^6$ where r is the distance between nucleus and unpaired electron. (Figure 3.2) In a paramagnetic core dendrimer, for paramagnetic relaxation to impact T_1, the nuclei must penetrate the microenvironment of the Fe_4S_4 core. (Figure 3.2) Reduction of T_1 was observed, indicating close approach of each part of the molecule to the paramagnetic core. These observations support a model of dendrimer conformation in which all of the different generations within a dendrimer are radially distributed throughout it and do not exist in a “shell-like” conformation with respect to the center of the molecule.

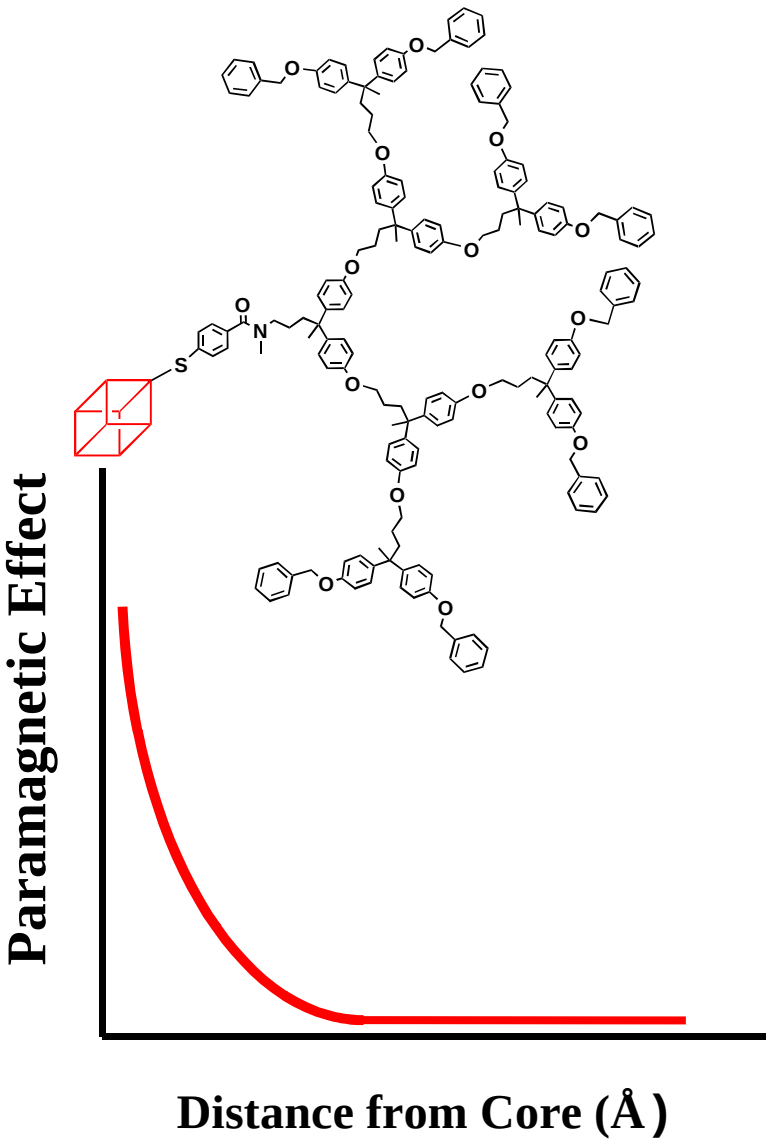

Figure 3.2. The efficiency of paramagnetic relaxation effects versus distance from the core. The influence of the unpaired electron (at the Fe_4S_4 core) will decay as $1/r^6$ where r is the distance between nucleus and Fe_4S_4 core. One arm of the FeS3 dendrimer is illustrated graphically.

3.2.2. Comparison of the Relaxation Behavior of Diamagnetic and Paramagnetic Core Dendrimers

Proton NMR specta of the aromatic regions of FeS and TPM core dendrimers are shown in Figures 3.3 and 3.4, respectively. These resonances have sufficiently different chemical shifts so as to distinguish, to a point, the topologically different generations (e.g. G0, G1..., Gn in Figure 3.1) within the dendrimer. The benzyl group resonance (designated Bn in Figure 3.5) although not shown in these spectra was also considered in this study. This resonance appeared as a singlet at 5.0 ppm for all the molecules considered. Other ^{1}H NMR resonances as well as ^{13}C NMR resonances for these molecules did not satisfy this criterion and were not considered further.

The paramagnetic center in the FeS dendrimers, although it resulted in shifting and broadening of the G0 protons, did not dramatically affect the chemical shift or broadness of the other proton signals in the dendrons (Figure 3.3). The signals were thus assignable to the different generations. Furthermore, this observation indicated a lack of Fermi contact as a mechanism for influencing either the chemical shift or T_1 value of these other protons.

The most notable difference in the relaxation data (Figure 3.5) was the dramatic shortening of T_1 values for the protons in the paramagnetic core (**FeS**) dendrimers as compared to those in the diamagnetic core (**TPM**) dendrimers. This shortening is attributed to the direct, through-space interaction of these protons with the unpaired electron centered at the core of the **FeS** dendrimers. This observation leads to the most significant result of this paper — protons in each generation of these dendrimers must approach the core of the molecule closely in space to experience the attenuation in T_1 observed for the **FeS** dendrimers compared to that of **TPM** dendrimers. The value of T_1 measured is an average T_1 for the protons in each generation of the molecule. Thus, an attenuated T_1 value due to the presence of a paramagnetic core indicates qualitatively that at least some of each set of protons approach the core closely on the time scale of the NMR experiment.

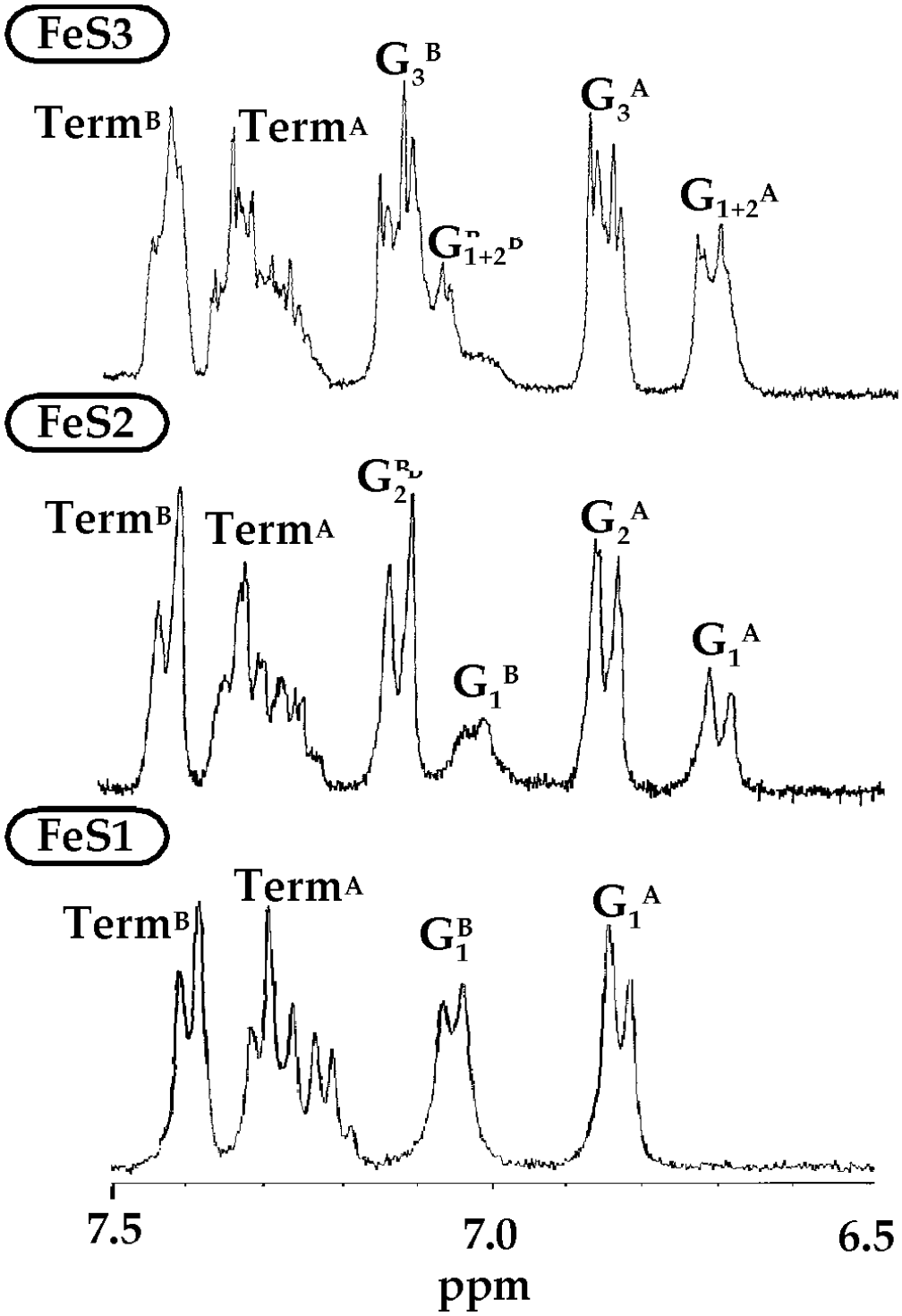

Figure 3.3. Aromatic regions of the ^{1}H NMR spectra of FeS1, FeS2, and FeS3.

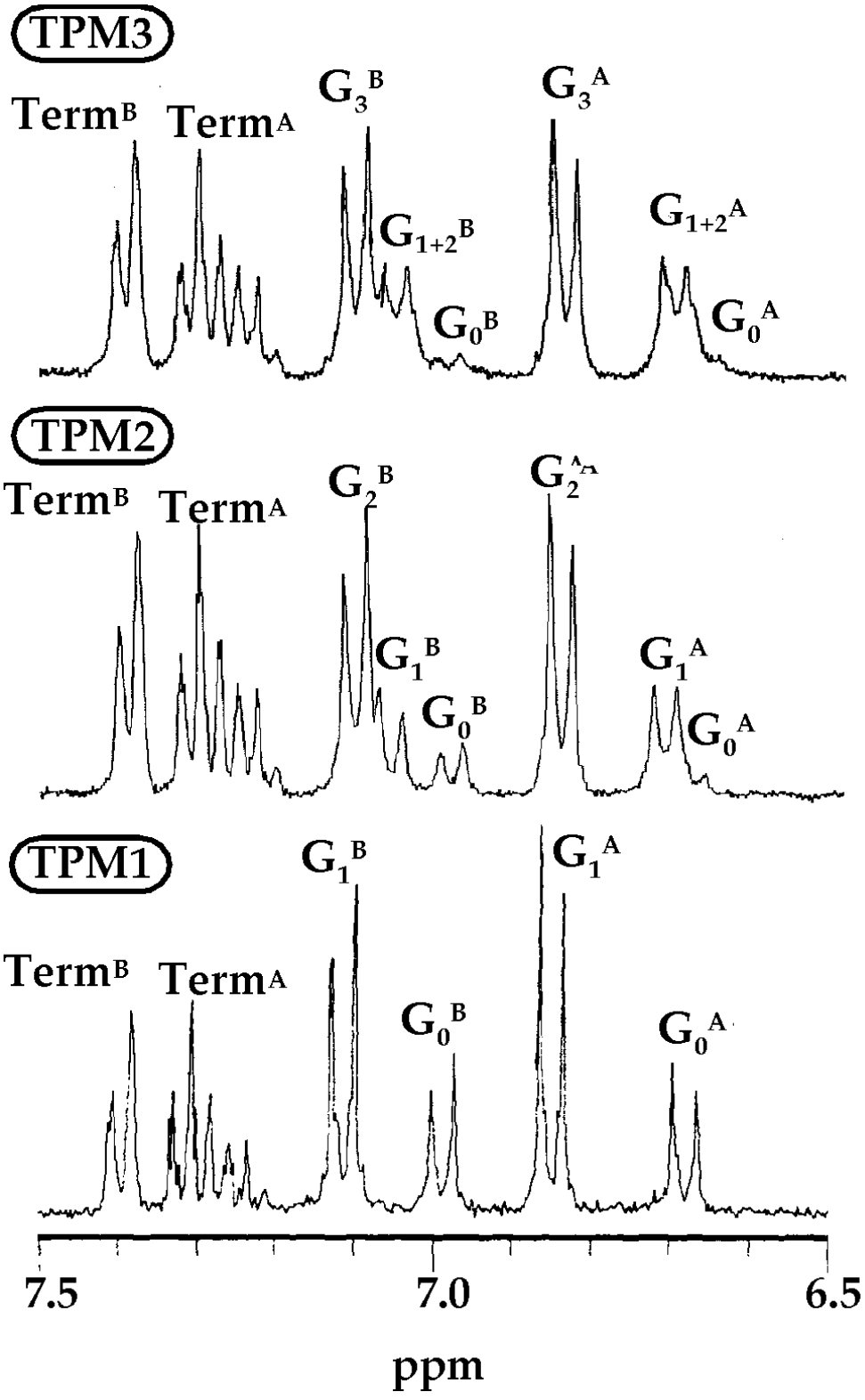

Figure 3.4. Aromatic regions of the ^{1}H NMR spectra of TPM1, TPM2, and TPM3.

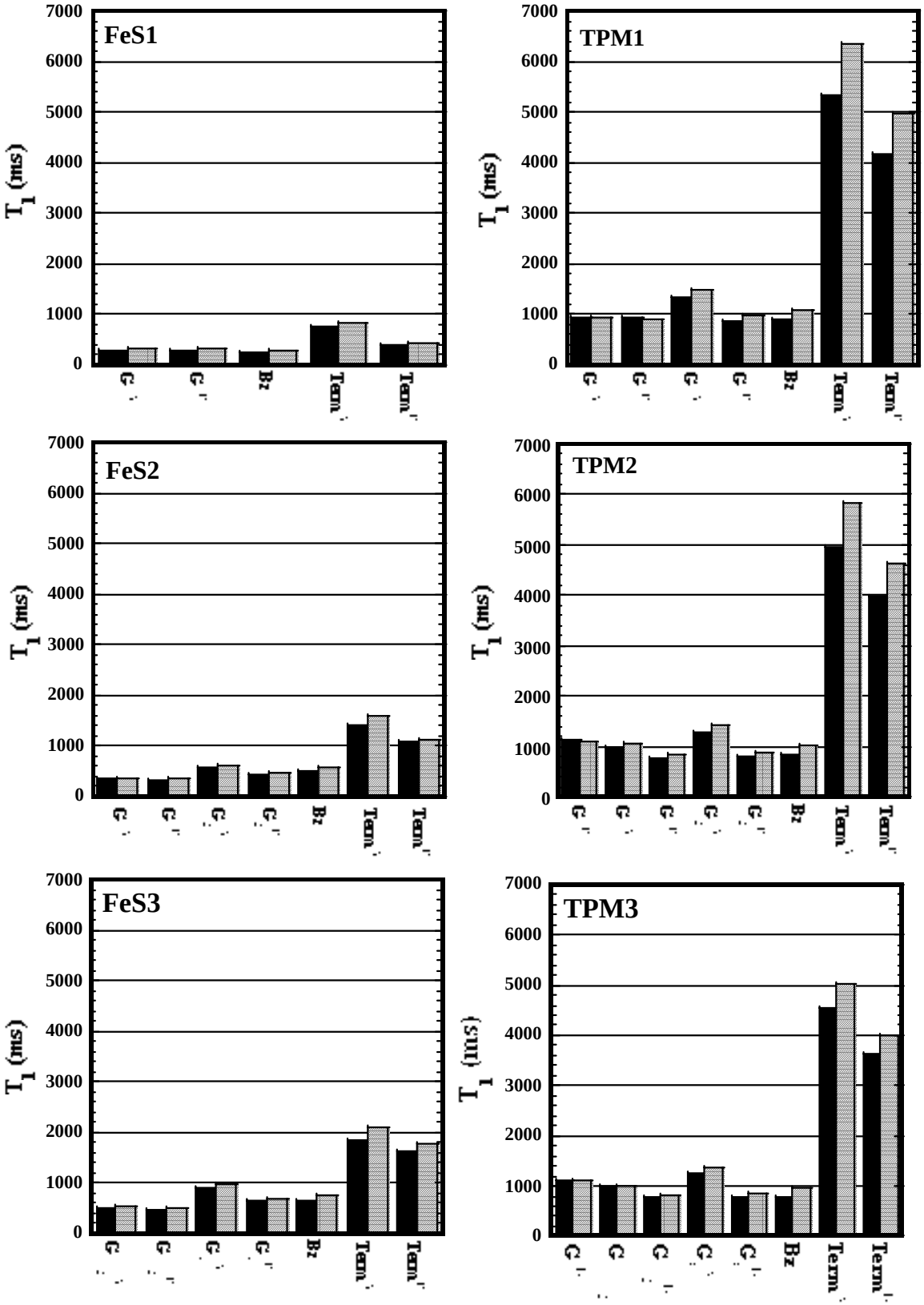

Figure 3.5. Tabulation of T_1 values at 25 °C (solid bars) and 40°C (dashed bars)

A model of dendrimer conformation in which different generations of the dendrimer are interspersed throughout its structure was supported by atomistic molecular dynamics simulations on these molecules. Figure 3.6 shows the radial density distribution of the different generations within a model of **FeS3** (in which the iron sulfur core was represented with a cubane core) averaged over the last 25 ps of a 100 ps molecular dynamics simulation. This graph shows the density (atom centers /unit volume) versus the distance from the molecular core. The radial density distributions calculated for **TPM3** were similar. This simulation depicted a compact, globular dendrimer with a trend in radial densities of each of the different generations that is consistent with the NMR relaxation data. Although this simulation is for a much shorter time scale than that of the NMR experiment, it illustrates that some of the protons at each generation of the dendrimer can come into close proximity to the core centered at 0 Å in Figure 3.6.

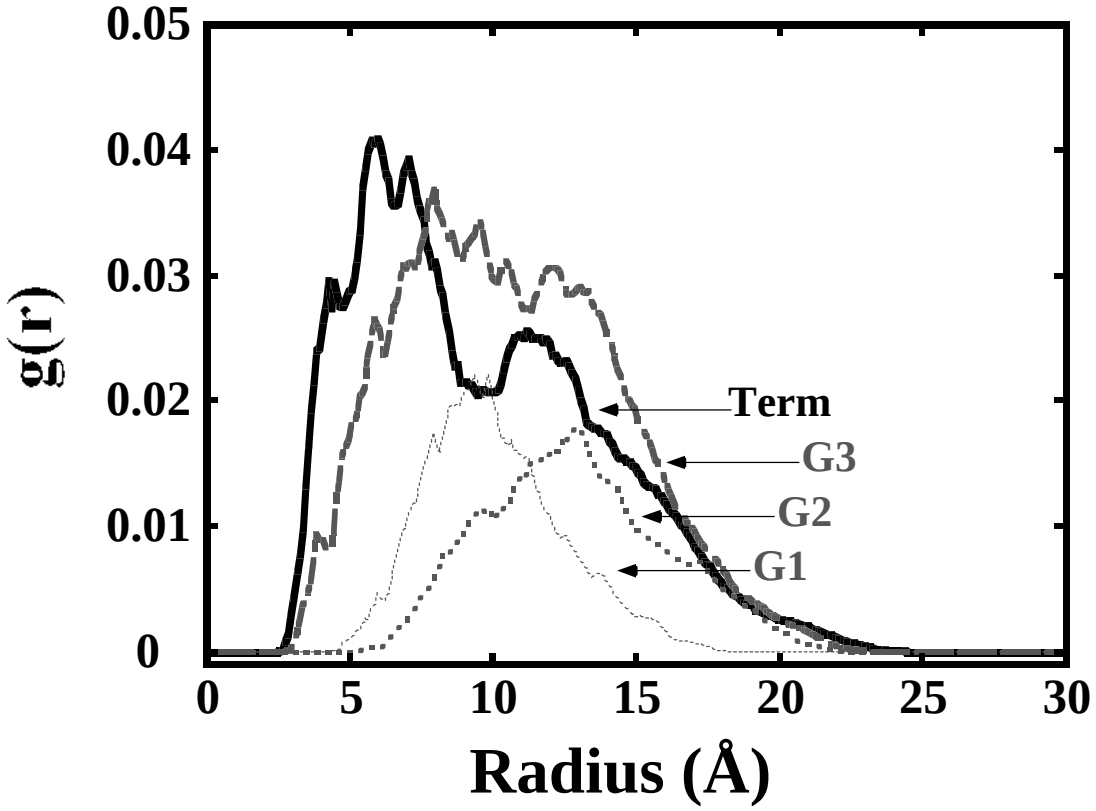

Figure 3.6. Radial density distribution functions of the generations (as designated in Figure 3.1) within a model of FeS3.

Because the conclusions mentioned are based on core-nuclei interactions, they assume that spin diffusion (a mechanism based on nuclei-nuclei interactions) is not important here.[40,41] This assumption should be reasonable for two reasons. First, if spin diffusion were operative in shortening the T_1 values of all the protons in the FeS dendrimers, these T_1 values should all be the same. While, the T_1 values of the topologically interior protons are similar, the T_1 values of the topologically exterior (e.g. $Term_A$ and $Term_B$) protons are quite different. Relaxation, particularly of the topologically exterior protons, is due to paramagnetic core effects and not spin diffusion. Second, the spin diffusion pathway requires nuclei-nuclei vectors to move at high frequencies. This scenario is most common in small molecules and not significant in molecules of this size.

3.2.3. The Inversion Recovery Experiment

The Inversion Recovery (IR) experiment measures nuclear spin relaxation for nuclei (^{1}H in the present study) exhibiting a distinctive resonance frequency. Nuclear spin relaxation is generally the process by which energized nuclei transfer excess magnetization to their environment. This process of magnetization (or energy) transfer causes the magnitude of the resonance signal to exponentially decay monotonically according to the equation

$$(M_o - M_z) = \ln(2) * \exp(M_o - \tau/T_1) \qquad \text{(Equation 3.1)}$$

where $(M_o - M_z)$ is the change in signal intensity, M_o is the equilibrium magnetization, and M_z is the z-component of the macroscopic magnetization. The parameter, τ, in the experimental pulse width or pulse delay. T_1 is the spin relaxation time constant and relates how fast relaxation occurs. Its inverse, τ_c, is known as the relaxation correlation time, and should not be confused with the τ in Equation 3.1.

IR is designed to measure the rate of change of the M_z component of the bulk magnetization over the duration of some time period, denoted, τ. (Figure 3.7) Figure 3.7 illustrates a standard 180-τ-90 IR pulse sequence used to obtain T_1 time constants. The diminution of the red arrow in Figure 3.7 represents the signal decay due to relaxation. The 90°-pulse at the end of the pulse width, τ, permits Fourier Transform detection of the M_z magnetization vector; which occurs for most instruments in the x,y plane.

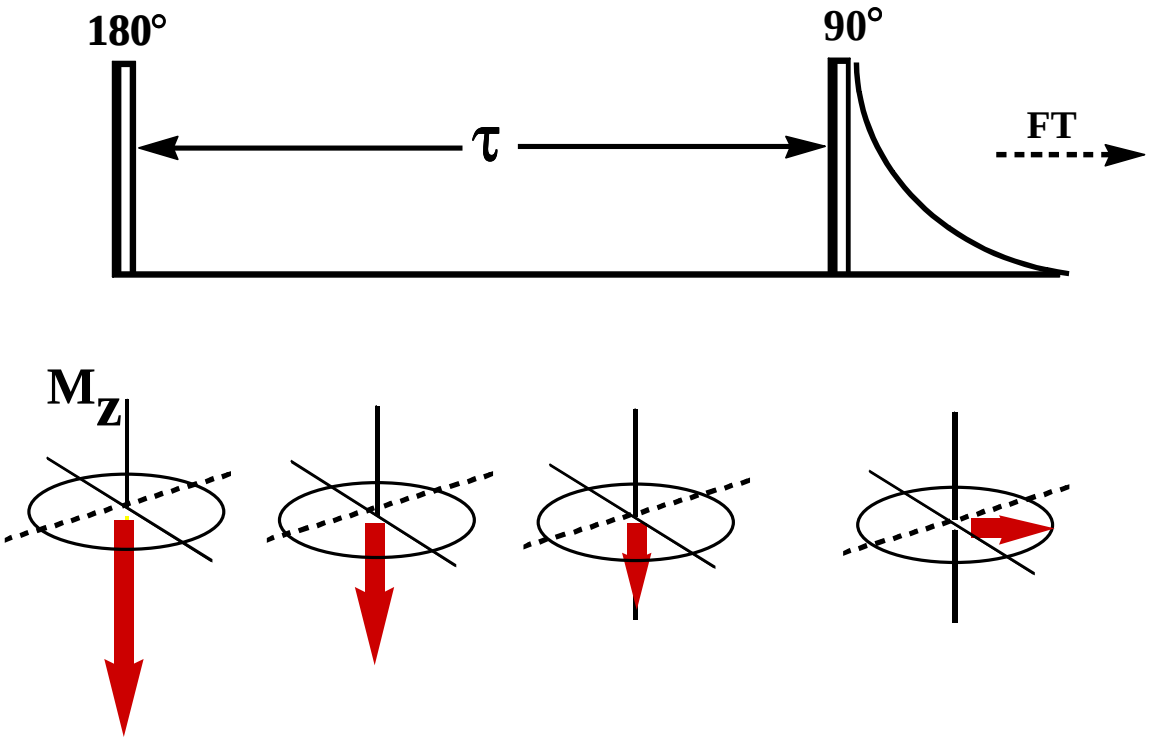

Figure 3.7. A schematic illustration of the 180-τ-90 pulse sequence used in the Inversion Recovery experiment. The red M_z vector is pointed up at the beginning of the experiment.

3.2.4. Relaxation Mechanisms

The trends in the NMR relaxation data can be rationalized by considering the likely mechanisms for nuclear spin relaxation in dendrimers. In the simplest sense, the magnetic motion (moving dipoles) in the microenvironment of a given nuclei serves as the major pathway for dissipating energy (relaxation). This mechanism is called dipole-dipole (DD) relaxation. In all of the molecules described here, relaxation can be attributed to dipole-dipole (DD) relaxation[42-44] between two nuclei (in both the FeS or TPM dendrimers) and between a nucleus and the unpaired electron density at the core (in only the FeS dendrimers).

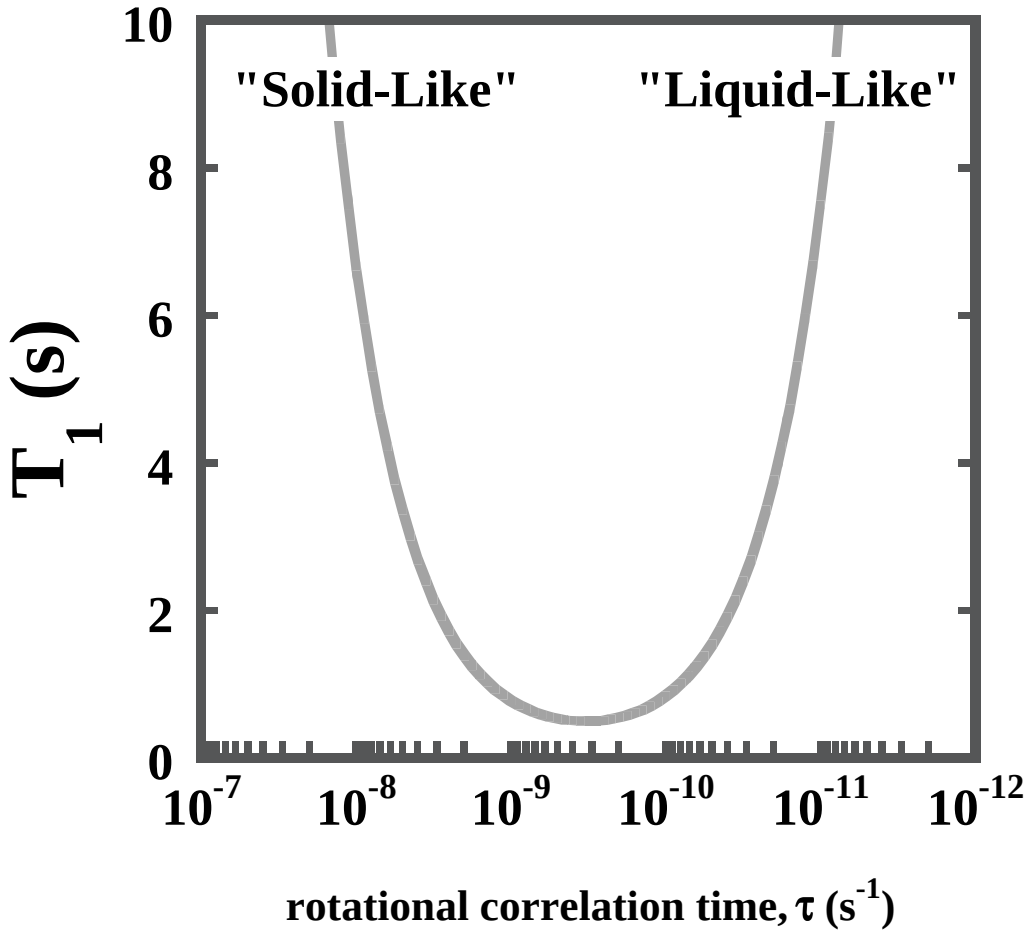

Figure 3.8. The dependence of T_1 on internuclear correlation time (τ) for two protons separated by 2 Å in a 300.522 MHz magnetic field.[56] This treatment assumes only DD relaxation between the two nuclei and the field and indicates the so-called solid-like and liquid-like regimes for relaxation as a function of internuclear motion.

DD relaxation is due to the motion of any number of internuclear vectors with respect to the applied magnetic field. To the extent that components of their motion oscillate at the Larmor frequency of the nuclei involved, these nuclei can couple to this field and relax. Thus, there is an optimal frequency of motion (τ) that gives rise to the most efficient DD relaxation and the lowest T_1 time constant. This idea is illustrated generally in Figure 3.8.[57] Oscillation of this internuclear vector that is slower than the Larmor frequency results in less than optimal efficiency of relaxation. Such motion is found for molecules in a so-called "solid-like" regime. Likewise, oscillation of this internuclear vector that is

faster than the Larmor frequency results in less than optimal efficiency of relaxation. Such motion is found for molecules in a so-called “liquid-like” regime.

Figure 3.8 should not be used to quantitatively predict T_1 from τ (the internuclear vector correlation time with respect to the applied magnetic field). This curve was generated for two nuclei interacting through-space at a fixed distance from one another (2 Å). In a real molecule, nuclei are probably farther apart from one another on average. Thus, the y-axis values of this curve probably represent the minimized relaxation time constants. This curve will shift upwards when one considers longer internuclear distances. However, its shape will not change. Thus, the usefulness of this curve is in predicting the *relative* T_1 for different τ values.

In addition, efficient DD relaxation depends on three additional things. The internuclear distance should be small (less than a few Ångstroms) as suggested by Figure 3.2. Specifically, the efficiency of relaxation will decrease with increasing internuclear distance to the sixth power. The angle of oscillation of the internuclear vector with respect to the applied field is also a consideration. It is generally not important in fluid solution as no preferred orientation of the molecules with respect to each other or with the applied magnetic field exists. Finally, the magnitude of the motion of the internuclear vector with respect to the applied magnetic field is important, with a larger magnitude affording more efficient relaxation.

Chemical environment plays an important role in the efficiency of DD relaxation, and such environmental effects are notable in the data shown in Figure 3.5. Most obvious is the difference in T_1 values between benzyl protons and phenyl protons. Moreover, the more upfield signal in the AA’XX’ patterns (those denoted G_n^A in Figure 3.3 and in Figure 3.4) have a longer relaxation time constant than the more downfield signal in these patterns (those denoted G_n^B). These differences are not unexpected as they reflect substantial local geometric differences in the different functional groups. These differences are generally consistent for protons in different generations and thus are of no value in a discussion of conformation.

Other mechanisms for nuclear relaxation such as chemical shift anisotropy (oriented dipole-dipole mechanism) and scalar coupling (through-bond mechanism) are unlikely to give rise to the trends illustrated here. These mechanisms are generally insignificant in fluid solution for nonbonded nuclei that are rapidly re-orienting themselves on the timescale of the experiment. This was also the conclusion of Meltzer et al. in a study of T_1 relaxation of ^{13}C nuclei in another type (PAMAM) of dendrimer structure.[36]

3.2.5. Characterizing the Dendrimer Interior

The interior of proteins is known to resemble the solid-state due to the close-packing of amino acid residues within a hydrogen-bond network[45,46] Since the dendrimers considered here do not incorporate any secondary non-covalent interactions, their interior most probably resembles the liquid-state by comparison.

Temperature dependent studies done here indicate the indeed that the molecules in this study are all in the liquid-like regime. This conclusion was made by considering the change in T_1 as the temperature was slightly elevated. It was not our intention to use temperature to widely vary correlation time and thus T_1 as it is not clear that one can predict either how the microviscosity within the dendrimer or how its conformational manifold might change with temperature. This small perturbation, however, should serve to increase somewhat the internuclear motion in the dendrimer, thus decreasing the internuclear correlation time (Figure 3.8). In all cases here, T_1 remained constant or increased. This behavior is consistent with internuclear correlation times in the liquid-like regime, probably near the T_1 minimum.

The trends in T_1 illustrated here reflect more motions than just overall rotation of the molecules. This is the case despite the fact that overall rotational motion leads to the largest amplitude of oscillation of internuclear vectors with respect to the applied magnetic field and thus is generally considered the most important factor in relaxation

effects. This conclusion was made by estimating the overall rotational correlation time of each dendrimer and noting that these times are longer than would be expected from the temperature dependent T_1 behavior mapped out in Figure 3.5.

Specifically, the overall rotational correlation times of **TPM1, TPM2** and **TPM3** were estimated from their average radii as computed from the molecular dynamics simulations described above. Average radii over the molecular dynamics trajectories of 10 Å, 14 Å, and 18 Å were computed for **TPM1**, **TPM2** and **TPM3**, respectively. These radii can be used to estimate the correlation time from the Stokes-Einstein equation

$$\tau_r = \frac{4\pi\eta a^3}{3kT} \qquad \text{(Equation 3.2)}$$

where η is the viscosity of THF (0.46×10^{-3} (J•s)/m^3 at room temperature),[47] k is Boltzmann's constant (1.38×10^{-23} J/K), T is absolute temperature and *a* is the average radius of the dendrimer. This computation leads to overall rotational correlation times of 4.685×10^{-10}, 1.286×10^{-9}, and 2.733×10^{-9} s for **TPM1**, **TPM2** and **TPM3**, respectively. These times are computed to change by less than 5% between 298 and 313K assuming no change in solvent viscosity or dendrimer conformation over this temperature range. (Table 3-1) No change in T_1 at elevated temperature is predicted by this approximation. Since this is not observed experimentally, rotational motion is not an accurate approximation for the dynamics processes at play in these dendrimers.

Moreover, based on the relationship between T_1 and τ shown in Figure 3.8, one would expect "solid-like" relaxation behavior for **TPM3** and **FeS3** dendrimers if molecular rotation was the only type of motion responsible for DD relaxation. In other words, T^1 should decrease at elevated temperatures. This type of behavior is not observed experimentally. Again, this indicates that overall molecular rotation is not the whole story here.

Table 3-1. Rotational correlation times for TPM1, TPM2, and TPM3 dendrimers at the specified temperatures using Equation 3.2 and 10 Å, 14 Å, and 18 Å respectively for the average molecular radii.

Molecule	τ_c @ 298 K (25 °C)	τ_c @ 313 K (40 °C)
TPM1	4.685×10^{-10}	4.461×10^{-10}
TPM2	1.286×10^{-9}	1.224×10^{-9}
TPM3	2.733×10^{-9}	2.602×10^{-9}

3.2.6. Conformational Flexibility

Using the analysis given above, one can come to some conclusion about the relative conformational flexibility of the different generations within the dendrimer. The T_1 values of many of the protons change very little with a change in temperature. Many of the differences are within the 5% error attributed to the experiment. Invariance of T_1 with temperature could be attributed to nuclei with a correlation time corresponding to the T_1 minimum (Figure 3.8). However, the values of T_1 measured here seem large for this regime. More likely, most of the interior nuclei are well-packed and have some but not a great deal of high frequency motion. In the spectrum of dynamic motion, these molecules are midway between small molecules that are moving about rapidly and protein macromolecules that are rigid networks of amino acids residues. This situation seems appropriate for globular macromolecules. Such a model would also account for the relative invariance of T_1 for the interior but topologically distinctive nuclei in the TPM dendrimers — new avenues for either additional motion or much of an increase in the frequency of motion do not become available with this small increase in temperature. In any event, these interior nuclei appear to be attached to groups with similar conformational flexibilities. The resolution of the NMR signals for different protons as highlighted in Section 3.2.2 makes this conclusion believable.

Upon close examination, one can discern more of a difference in T_1 with respect to generation in the FeS dendrimers compared to the TPM dendrimers. This small

difference can be attributed to the different radial density distributions with respect to the paramagnetic core of nuclei in different generations. (Figure 3.6, for **FeS3**) However, this effect is obviously not large. This observation is again consistent with a model of dendrimer conformation in which all of the topologically different nuclei are radially distributed throughout the structure.

The terminal protons ($Term_A$ and $Term_B$) in both sets of dendrimers behave differently from the other nuclei. Their T_1 values are longer. Moreover, they exhibit a greater temperature dependence of T_1 over the small range studied. Both of these behaviors are consistent with increased motion of these peripheral groups as compared to all others in the molecules. As depicted in Figure 3.8, high frequency motion (low τ–values) results in increased T_1 values. This motion is most probably rapid rotation of these benzene rings. However other motions certainly exist as well.

The existence of this type of motion was supported by calculating the mean square displacement correlation functions for the atoms at each generation in the model of the **FeS3** dendrimer considered in Figure 3.1. Such a graph is shown in Figure 3.9 for the last 80 ps of the molecular dynamics run performed and described above. A molecular dynamics run of this duration is too short to be used in a meaningful calculation of the DD contribution to relaxation.[58] However, in this short period, one can distinguish very different relative mobilities of groups. Indeed, in Figure 3.9, the terminal groups in the molecule are predicted to move about much more than any of the interior groups.

This relatively higher mobility reflects that of an average terminal group in a given dendrimer. Terminal groups close to the core would probably be much less mobile on this short time scale (100 ps). Terminal groups closer to the geometric periphery of the molecule would understandably be more mobile. These data, thus, reflect an average behavior. Likewise, the relaxation data reflect an average of all T_1 values. In particular, an attenuated T_1 value due to the presence of a paramagnetic core gives a qualitative indication that some but not necessarily all of the members in a topologically identical group approach the core closely on the time scale of the NMR experiment.

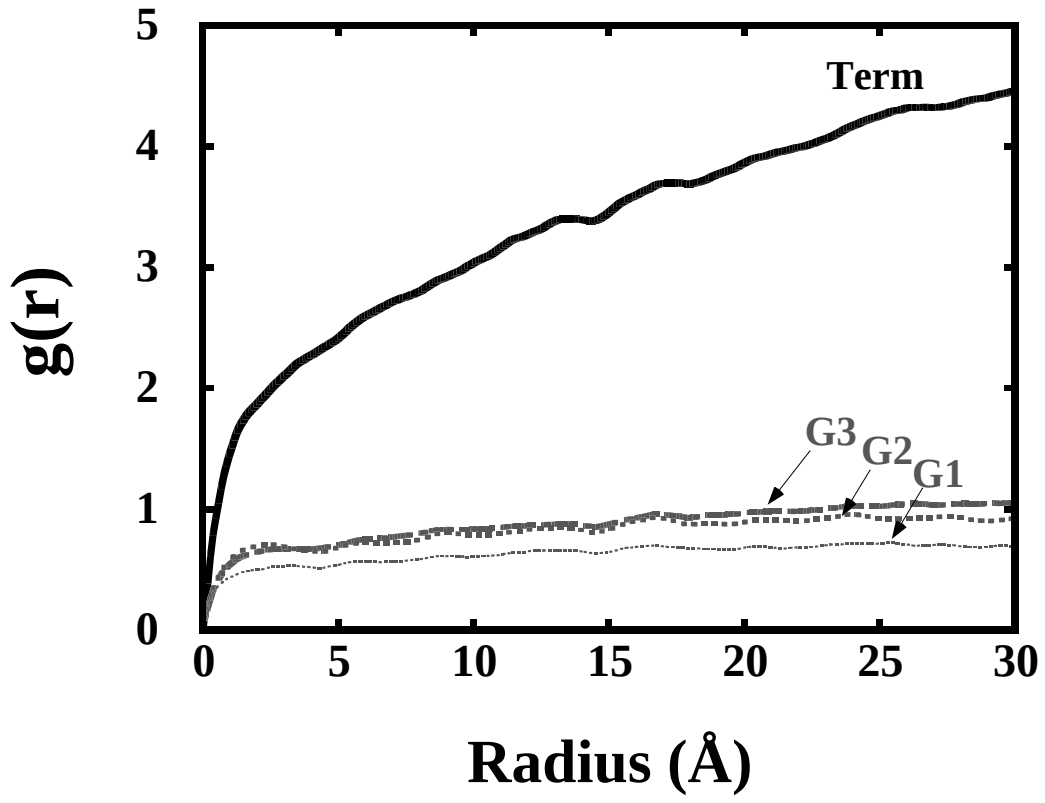

Figure 3.9. Mean square displacement correlation functions of the generations (as designated in Figure 3.1) for a model of FeS3.

3.3. Conclusions

Dendrimers with paramagnetic cores offer a handle for qualitatively evaluating some general conformational features of dendrimers. Specifically, the attenuation of T_1 values for protons in paramagnetic core dendrimers as compared to those in similar diamagnetic core dendrimers indicate a dendrimer structure in which, on average, the protons in each different generation of a dendrimer approach the core of the molecule closely in space. This conclusion agrees with the computed radial density distributions of these different generations that could be calculated from molecular dynamics simulations.

These T_1 values as well as their change with a slight change in temperature also suggest liquid-like mobility, most particularly for the terminal groups on the dendrimer. This observation is consistent with geometric distribution of terminal groups in which many, but not all, are at the geometric exterior of the dendrimers and are thus capable of more segmental motion. This conclusion is supported by the computed mean square displacement correlation functions for the different generations that could be calculated from molecular dynamics simulations.

These observations support a model of a dendrimer with a compact, yet liquid-like, interior and a more mobile exterior. This packed interior, however, does not find the topologically most central groups exclusively at the geometric center of the molecule. Rather, over the time scale of the experiment, some members of each of the different generations within the dendrimer establish a position close to the core of the molecule as well. These conclusions are consistent with recent computational predictions about dendrimer conformation[48-52] and help to provide a general physical picture for dendrimer conformation and flexibility that, to date, has enjoyed only modest experimental support.

3.4. Experimental

Synthesis of FeS dendrimer series. Molecules were available from a previous study.[26]

Synthesis of the TPM dendrimer series. The synthesis of the **TPM** dendrimers was carried out by Dr. Michael W. Hager. Detailed procedure and characterization data are available.[26]

Measurement of T_1 values. T_1 values were measured using a standard 180-τ-90 IR pulse sequence. Tetrahydrofuran-d_8 was employed as the solvent as all six of the dendrimers under consideration were soluble in this solvent. Dilute (10^{-4} M) solutions were employed to avoid intermolecular relaxation effects between dendrimers. At higher concentrations of dendrimer, smaller T_1 values were obtained, indicative of some

intermolecular relaxation at these higher concentrations. Variable delays (τ) were selected to span a range sufficient to probe relaxation up to five times the T_1 values of all of the protons under consideration. A minimum of 10 τ values were employed. Integrals of the proton signals versus τ were plotted and fit to a three parameter fit using the procedure of Levy and Peat.[53] A 5% standard error in integration was found to be the major source of error in the measurement.

Molecular Dynamics Simulations. All simulations were performed on a Silicon Graphics INDIGO2 R4400 workstation using BIOSYM modules INSIGHTII and DISCOVER (3.0.0). The all-atom 'consistent valence forcefield' (CVFF) which includes explicit hydrogens was used for molecular mechanics and molecular dynamics. Atoms were treated as interacting points held together by potential energy terms. Bonded interactions considered were bond stretching, angle bending, torsion and out-of-plane bending. Nonbonded van der Waals interactions were treated with a 12-6 Lennard-Jones function and electrostatic interactions were calculated with a non-distance dependent dielectric constant. The Verlet velocity algorithm was used for integrating equations of motion during molecular dynamics.

A simulated annealing protocol was implemented to generate a reasonable minimum energy structure on which to collect structural data. Bonds were constrained to their equilibrium distances using the RATTLE algorithm (velocity version of SHAKE) permitting the use of a 2 fs timestep.[54,55] A nonbond cutoff limit of 9.5 Å was used as well.

The simulated annealing procedure involved 100 ps of high temperature dynamics at 600K to ensure adequate sampling of the potential energy surface. Subsequently, the system was cooled to 50K at a rate of 20K/ps; and minimized to a maximum derivative less than 0.001 kcal*mol^{-1}Å^{-1}. This structure was subjected to 20 ps of low temperature dynamics at 273K to attain dynamic equilibrium and subsequently sampled for an additional 80 ps. Trajectory coordinates were recorded every 100 fs. Radial density distribution functions (RDF) and molecular radii were averaged over the last 25 ps of this

trajectory. Mean Square Displacement correlation functions (MSD) were tabulated for the last 80 ps of this trajectory. For the FeS dendrimer series, the iron-sulfur core was replaced by cubane to fulfill the valence requirements of the forcefield atom types.

3.5. References and Notes

1)Wallimann, P.; Seiler, P.; Diederich, F. *Helv. Chim. Acta* **1996**, *79*, 779-788.

2)Aoi, K.; Itoh, K.; Okada, M. *Macromolecules* **1995**, *28*, 5391-5393.

3)Turro, N. J.; Barton, J. K.; Tomalia, D. A. *Acc. Chem. Res.* **1991**, *24*, 332-340.

4)Watanabe, S.; Regen, S. L. *J. Am. Chem. Soc.* **1994**, *116*, 8855-8856.

5)Wells, M.; Crooks, R. M. *J. Am. Chem. Soc.* **1996**, *118*, 3988-3989.

6)Bar, G.; Rubin, S.; Cutts, R. W.; Taylor, T. N.; Zawodzinski, T. A. *Langmuir* **1996**, *12*, 1172-1179.

7)Saville, P. M.; Reynolds, P. A.; White, J. W.; Hawker, C. J.; Fréchet, J. M. J.; Wooley, K. L.; Penfold, J.; Webster, J. R. P. *J. Phys. Chem.* **1995**, *99*, 8283-8289.

8)Brunner, H. *J. Organomet. Chem.* **1995**, *500*, 39-46.

9)Chang, H.-T.; Chen, C.-T.; Kondo, T.; Suizdak, G.; Sharpless, K. B. *Angew. Chem. Int. Ed. Engl.* **1996**, *35*, 182-186.

10)Jansen, J. F. G. A.; Meijer, E. W.; de Branbander-Van den Berg, E. M. M. *J. Am. Chem. Soc.* **1995**, *117*, 4417-4418.

11)Jansen, J. F. G. A.; Janssen, R. A. J.; de Branbander-Van den Berg, E. M. M.; Meijer, E. W. *Adv. Mater.* **1995**, *7*, 561-564.

12)Hawker, C. J.; Farrington, P. J.; Mackay, M. E.; Wooley, K. L.; Fréchet, J. M. J. *J. Am. Chem. Soc.* **1995**, *117*, 4409-4410.

13)Mourey, T. H.; Turner, S. R.; Rubinstein, M.; Fréchet, J. M. J.; Hawker, C. J.; Wooley, K. L. *Macromolecules* **1992**, *25*, 2401-2406.

14)Percec, V.; Chu, P.; Ungar, G.; Zhou, J. *J. Am. Chem. Soc.* **1995**, *117*, 11441-11454.

15)Hawker, C. J.; Wooley, K. L.; Fréchet, J. M. J. *J. Am. Chem. Soc.* **1993**, *115*, 4375-4376.

16)Dandliker, P. J.; Diederich, F.; Gross, M.; Knobler, C. B.; Louati, A.; Sanford, E. M. *Angew. Chem. Int. Ed. Engl.* **1994**, *33*, 1739-1741.

17)Dandliker, P. J.; Diederich, F.; Gisselbrecht, J.-P.; Louati, A.; Gross, M. *Angew. Chem. Int. Ed. Engl.* **1995**, *34*, 2725-2727.

18)Janssen, R. A. J.; Jansen, J. F. G. A.; van Haare, J. A. E. H.; Meijer, E. W. *Adv. Mater.* **1996**, *8*, 494-496.

19)Sadamoto, R.; Tomioka, N.; Aida, T. *J. Am. Chem. Soc.* **1996**, *118*, 3978-3979.

20)Tomoyose, Y.; Jiang, D.-L.; Jin, R.-H.; Aida, T.; Yamashita, T.; Horie, K.; Yashima, E.; Okamoto, Y. *Macromolecules* **1996**, *29*, 5236-5238.

21)Ihre, H.; Hult, A.; Söderlind, E. *J. Am. Chem. Soc.* **1996**, *118*, 6388-6395.

22)Wiener, E. C.; Auteri, F. P.; Chen, J. W.; Brechbiel, M. W.; Gansow, O. A.; Schneider, D. S.; Belford, R. L.; Clarkson, R. B.; Lauterbur, P. C. *J. Am. Chem. Soc.* **1996**, *118*, 7774-7782.

23)Ottaviani, M. F.; Montalti, F.; Romanelli, M.; Turro, N. J.; Tomalia, D. A. *J. Phys. Chem.* **1996**, *100*, 11033-11042.

24)Ottaviani, M. F.; Cossu, E.; Turro, N. J.; Tomalia, D. A. *J. Am. Chem. Soc.* **1995**, *117*, 4387-4398.

25)Ottaviani, M. F.; Bossman, S. H.; Turro, N. J.; Tomalia, D. A. *J. Am. Chem. Soc.* **1994**, *116*, 661-671.

26)Gorman, C. B.; Parkhurst, B. L.; Chen, K.-Y.; Su, W. Y. *J. Am. Chem. Soc.* **1997**, *119*, 1141-1142.

27)González-Moraga, G. *Synthetic Analogues of the Active Sites of Iron-Sulfur Proteins*; González-Moraga, G., Ed.; Springer-Verlag: New York, 1993, pp 278-295.

28)Babini, E.; Bertini, I.; Borsari, M.; Capozzi, F.; Dikiy, A.; Eltis, L. D.; Luchinat, C. *J. Am. Chem. Soc.* **1996**, *118*, 75-80.

29)Agarwal, A.; Li, D.; Cowan, J. A. *J. Am. Chem. Soc.* **1996**, *118*, 927-928.

30)Averill, B. A.; Herskovitz, T.; Holm, R. H.; Ibers, J. A. *J. Am. Chem. Soc.* **1973**, *95*, 3523-3534.

31)Que Jr., L.; Bobrik, M. A.; Ibers, J. A.; Holm, R. H. *J. Am. Chem. Soc.* **1974**, *96*, 4168-4177.

32)DePamphilis, B. V.; Averill, B. A.; Herskovitz, T.; Que Jr., L.; Holm, R. H. *J. Am. Chem. Soc.* **1974**, *96*, 4159-4167.

33)Holm, R. H.; Phillips, W. D.; Averill, B. A.; Mayerle, J. J.; Herskovitz, T. *J. Am. Chem. Soc.* **1974**, *96*, 2109-2117.

34)Holm, R. H. *Acc. Chem. Res.* **1977**, *10*, 427-434.

35)Herskovitz, T.; Averill, B. A.; Holm, R. H.; Ibers, J. A.; Phillips, W. D.; Weiher, J. F. *Proc. Nat. Acad. Sci.* **1972**, *69*, 2437-2441.

36)Meltzer, A. D.; Tirrell, D. A.; Jones, A. A.; Inglefield, P. T.; Hedstrand, D. M.; Tomalia, D. A. *Macromolecules* **1992**, *25*, 4541-4548.

37)Meltzer, A. D.; Tirrell, D. A.; Jones, A. A.; Inglefield, P. T. *Macromolecules* **1992**, *25*, 4549-4552.

38)Wooley, K. L.; Klug, C. A.; Tasaki, K.; Schaefer, J. *J. Am. Chem. Soc.* **1997**, *119*, 53-58.

39)Gorman, C. B.; Hager, M. W.; Parkhurst, B. L.; Smith, J. C. *Macromolecules* **1998**, *31*, 815-822.

40)Kalk, A.; Berendsen, H. J. C. *J. Magn. Reson.* **1976**, *24*, 343-366.

41)Eckman, R. R.; Henrichs, P. M.; Peacock, A. J. *Macromolecules* **1997**, *30*, 2474-2481.

42)Sanders, J. K. M.; Hunter, B. K. *Modern NMR Spectroscopy: A Guide for Chemists, 2nd Ed.*; Oxford University Press: New York, 1993.

43)Noggle, J. H.; Schirmer, R. E. *The Nuclear Overhauser Effect. Chemical Applications*; Noggle, J. H.; Schirmer, R. E., Ed.; Academic Press: New York, 1971, pp Chapter 2.

44)Bovey, F. A.; Jelinski, L.; Mirau, P. A. *Nuclear Magnetic Resonance Spectroscopy, 2nd. Ed.*; Bovey, F. A.; Jelinski, L.; Mirau, P. A., Ed.; Academic Press: New York, 1988, pp Chapter 5.

45)Richards, F. M. *Annual Review of Biophysics and Bioengineering* **1977**, *6*, 151-176.

46)Richards, F. M. *Journal of Molecular Biology* **1974**, *82*, 1-14.

47)Snyder, L. R. *Introduction to Modern Liquid Chromatography, 2nd Ed.*; Snyder, L. R., Ed.; John Wiley and Sons, Inc.: New York, 1979, pp 248.

48)Chen, Z. Y.; Cui, S.-M. *Macromolecules* **1996**, *29*, 7943-7952.

49)Forni, A.; Ganazzoli, F.; Vacatello, M. *Macromolecules* **1996**, *29*, 2994-2999.

50)Mansfield, M. L.; Klushin, L. I. *J. Phys. Chem.* **1992**, *96*, 3994-3998.

51)Mansfield, M. L.; Klushin, L. I. *Macromolecules* **1993**, *26*, 4262-4268.

52)Murat, M.; Grest, G. S. *Macromolecules* **1996**, *29*, 1278-1285.

53)Levy, G. C.; Peat, I. R. *J. Magn. Reson.* **1975**, *18*, 500-521.

54)Lamy, A.; Smith, J. C. *J. Am. Chem. Soc.* **1996**, *118*, 7326-7328.

55)Wilson, M. A.; Pohorille, A. *J. Am. Chem. Soc.* **1996**, *118*, 6580-6587.

56) In addition, the effects of a paramagnetic ion as a magnetic resonance contrast agent are increasingly employed. For an interesting recent example, see: Moats, R. A.; Fraser, S. E.; Meade, T. J. *Angew. Chem. Int. Ed. Engl.* **1997**, *36*, 726-728.

57) This curve was calculated at an internuclear separation of 2 Å using a program employing the GAMMA function library. This library is available from (http://gamma.magnet.fsu.edu/download/packages/). The program upon this calculation was based is available from (http://gamma1.magnet.fsu.edu/~gamma/htmldox/relax/dipolar.fm45.html) Literature reference to these calculations is given as: Smith, S. A.; Levante, T. O.; Meier, B. H.; Ernst, R. R. *J. Magn. Reson.* **1994**, *106a*, 75-105.

58) A power spectrum of amplitude of internuclear motion versus frequency can be used to compute T_1 assuming a DD relaxation mechanism. However, this requires a molecular dynamics simulation on the order of 100 nanoseconds to obtain a spectrum at the relevant frequencies. Such a computation has been performed recently for a small cyclic oligopeptide: Bremi, T.; Brüschweiler, R.; Ernst, R. R. *J. Am. Chem. Soc.* **1997**, *119*, 4272-4284.

CHAPTER 4

EFFECT OF REPEAT UNIT FLEXIBILITY ON DENDRIMER CONFORMATION AS STUDIED BY MOLECULAR DYNAMICS SIMULATIONS

This work was the subject of a publication, Gorman, C. B.; Smith, J. C. *Polymer* **1999**, *in press.*

4.1. Introduction

It is of great interest to elucidate the geometric features of dendrimers such as their shape, size, and internal organization. To this end, a number of experimental and computational approaches have been devised to provide a physical picture of dendrimer conformation; including their overall shape and their internal structure. However, to date, this picture of dendrimer conformation is far from complete. Most notably, the effect of the primary structure of the dendrimer on its overall three-dimensional structure has not been elucidated. Thus, little information is available for the development of rational design strategies and establishment of molecular structure-property relationships. Such information will be essential to the successful rational implementation of dendrimers in novel materials and applications.

A number of computations have been devised to elucidate dendrimer conformation. Initially, Lescanec and Muthukumar[1] reported kinetic-growth simulations predicting a density maximum at the topological center of dendrimer models with radially scattered branch ends at advanced stages of dendrimer growth (i.e. high generations). More recently, this general picture has been supported using coarse-grain molecular dynamics simulations,[2] coarse-grain Monte Carlo simulations,[3-7] and coarse-grain self-consistent field calculations.[8] Likewise in these cases, repeat units closer to the topological periphery of the models were dispersed throughout the geometric interior of the model. These predictions have been confirmed in flexible molecules using REDOR NMR experiments on appropriately functionalized dendrons[9] and, more recently, by NMR relaxation studies on paramagnetic core dendrimers.[10]

Coarse-grain models, however, treat molecules as a set of identical points interacting according to simple bonding and self-exclusion forces. Algorithms for evaluating their conformational manifold consider only basic enthalpic contributions arising from these generic bonding and self-exclusion energy terms. Atomistic molecular dynamics simulations (MDS) based on chemically specific potential energy terms would

complement simplified models of the type cited above. To date, although the effect of the number of hyperbranches on molecular shape has been illustrated in one system using short, atomistic MDS,[11] little additional structural information is available. The results mentioned above have been generated exclusively for dendrimers composed of flexible units (i.e. those containing mostly low energy torsional barriers). High interior density due to molecular folding may or may not persist as the flexibility of the repeat unit is varied.

In this section, the effect of conformational flexibility of a dendrimer repeat unit and generation (i.e. the number of hyperbranches within the molecule) on the overall geometry and organization of a dendrimer is studied using atomistic molecular dynamics simulations. This relationship is explored over a size range of dendrimer models that are computationally feasible to equilibrate and constitute reasonable synthetic targets. Repeat units that are alternatively "flexible" and "stiff" are compared. In contrast to course-grain calculations [2,3-7,1,8] using ball-and-stick models, these simulations were performed to provide a detailed atomistic picture of dendrimer conformation.

4.2. Results and Discussion

4.2.1. Structures Under Consideration

A series of molecular dynamics simulations was performed to compare and contrast the shape and internal organization of different dendrimers with repeat units that were alternatively flexible and stiff. To maximize the practical utility of these computations, repeat units commonly reported in the literature were chosen. This approach does not merely indicate the effect of repeat unit stiffness on overall structure as these molecules have other differences. Variation of repeat unit flexibility by, for example, artificially changing a torsion barrier in the forcefield employed would permit a continuous mapping of this parameter on overall dendrimer structure. However, such results cannot be correlated in a straightforward fashion with real chemical systems. Thus, the former method has been employed here.

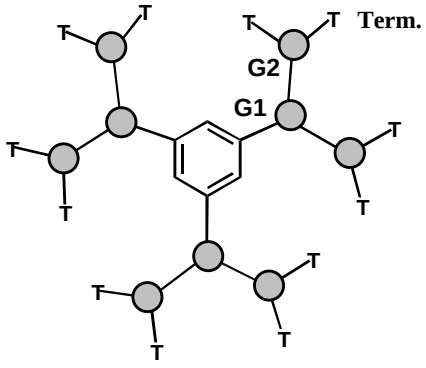

Dendrimer -21

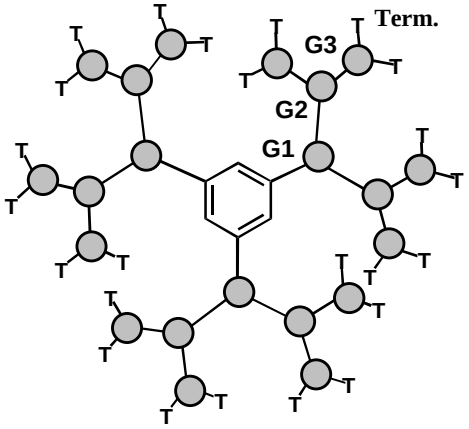

Dendrimer-45

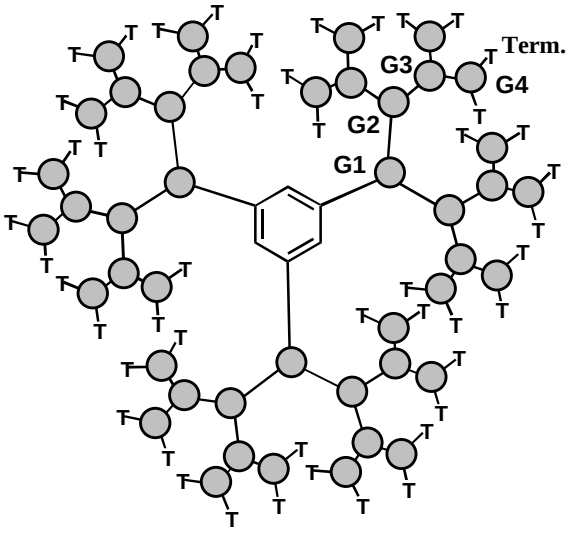

Dendrimer-93

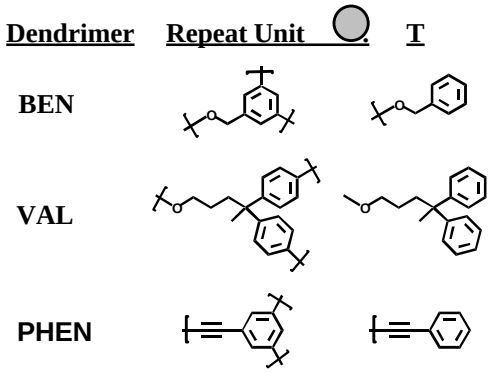

Figure 4.1. Structures employed in this study. The numbers 21-, 45-, and 93- preceding the dendrimer label denote the number of repeat units in the structure. G1, G2, Gn refer to the group of repeat units at the nth hyperbranch point in the molecule. Term. denotes the group of repeat units located at the topological periphery in each of the models.

The structures of the dendrimers under study are depicted in Figure 4.1. The designation "generation" is used here to refer to a topological group of repeat units within a given dendrimer. Thus, generation 1 (G1) refers to the three repeat units covalently bonded to the benzene core of the molecule. In a similar fashion, generation n (Gn) refers to daughters covalently bonded to Gn-1. Molecules are referred to by the number of repeat

units in the structure (i.e. DENDRIMER-21, DENDRIMER-45, and DENDRIMER-93). Dendrimers based upon the units termed BEN (for a 3,5-dibenzyloxy repeat unit)[12,13] and VAL (for a 4,4´-diphenyl-isovaleroxy repeat unit)[14] have been reported previously by Fréchet et al. These two units were chosen to represent flexible repeat unit dendrimers. The VAL unit is more flexible than the BEN unit because of the greater number of low energy torsions in its methylene chain. It is also larger than the BEN unit and thus gives an indication of how molecular weight influences dendrimer structure for molecules with the same number of hyperbranches. Dendrimers based upon the PHEN unit have been reported previously by Moore et al.[15-18] and were chosen to represent a rigid repeat unit dendrimer. All of these units have no specially designed features such as hydrogen-bonding or extreme steric bulk within the units. Such features may have notable effects on the overall shape and organization of the dendrimer. These effects have not been treated here. Additionally, the core of the dendrimer models studied here is a 1,3,5-trisubstituted benzene moiety. Although not all of the dendrimer molecules reported in the literature had this core, it was used here so as not to bias the observed differences in the dendrimers studied by an additional variable.

4.2.2. Molecular Shape

The rigidity of the repeat unit has been suggested to be a dominant factor in controlling dendrimer shape.[17,19-25] The results of the simulations reported here are also consistent with this hypothesis. Figures 4.2 and 4.3 show snapshots of dendrimer models during simulations. These depict the shape differences among the alternatively flexible (Figure 4.2) and stiff (Figure 4.3) architectures. These models are snapshots of the molecules at the midpoint of the production dynamics and are representative of the shapes of the molecules during the course of the simulations. In these depictions, the terminal groups of each dendrimer are shaded lighter than the other groups. The significance of these distributions will be discussed in detail below.

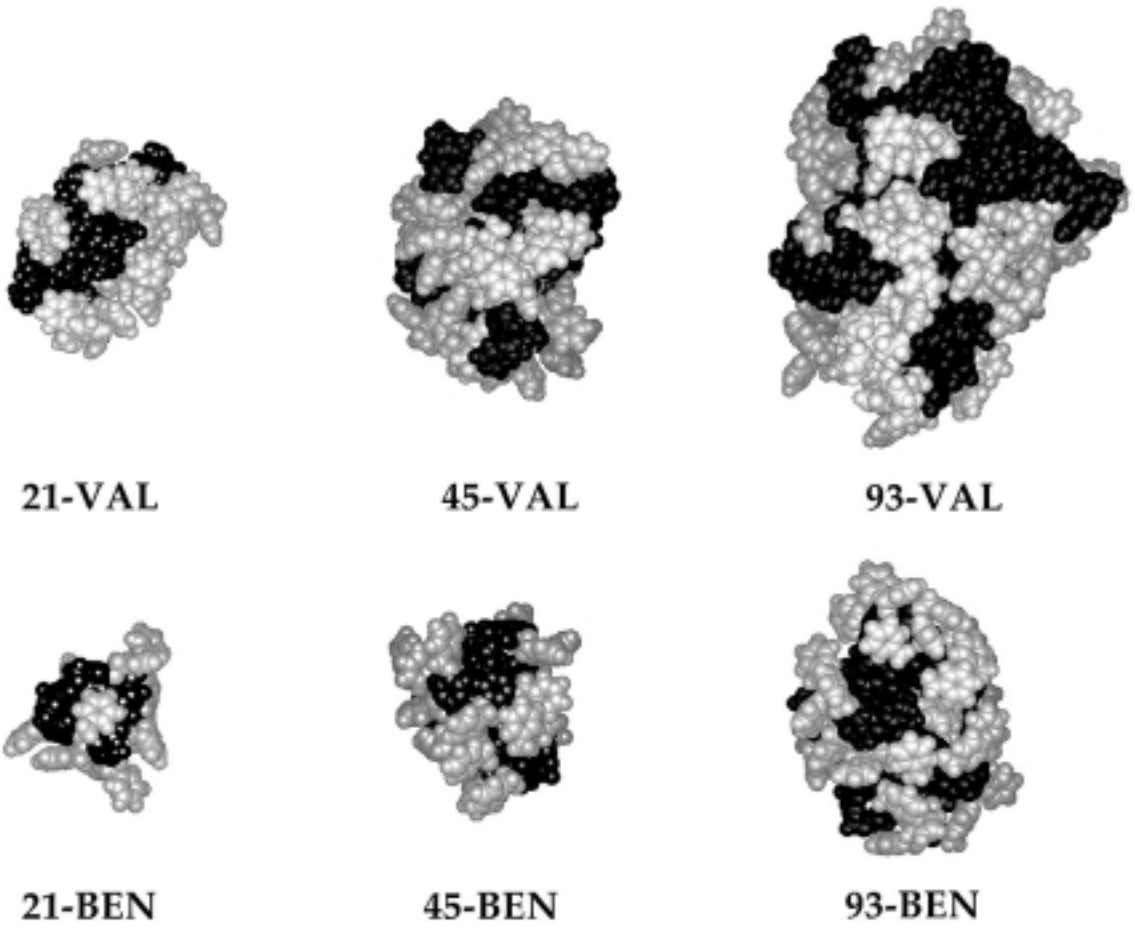

Figure 4.2. CPK models of VAL-and BEN-derived dendrimers obtained at the midpoint of the 500 ps production dynamics run. Repeat units at the Term. are colored light gray. All others are colored black.

The globular shapes found for the BEN and VAL dendrimers resulted from contraction of dendron arms around the topological core. This contraction was driven by interatomic van der Waals interactions as evidenced by a large change in the dispersive van der Waals energy component of the total energy expression during relaxation. Boris and Rubinstein have previously discussed the entropic favorability of this behavior.[8] The results presented here, however, are consistent with those generated using statistically rigorous coarse-grain models that consider entropy.[2-8] The dynamic shape of these dendrimers was illustrated by plotting their aspect ratio (i.e. calculated from principle moments of inertia, Iz/Ix, Figure 4.4) as it evolved during the course of the production phase of the simulation. The smallest flexible dendrimers (21-BEN and 21-VAL)

exhibited a large apparent change in shape during the course of the simulation. This change was due to substantial motion of the peripheral groups in these molecules. In these small molecule cases, the peripheral groups made up a substantial portion of the molecule and were uncrowded.

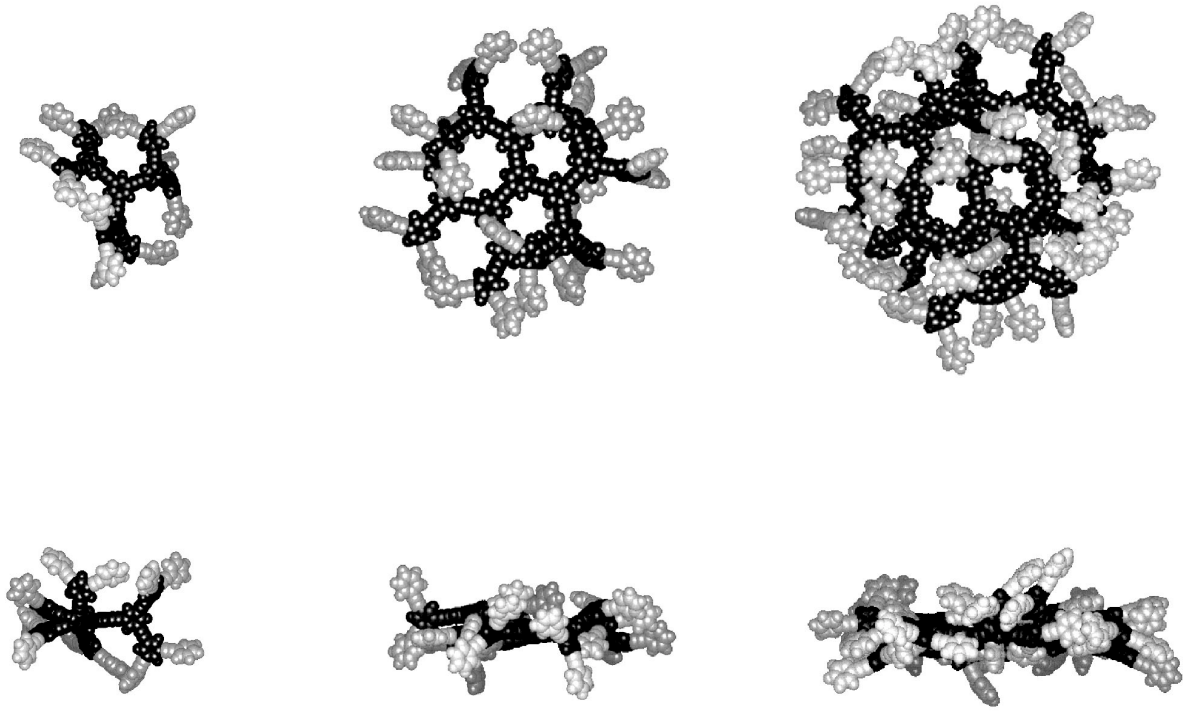

21-PHEN **45-PHEN** **93-PHEN**

Figure 4.3. CPK models of PHEN-derived dendrimers obtained at the midpoint of the 500 ps production dynamics run. Repeat units at the Term. are colored light gray. All others are colored black. Orthogonal views of each model are presented.

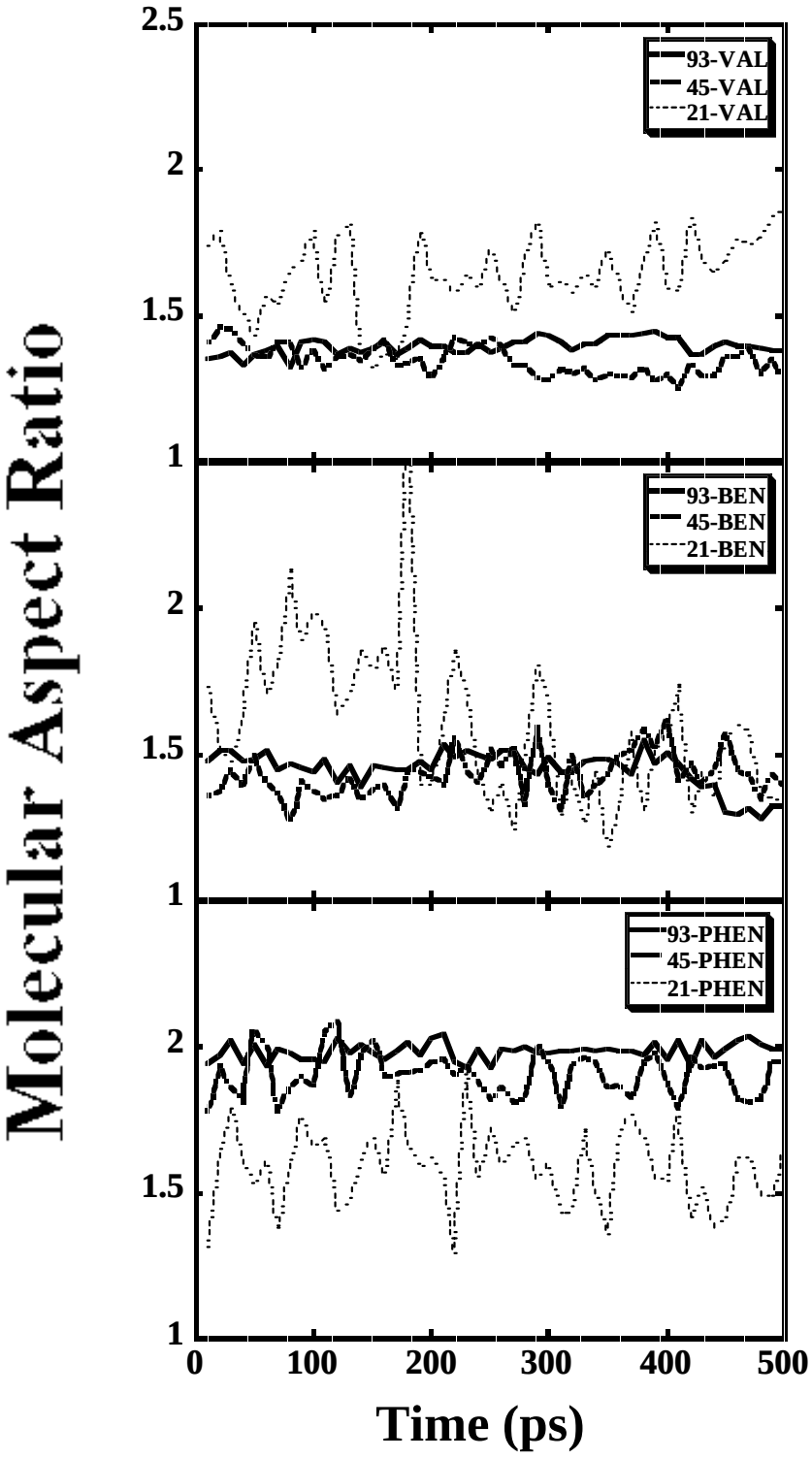

Figure 4.4. Aspect Ratios (Iz/Ix) of the models during the course of production dynamics.

In addition, the average aspect ratio of 21-BEN and 21-VAL over the course of the simulation was large compared to the larger BEN- and VAL-derived flexible dendrimers. The molecules 45-BEN, 45-VAL, 93-BEN, and 93-VAL exhibited a more or less constant aspect ratio of approximately 1.4 which is consistent with an eccentric spheroid, globular shape. This change in aspect ratio with increasing generation is consistent with experimental predictions of a change from a more extended to a more globular shape at approximately this degree of hyperbranching.[24-27] For the larger molecules, these observations indicate that flexible repeat unit dendrimers exhibit a compact, space-filling structure in both a static and dynamic sense. We have illustrated this effect more specifically via molecular dynamics simulations on BEN-derived dendrimers in the following section.

Unlike dendrimers derived from the flexible repeat units VAL and BEN, PHEN-derived dendrimers exhibited a very different shape. These dendrimers were much more disk-like as evidenced by the static CPK models (Figure 4.3) and the aspect ratios. (Figure 4.4) The molecule 21-PHEN exhibited a larger change in shape over the course of the simulation, again due to substantial motion of the peripheral groups. However, 45-PHEN and 93-PHEN had a more or less constant aspect ratio of 1.8-1.9, consistent with the disk-like conformations shown in Figure 4.3. Note that these conformations were obtained after high temperature annealing was performed on structures in which the dendrimers were initially placed into a *spherically symmetric* conformation around the central benzene core.

The energetic driving force for assuming this shape is attractive interatomic van der Waals forces that are optimized by concentrating phenylacetylene repeat units in a single plane. Energetically favorable π-conjugation among phenyl rings is also afforded by a planar conformation and is incorporated in the parameterization of the forcefields employed. Electron microscopy and powder diffraction data on crystalline phenylacetylene macrocycles and small dendrimers support a planar orientation of these molecules in the condensed state.[22] In addition, Monte Carlo conformational searching

on rigid polyphenylene dendrimer models indicated planar, low energy conformations resembling those obtained and presented here.[28]

4.2.3. Internal Organization

In addition to shape, the internal organization of the dendrimer units is important in developing molecular design rules. The spatial distribution of repeat units throughout each dendrimer was determined by computing number distribution functions (NDFs) for each of the molecules under study. These functions (Figure 4.5) represent the number of atoms at a given radial distance from the molecular core and were calculated for atom centers in each set of topologically identical repeat units (labeled as indicated in Figure 4.1). The values of these functions are those averaged over the course of the 500 ps production trajectory.

The NDFs for each of the three types of dendrimers illustrate that each topological generation was distributed throughout the geometric interior of each molecule. This trend was found for both the flexible and stiff dendrimers. In the case of flexible dendrimers, this distribution was attributed primarily to folding within the units of the molecule. This folding motif has been illustrated in most previously performed, coarse-grained computations of dendrimer conformation.[2-5,7,8] Dendron folding in the condensed and solution-state has been indicated experimentally. Solid-state REDOR NMR on flexible dendrons indicated close contact between the focal and peripheral groups within individual molecules.[9] Examination of longitudinal NMR relaxation times in paramagnetic core dendrimers also indicated close approach of all units within a dendrimer to the molecular core.[10]

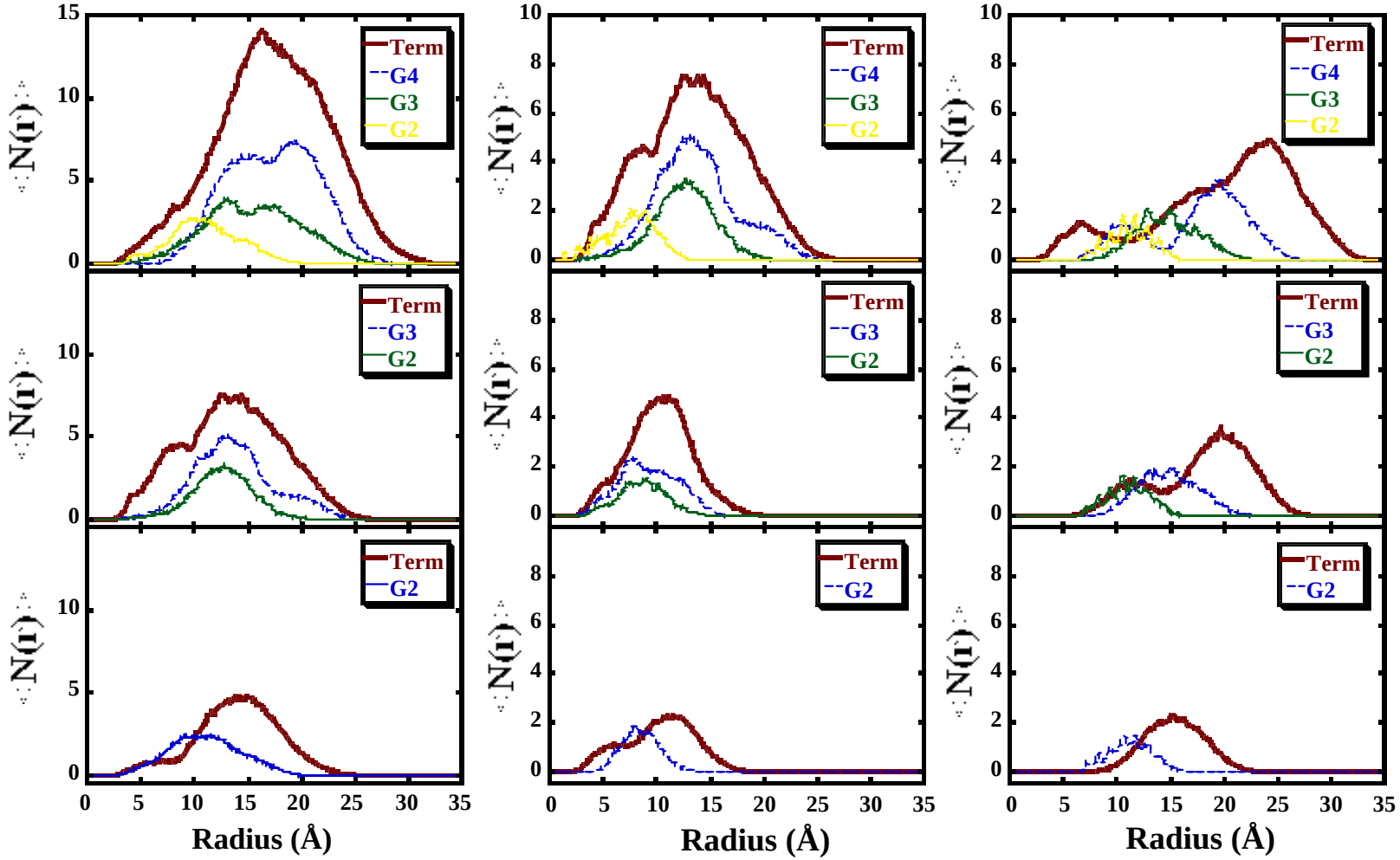

Figure 4.5. Number density distribution functions (<N(r)>) averaged over 500 ps of production dynamics for each dendrimer model. Follow labelling scheme adopted in Figure 4.7, pg. 114.

It was initially surprising to find NDFs for the stiff PHEN-derived dendrimers that were qualitatively so similar to those found in the flexible dendrimers. On first glance, these NDFs exhibited some periodicity, especially for 21-, 45-, and 93-PHEN. This observation was easily rationalized by the geometrical constraints imposed by the stiff repeat units. It is also notable that topological generations within each molecule (excluding 21-PHEN in which they are more radially localized) were radially disposed throughout each molecule. This disposition could not be due to folding within these molecules as none of the linkages should permit this. Rather, it was attributed to the angle of hyperbranching in the molecules. At each hyperbranch after the first one, the angle of branching splays one half of the groups in towards the center of the molecule.

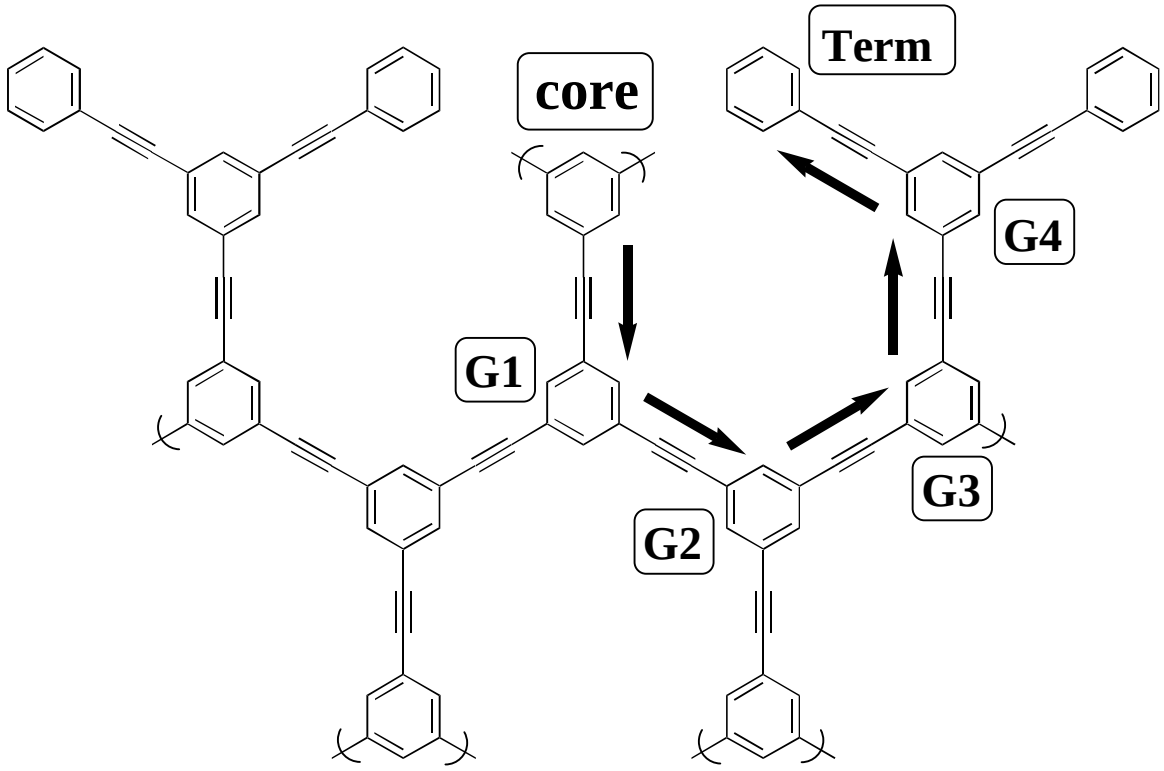

Figure 4.6. Schematic depicting the "inward folding" of stiff-chain dendrons via a rigid branching angle that forces repeat units in toward the molecular core.

This hyperbranching effect is illustrated schematically in Figure 4.6. This schematic predicts a high density of terminal repeat units should be found near the molecular core after four hyperbranches (i.e. for 93-PHEN). Indeed this was observed. The radial

density distribution functions (Figure 4.7) for the PHEN-derived dendrimers emphasizes this high local density in 93-PHEN compared to the smaller 45-PHEN and 21-PHEN. Simply, this molecule contains the requisite number of hyperbranches to bring the terminal groups around to the molecular core. Recently, a dramatic shift in fluorescence λ_{max} was observed in PHEN-derived dendrons with this number of hyperbranches when compared to smaller dendrons.[29] The conformational explanation depicted in Figure 4.6 might rationalize these experimental data.

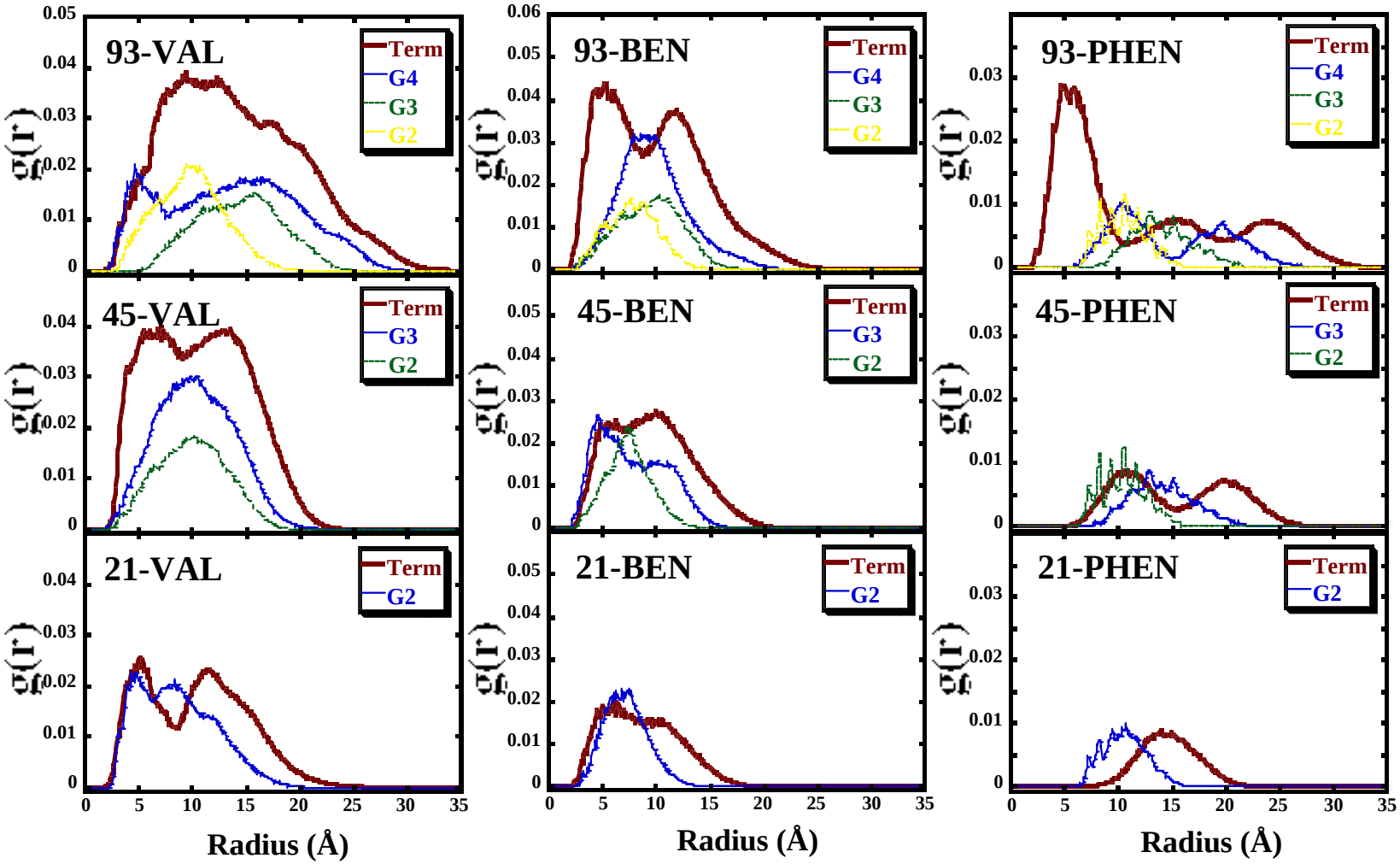

Figure 4.7. Radial density distribution functions, g(r), for PHEN-derived dendrimer models emphasize sudden density increase for 93-PHEN in the core region due to "inward folding."

4.2.4. Composition of the Geometric Periphery

Although all of the generations within each dendrimer are found to be radially distributed throughout the molecule, this conformation does not preclude finding a number of the topologically terminal groups at the geometric exterior of each molecule. The composition of the exterior surface of dendrimers is important for catalysis and molecular recognition applications. To indicate the composition of the exterior of the dendrimers, the CPK models in Figures 4.2 and 4.3 were color-coded to discriminate terminal (light gray) from non-terminal (black) repeat units. In the case of PHEN-derived dendrimers, their disk-like shape placed the majority of the repeat units at the accessible surface of the molecule. Thus their molecular surface was not found to be dominated by any particular topological generation.

In contrast, the surfaces of the VAL- and BEN-derived dendrimers were found to consist of a substantial number of terminal groups. The number of repeat units in each of the generations at the surface of each molecule was tabulated over the course of production dynamics (Figure 4.8). This analysis revealed that ca. 40 of the 48 terminal repeat units were found at the periphery in both 93-VAL and 93-BEN. This observation does not preclude finding a number of interior groups (G2-G4) at the surface of these molecules. Figure 4.8 illustrates that, indeed, a number of the interior groups were found at each molecular surface over the course of production dynamics. These observations indicate a structure in which most of the branch ends are concentrated at the surface of each dendrimer, yet a number are dispersed in the molecular interior.

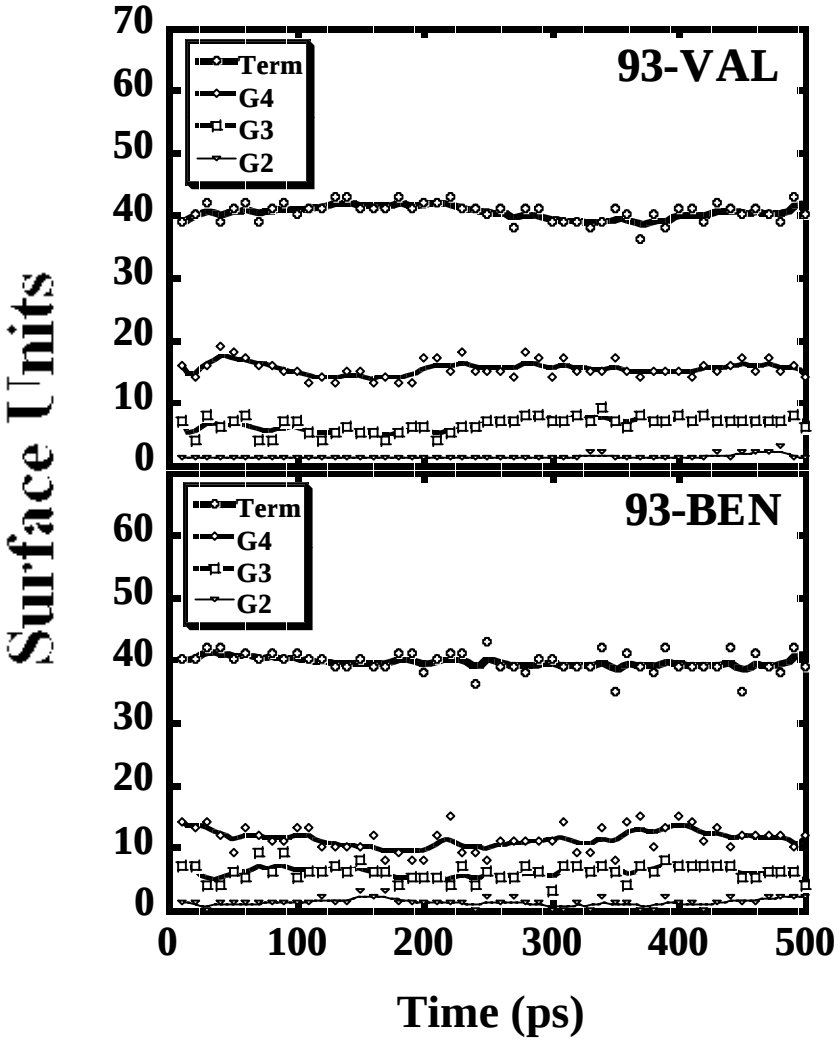

Figure 4.8. Surface accessible repeat units for 93-DENDRIMERS categorized by generation.

This distribution of repeat units was also reflected by their relative mobility. This mobility is illustrated for 93-VAL 93-BEN, and 93-PHEN by computing the average atomic mean square displacement correlation functions of each generation within each molecule over the course of production dynamics (Figure 4.9). The terminal groups in each molecule were, on average, substantially more mobile than the other generations on this time-scale. This behavior can be attributed to decreased steric congestion at the surface of 93-BEN and 93-VAL and to decreased steric congestion at the periphery of the disk in 93-PHEN. Conversely, the reduced average mobility of the other generations was attributed to their prevalence in the more densely packed interior.

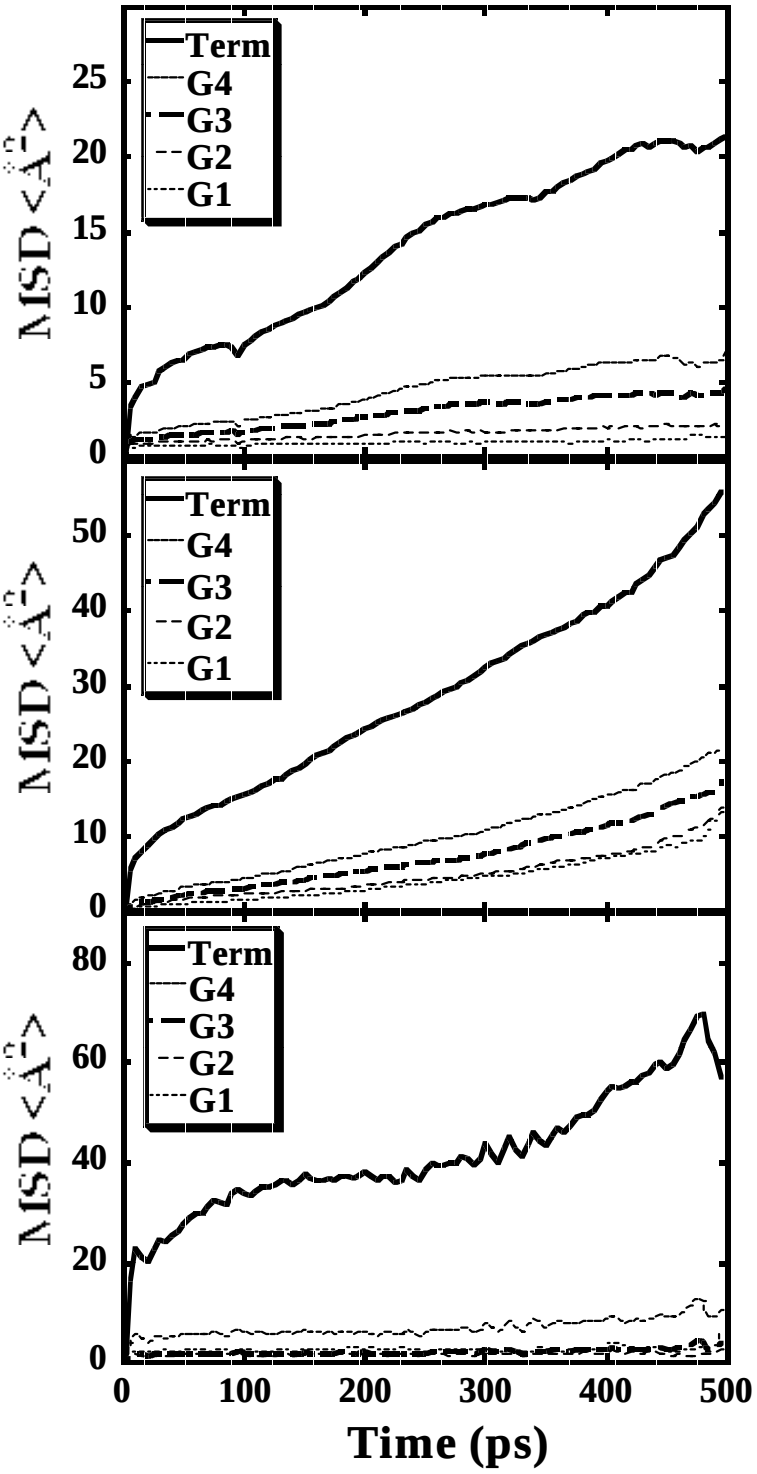

Figure 4.9. Averaged atomic Mean Square Displacement correlation functions (MSD<Å^2>) for repeat units in the 93-DENDRIMERS categorized by generation.

4.3. Conclusions

Atomistic molecular dynamics simulations illustrated differences in shape and internal organization of dendrimers as the flexibility of the dendrimer repeat unit was varied. In general, flexible repeat unit dendrimers possessed a somewhat eccentric but globular shape. Stiff-chain (phenylacetylene) repeat unit dendrimers were, in contrast, more disk-like in shape. For all dendrimers, the different generations within each molecule were found to be radially distributed throughout its interior. This appearance could be attributed to back-folding of some of the repeat units in the flexible case and to a branching angle effect in the stiff case. This distribution, however, did not preclude a molecular surface composed of a substantial portion of the topologically terminal groups generation.

4.4. Simulation Method

All dendrimer models were built from monomers using the Builder module in the Biosym/MSI software and displayed using the INSIGHTII molecular visualization program. In order to simulate models in atomistic detail, interactions were defined according to the DISCOVER PCFF (version 3.0) all-atom forcefield. This forcefield incorporates the following potential terms,

$$E_{Total} = \sum_{b}\left[K_2(b-b_0)^2\right] + \sum_{\theta}\left[K_\theta(\theta-\theta_0)^2\right] + \sum_{\phi}K_\phi\left[1+\cos(n*\phi-\phi_0)\right] +$$
$$\sum_{\chi}K_\chi(\chi-\chi_0)^2 + \sum_{i>j}\frac{q_i q_j}{r_{ij}} + \sum_{i>j}\varepsilon_{ij}\left[2*\left(\frac{r_{ij}^*}{r_{ij}}\right)^9 - 3*\left(\frac{r_{ij}^*}{r_{ij}}\right)^6\right]$$

(Equation 4.1)

The terms above are, respectively, the bond stretch term (*b*), the valence angle term (θ), the torsional potential (ϕ), the wilson-out-of-plane potential (χ), a Coulomb term, and a Lennard-Jones 9-6 potential describing the van der Waals interactions where

$$r_{ij} = \left[\frac{r_i^{\,6} + r_j^{\,6}}{2} \right]^{1/6} \qquad \text{(Equation 4.2)}$$

and

$$\varepsilon_{ij} = 2 * \sqrt{(\varepsilon_i * \varepsilon_j)} * r_i^{\,3} * \left[\frac{r_j^{\,3}}{r_i^{\,6} + r_j^{\,6}} \right] \qquad \text{(Equation 4.3)}$$

Forcefield parameters were taken from the PCFF version 3.0.0 forcefield. This forcefield is an extension of the Consistent Force Field, CFF91,[30,31] and is designed explicitly for polymer and organic materials applications.[32-34] This forcefield is parameterized for polymer simulations and has comparably soft attractive interatomic van der Waals potential terms. This results in a better consistency with solution-state properties and is more representative, in principle, of Θ-solvent conditions than simulations performed using the CVFF forcefield which give more compacted, congested structures when used in the same protocol. Electrostatic interactions were calculated with a non-distance dependent dielectric constant of 1. Functional groups that have been parameterized explicitly from quantum mechanics calculations and simulations include acetals, alcohols, alkenes, amines, carbonates, ethers, siloxanes, ureas, acids, alkanes, amides, aromatic groups, carbamates, urethanes, esters, silanes, and zeolites. No cross terms were taken into account.

As no X-ray or other structural data is available for dendrimers, the INSIGHTII Builder module was used to construct the dendrimer models shown in Figure 4.2 and 4.3. Each

of these dendrimer models were constructed in a completely extended conformation (e.g. dihedral angles set to 180°). After construction of a model, the structure was minimized to RMS < 0.01 kcal mol^{-1} $Å^{-1}$. In so doing, bonds were relaxed to their respective equilibrium bond distances. Next, the BEN- and VAL-derived structures were subjected to 100 ps of 600 K constant temperature dynamics to search for and obtain a low energy, equilibrium conformation for each structure.[35,36] The PHEN-derived structures were subjected to a preheating schedule before this procedure to avoid shocking. Subsequently, the temperature was stepped down in 50 K increments to 50 K. At each temperature step, atom velocities were readjusted and 5 ps of constant temperature molecular dynamics was performed. At 50 K, each structure was then minimized using steepest descents/conjugate gradients to RMS < 0.001 and equilibrated for 45 ps at 273 K. A 500 ps production trajectory at 273 K was then obtained. Computations were also performed using the CVFF forcefield. However, the use of the CVFF forcefield gave unrealistically compact dendrimer structures and occasionally failed to reach an equilibrium structure in the simulated annealing procedures described below. These behaviors were traced to the large attractive interatomic van der Waals forces inherent in this forcefield parameterization.

In all cases, constant temperature was achieved by direct velocity scaling as described below. During production dynamics, every structure had a constant average potential energy history consistent with an equilibrium structure. Similar results were obtained when other, arbitrary starting conformations were employed in the equilibration procedure and when the structures were subjected to multiple annealing cycles, suggesting that rigorous equilibration had been achieved.

During the annealing schedule, bonds were constrained to their equilibrium bond lengths using the RATTLE algorithm.[37] By applying constraints to bonds, the assumption that atom velocities and accelerations are constant becomes valid for large integration timesteps. In this way, a relatively long integration timestep of 2 fs was used without introducing instability or inaccuracy in the integration process. In addition, long range van der Waals interactions were neglected beyond a certain point, specified by the "cutoff

distance". Inaccuracy and instability may be introduced in this way as well due to discontinuities in energy derivatives. The DISCOVER 3.0.0 program incorporates a switching function to remedy the abrupt cutting off of non-bonded interactions. The switching function is mathematically incorporated into the forcefield and effectively smoothes the van der Waals potential from its natural potential energy to zero over a specified interval. This interval is specified by a parameter, swtdis, in the simulation. In addition, since atoms are continually changing their relative positions throughout the simulation, a protocol for updating atom neighbor lists is incorporated. This protocol involves the definition of a distance range outside the cutoff distance, called the buffer width, within which atom lists are updated before every integration step. The buffer width is explicitly specified in DISCOVER 3.0.0. In all calculations, non-bonded interactions were cut off at 9.5 Å (cutoff = 9.5 Å), the switching function was applied over the last 1.0 Å (swtdis = 1.0 Å), and the buffer width was 0.5 Å outside of the cut off distance.

In all simulations, initial velocities were generated so as to maintain a Maxwell-Boltzmann distribution at a specified "temperature". During dynamics kinetic energy is constantly changing to potential energy and vice versa. To maintain the correct temperature, atom velocities must be scaled periodically. In all simulations, "direct velocity scaling" was employed for this purpose. In contrast to other methods that, for example, adjust single atom velocities according to a Boltzmann distribution at every integration step, direct velocity scaling uniformly scales all atom velocities at one time according to the equation,

$$\left(\frac{v_{new}}{v_{old}}\right)^2 = \frac{T_{target}}{T_{system}} \qquad \text{(Equation 4.4)}$$

This scaling occurs only if the temperature of the system changes more than 10 K between two integration steps and is explicitly specified within the DISCOVER 3.0.0 program as the parameter, "temperature window."

Radial density distribution functions (g(r)) and Mean Square Displacement correlation functions (MSD<Å^2>)) were averaged over the 500 ps production trajectory. Radial density distribution functions denote the density of atom centers in a 0.01 Å thick radial shell centered at a radial distance from the dendrimer core. Number density distribution functions (<N(r)>) were generated by multiplying atom density*shell volume, and denote the number of atom centers at radial distace, r, from the dendrimer core. Aspect ratios are ratios of the principal moments of inertia, (Iz/Ix) where Ix < Iz. Surface accessible repeat units were analyzed by soaking (no equilibration) the models in a set of chloroform solvent molecules, and listing repeat units within 4.5 Å from any solvent molecule.

4.5. References and Notes

1)Lescanec, R. L.; Muthukumar, M., *Macromolecules,* **1990**, *23*, 2280-2288.

2)Murat, M.; Grest, G. S. *Macromolecules,* **1996**, *29*, 1278-1285.

3)Mansfield, M. L.; Klushin, L. I. *J. Phys. Chem.,* **1992**, *96*, 3994-3998.

4)Mansfield, M. L.; Klushin, L. I. *Macromolecules*, **1993**, *26*, 4262-4268.

5)Carl, W. *J. Chem., Soc.,, Faraday Trans.,* **1996**, *92*, 4151-4154.

6)Cai, C.; Chen, Z. Y. *Macromolecules,* **1997**, *30*, 5104-5117.

7)Chen, Z. Y.; Cui, S.-M. *Macromolecules,* **1996**, *29*, 7943-7952.

8)Boris, D.; Rubinstein, M. *Macromolecules,* **1996**, *29*, 7251-7260.

9)Wooley, K. L.; Klug, C. A.; Tasaki, K.; Schaefer, J. *J. Am. Chem., Soc.,* **1997**, *119*, 53-58.

10)Gorman, C. B.; Hager, M. W.; Parkhurst, B. L.; Smith, J. C. *Macromolecules,* **1998**, *31*, 815-822.

11)Naylor, A. M.; Goddard III, W. A.; Kiefer, G. E.; Tomalia, D. A. *J. Am. Chem., Soc.,* **1989**, *111*, 2339-2341.

12)Hawker, C. J.; Fréchet, J. M. J. *J. Am. Chem., Soc.,* **1990**, *112*, 7638-7647.

13)Hawker, C. J.; Fréchet, J. M. J. *J. Am. Chem., Soc.,* **1992**, *114*, 8405-8413.

14)Wooley, K. L.; Hawker, C. J.; Fréchet, J. M. J. *J. Am. Chem., Soc.,* **1991**, *113*, 4252-4261.

15)Xu, Z.; Moore, J. S. *Angew. Chem., Int. Ed. Engl.* **1993**, *32*, 246-248.

16)Bharathi, P.; Patel, U.; Kawaguchi, T.; Pesak, D. J.; Moore, J. S. *Macromolecules*, **1995**, *28*, 5955-5963.

17)Xu, Z.; Kahr, M.; Walker, K. L.; Wilkins, C. L.; Moore, J. S. *J. Am. Chem., Soc.,* **1994**, *116*, 4537-4550.

18)Kawaguchi, T.; Walker, K. L.; Wilkins, C. L.; Moore, J. S. *J. Am. Chem., Soc.,* **1995**, *117*, 2159-2165.

19)Pesak, D. J.; Moore, J. S. *Angew. Chem., Int. Ed. Engl.* **1997**, *36*, 1636-1639.

20)Höger, S.; Spickermann, J.; Morrison, D. L.; Dziezok, P.; Räder, H. J. *Macromolecules,* **1997**, *30*, 3110-3111.

21)Kaneko, T.; Horie, T.; Asano, M.; Aoki, T.; Oikawa, E. *Macromolecules,* **1997**, *30*, 3118-3121.

22)Buchko, C. J.; Wilson, P. M.; Xu, Z.; Zhang, J.; Moore, J. S.; Martin, D. C. *Polymer* **1995**, *36*, 1817-1825.

23)Morgenroth, F.; Reuther, E.; Müllen, K. *Angew. Chem., Int. Ed. Engl.* **1997**, *36*, 631-634.

24)Mourey, T. H.; Turner, S. R.; Rubinstein, M.; Fréchet, J. M. J.; Hawker, C. J.; Wooley, K. L. *Macromolecules*, **1992**, *25*, 2401-2406.

25)Hawker, C. J.; Wooley, K. L.; Fréchet, J. M. J. *J. Am. Chem., Soc.,* **1993**, *115*, 4375-4376.

26)Jiang, D.-L.; Aida, T. *Nature* **1997**, *388*, 454-456.

27)Tomoyose, Y.; Jiang, D.-L.; Jin, R.-H.; Aida, T.; Yamashita, T.; Horie, K.; Yashima, E.; Okamoto, Y. *Macromolecules*, **1996**, *29*, 5236-5238.

28)Morgenroth, F.; Kübel, C.; Müllen, K. *J. Mater. Chem.*, **1997**, *7*, 1207-1211.

29)Devadoss, C.; Bharathi, P.; Moore, J. S. *Angew. Chem., Int. Ed. Engl.* **1997**, *36*, 1633-1635.

30)Hwang, M. J.; Stockfisch, T. P.; Hagler, A. T. *J. Am. Chem., Soc.,* **1994**, *116*, 2515-2525.

31)Maple, J. A.; Hwang, M. J.; Stockfisch, T. P.; Dinur, U.; Waldman, M.; Ewig, C. S.; Hagler, A. T. *J. Comput. Chem.,* **1994**, *15*, 162-182.

32)Sun, H.; Mumby, S. J.; Maple, J. R.; Hagler, A. T. *J. Am. Chem., Soc.,* **1994**, *116*, 2978-2987.

33)Sun, H. *J. Comput. Chem.,* **1994**, *15*, 752-768.

34)Sun, H. *Macromolecules*, **1995**, *28*, 701-712.

35)Shamovsky, I. L.; Ross, G. M.; Riopelle, R. J.; Weaver, D. F. *J. Am. Chem., Soc.*, **1996**, *118*, 9743-9749.

36)Humphrey, W.; Xu, D.; Sheves, M.; Schulten, K. *J. Phys. Chem.,* **1995**, *99*, 14549-14560.

37)Anderson, H. C. *J. Comp. Phys.* **1983**, *52*, 24-34.

CHAPTER 5

SHAPE AND SEGMENTAL MOBILITY IN POLYETHER DENDRIMERS AS STUDIED BY MOLECULAR DYNAMICS SIMULATIONS

This work was communicated in preliminary form, Gorman, C. B.; Smith, J. C. *PMSE Preprints*, **1998**, 78, 226-227.

5.1. Introduction

Several questions have recently emerged about the conformation of dendrimers as the generation of the molecule increases. As one example, recent experiments to study the intrinsic viscosity of dendrimers,[1] solvatochromic shifts of chromophores focally attached to dendrons,[2] shifts in fluorescence spectra of dendrimers[3] and NMR relaxation data of dendrimers at various generations[4,5] have suggested a transition from an open, extended structure to a densely-packed, globular structure at about the third or fourth generation (alternatively, for molecular weights in the range of 3000-7000 amu).

Here, we present molecular dynamics simulations (MDS) that provide an atomistic picture of the average shape and relative mobility differences that develop with increased generation for polyether dendrimers employed experimentally in the majority of the studies above. Critical in obtaining a simulation consistent with solution-state physical properties was the production of a reasonable, equilibrated starting geometry for each of the models upon which to perform dynamics. This is an important component of MDS on macromolecules and has not always been applied in past atomistic simulations.[6,7] Most computational and numerical simulations of dendrimers have employed coarse-grain models that incorporate rigorous equilibration techniques but do not include chemical detail.[8-15] A procedure for realistic, atomistic simulations can provide a way to investigate structure-property relationships computationally with potential use in molecular design strategies in applications employing dendrimers.

5.2. Results and Discussion

5.2.1. Shape Evolution

Atomistic molecular dynamics simulations were performed on each of a series of 3-arm polyether dendrimers (Figure 5.1) of generations 1 through 5 composed of dibenzyloxy repeat units.[16] These simulations were performed using a high temperature simulated annealing protocol described in the atomistic model and simulation methods section

above. These structures contain the same repeat unit as those studied in the experiments referred to above.

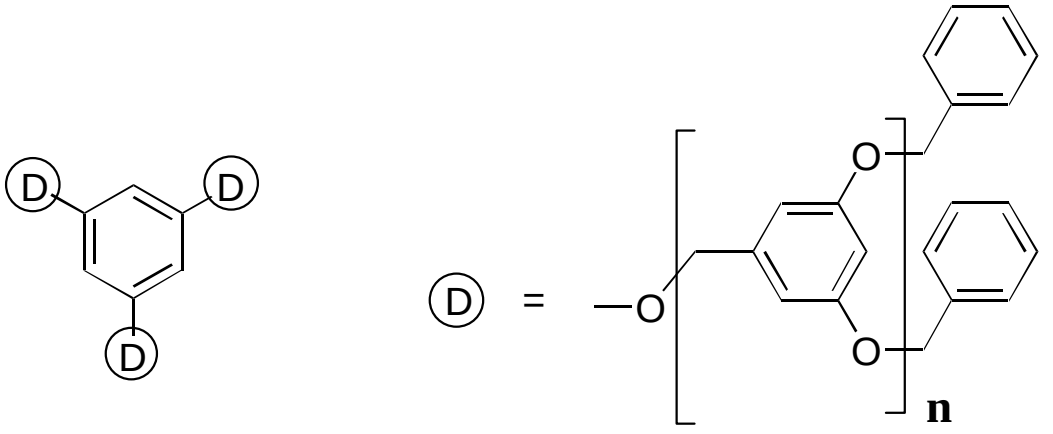

n = 1-5 (generation 1-5)

Figure 5.1. The structures employed in this study.

The results of these simulations showed a change in the average shape of the dendrimer models with increasing generation (Figure 5.2). As generation increased, the average eccentricity[25] of each of the structures became closer to spheroid (eccentricity = 1). Early generations (1-2) were comparably more eccentric displaying, on average, more open, extended conformations. At generation 3 (45 benzyl units, molecular weight of 4,848), the average molecular shape was found to be more spherical. The average shape of the structures then remained constant up to generation 5.

The molecular weight range corresponding to this shape change correlated well with experimentally determined changes in behavior of several dibenzyloxy dendrons and dendrimers of similar size and molecular weight. The four sets of experimental data that might be explained by this shape change with increasing generation were a reduction in T_1 values of nuclei on dendrimers with azobenzene[5] and porphyrin cores,[4] a nonlinear molecular weight dependence on intrinsic viscosity in dendrons and dendrimers,[1] and a

nonlinear change in absorption maximum of a solvatochromic probe attached at the focal point of dibenzyloxy dendrons.[2] All of these effects occurred at generation 3 or 4. This variance is undoubtedly due to differences in the topology and molecular weight between these structures. Thus, the molecular weight of the structures studied here is given in Figure 5.2 as this parameter may be best in correlating all of the data.

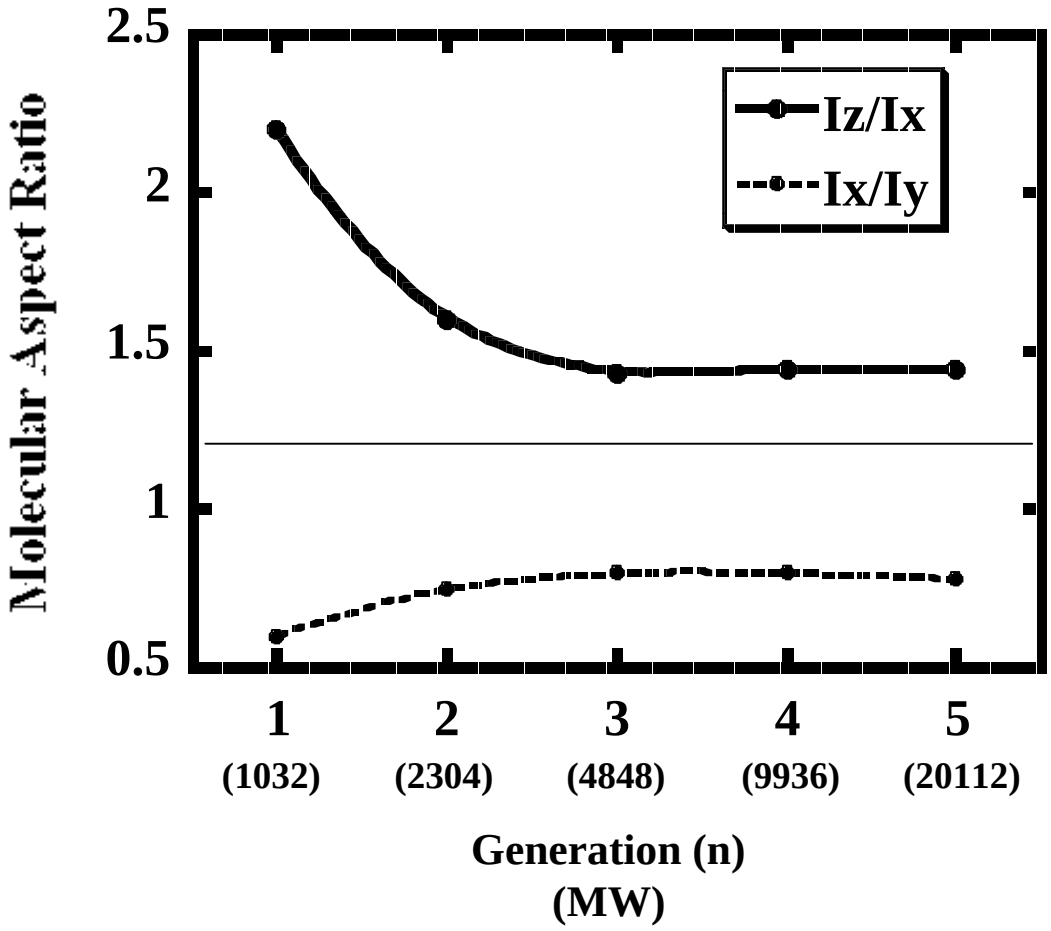

Figure 5.2. Average eccentricity (defined as ratios of principal moments of inertia) as a function of generation for each structure. Lines are drawn through data points solely as a guide to the eye.

5.2.2. Segmental Mobility

Calculated RMS fluctuations (Figure 5.3) also indicates a change in the behavior of the dendrimers as a function of generation. The magnitude of the bars in Figure 5.3 indicates quantitatively the average mobility (segmental motion) of each set of repeat units

comprising each generation within a given molecule. These designations are termed Gn where n counts the number of topological layers of repeat units starting at the molecular core. Specifically, the relative mobility of the terminal groups decreased notably from generation 2 to generation 3 as did the relative mobility of interior groups.

Decreased mobility with increasing molecular weight is attributed to increased steric congestion for interior and terminal nuclei. This decrease in relative motion is consistent with a transition to a more congested structure at this molecular size. The data in both Figures 5.2 and 5.3 illustrates structural differences among the molecules that might explain the experimental observations mentioned above. These functions, however, illustrate additional steric congestion with increasing generation past generation 3. At generation 5, the amount of both internal and peripheral motion was found to decrease compared to the generation 3 and generation 4 models. Notably, the relative shape of the generation 5 model, however, was similar to that of generation 3 and generation 4 (Figure 3.2). This effect might be illustrated experimentally. However, few experiments with sufficiently large dendrimers of this type have been reported.

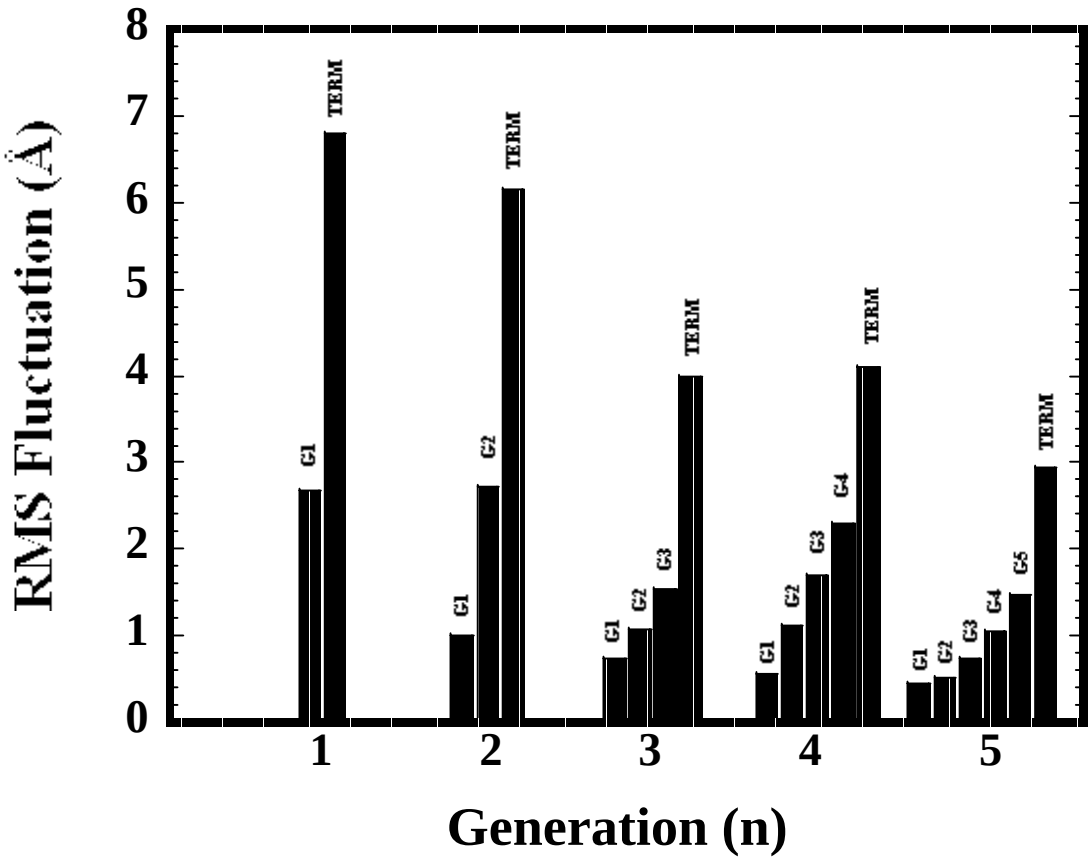

Figure 5.3. Average RMS fluctuations[26] over the course of the MDS for each group of atoms listed. Designations "Gn" refer to atoms in each group of repeat units at the n-th topological layer from the molecular core in each structure. The designation "Term" refers to the terminal benzyl groups.

5.3. Conclusions

These results show that atomistic molecular dynamics simulations may be used effectively to model dendrimer conformation and to provide a molecular picture consistent with experimental results. Further efforts to elucidate specific molecular structure-property relationships such as the relationship between the repeat unit structure and overall conformation of the dendrimer appear worthwhile given these results. Such relationships are under exploration in our group.

5.4. Simulation Method

All dendrimer models were built from monomers using the Builder module in the Biosym/MSI software and displayed using the INSIGHTII molecular visualization program. In order to simulate models in atomistic detail, interactions were defined according to the DISCOVER PCFF (version 3.0) all-atom forcefield as described in Section 4.4.

As no X-ray or other structural data is available for dendrimers, the INSIGHTII Builder module was used to construct the polyether dendrimer models of generation 1 through generation 5 (Figure 5.1). Each of these five dendrimer models were constructed in a completely extended conformation. After construction of a model, the structure was minimized to RMS < 0.01 kcal mol^{-1} $Å^{-1}$. In so doing, bonds were relaxed to their respective equilibrium bond distances. Next, each model was subjected to 100 ps of high temperature dynamics at 600 K to search for and obtain a low energy, equilibrium conformation for each structure.[22,23]

Each of these five structures were subsequently subjected to a cooling schedule from 600 K to 50 K in steps of 50 K per 5 ps. Each of these five equilibrium structures were then minimized to a maximum derivative of < 0.001 kcal mol^{-1} $Å^{-1}$. Dynamics on each structure were then performed at 273 K for a 45 ps equilibration period. Subsequently, 500 ps of production dynamics at this temperature were run on each structure to obtain the data presented here. In all cases, constant temperature was achieved by direct velocity scaling as described below. During production dynamics, every structure had a constant average potential energy history consistent with an equilibrium structure. The criterion for equilibration is convergence to similar potential energies starting from arbitrary initial conditions (i.e. different starting structures). The potential energy vs time plots for two distinct 500 ps production dynamic runs originating from arbitrary start structures is shown in Figure 5.4. Note convergence to similar potential energies indicates that the procedure employed is achieving “true equilibration.” Similar results were obtained for all models employed in this study.

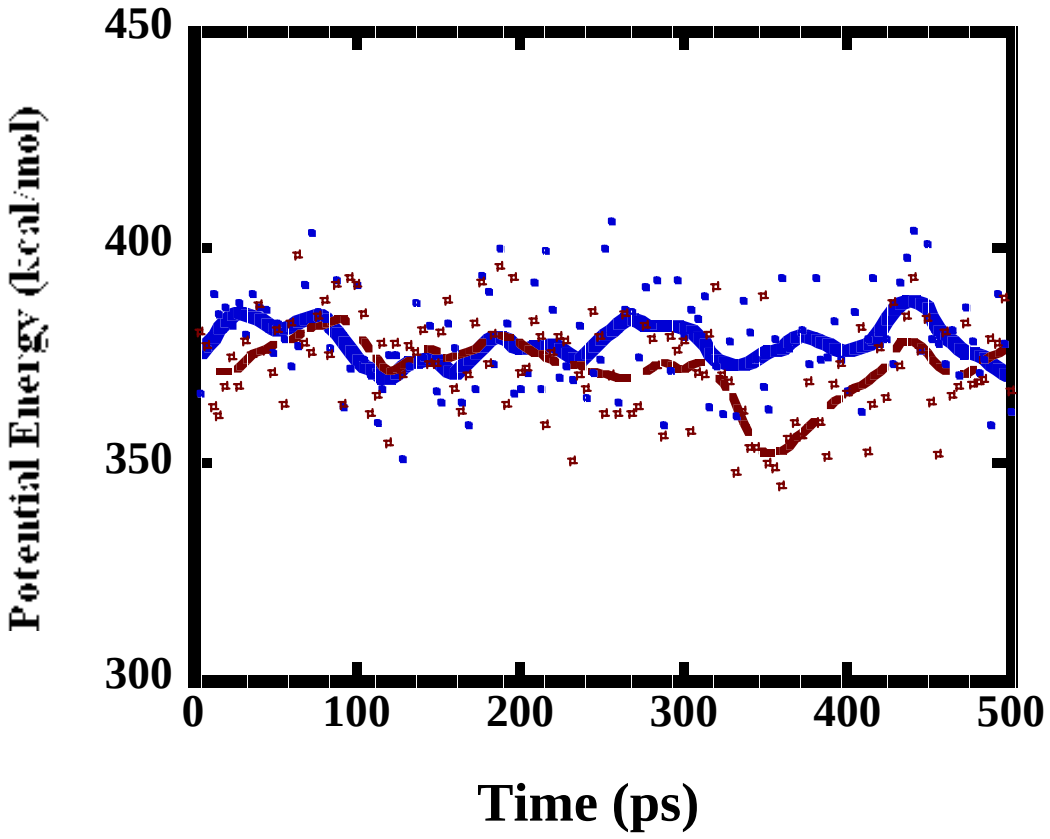

Figure 5.4. Potential energy vs time plots during production dynamics for two different starting structures of the BEN4 model. The trajectory indicates convergence to similar potentiel energies indicative of adequate equilibration. Similar plots were obtained for all models employed.

During the annealing schedule, bonds were constrained to their equilibrium bond lengths using the RATTLE algorithm.[24] By applying constraints to bonds, the assumption that atom velocities and accelerations are constant becomes valid for large integration timesteps. In this way, a relatively long integration timestep of 2 fs was used without introducing instability or inaccuracy in the integration process. In addition, long range van der Waals interactions were neglected beyond a certain point, specified by the "cutoff distance". Inaccuracy and instability may be introduced in this way as well due to discontinuities in energy derivatives. The DISCOVER 3.0.0 program incorporates a switching function to remedy the abrupt cutting off of non-bonded interactions. The switching function is mathematically incorporated into the forcefield and effectively smoothes the van der Waals potential from its natural potential energy to zero over a

specified interval. This interval is specified by a parameter, swtdis, in the simulation,. In addition, since atoms are continually changing their relative positions throughout the simulation, a protocol for updating atom neighbor lists is incorporated. This protocol involves the definition of a distance range outside the cutoff distance, called the buffer width, within which atom lists are updated before every integration step. The buffer width is explicitly specified in DISCOVER 3.0.0. In all calculations, non-bonded interactions were cut off at 9.5 Å (cutoff = 9.5 Å), the switching function was applied over the last 1.0 Å (swtdis = 1.0 Å), and the buffer width was 0.5 Å outside of the cut off distance.

In all simulations, initial velocities were generated so as to maintain a Maxwell-Boltzmann distribution at a specified "temperature". During dynamics kinetic energy is constantly changing to potential energy and vice versa. To maintain the correct temperature, atom velocities must be scaled periodically. In all simulations, "direct velocity scaling" was employed for this purpose. In contrast to other methods that, for example, adjust single atom velocities according to a Boltzmann distribution at every integration step, direct velocity scaling uniformly scales all atom velocities at one time according to the equation,

$$\left(\frac{v_{new}}{v_{old}} \right)^2 = \frac{T_{target}}{T_{system}} \qquad \text{(Equation 5.4)}$$

This scaling occurs only if the temperature of the system changes more than 10 K between two integration steps and is explicitly specified within the DISCOVER 3.0.0 program as the parameter, "temperature window."

5.5. References and Notes

1)Mourey, T. H.; Turner, S. R.; Rubinstein, M.; Fréchet, J. M. J.; Hawker, C. J.; Wooley, K. L. *Macromolecules* **1992**, *25*, 2401-2406.

2)Hawker, C. J.; Wooley, K. L.; Fréchet, J. M. J. *J. Am. Chem. Soc.* **1993**, *115*, 4375-4376.

3)Devadoss, C.; Bharathi, P.; Moore, J. S. *Angew. Chem. Int. Ed. Engl.* **1997**, *36*, 1633-1635.

4)Tomoyose, Y.; Jiang, D.-L.; Jin, R.-H.; Aida, T.; Yamashita, T.; Horie, K.; Yashima, E.; Okamoto, Y. *Macromolecules* **1996**, *29*, 5236-5238.

5)Jiang, D.-L.; Aida, T. *Nature* **1997**, *388*, 454-456.

6)Naylor, A. M.; Goddard III, W. A.; Kiefer, G. E.; Tomalia, D. A. *J. Am. Chem. Soc.* **1989**, *111*, 2339-2341.

7)Camps, X.; Schönberger, H.; Hirsch, A. *Chem. Eur. J.* **1997**, *3*, 561-567.

8)Lescanec, R. L.; Muthukumar, M. *Macromolecules* **1990**, *23*, 2280-2288.

9)Murat, M.; Grest, G. S. *Macromolecules* **1996**, *29*, 1278-1285.

10)Mansfield, M. L.; Klushin, L. I. *J. Phys. Chem.* **1992**, *96*, 3994-3998.

11)Mansfield, M. L.; Klushin, L. I. *Macromolecules* **1993**, *26*, 4262-4268.

12)Boris, D.; Rubinstein, M. *Macromolecules* **1996**, *29*, 7251-7260.

13)Cai, C.; Chen, Z. Y. *Macromolecules* **1997**, *30*, 5104-5117.

14)Chen, Z. Y.; Cui, S.-M. *Macromolecules* **1996**, *29*, 7943-7952.

15)Carl, W. *J. Chem. Soc., Faraday Trans.* **1996**, *92*, 4151-4154.

16)Hawker, C. J.; Fréchet, J. M. J. *J. Am. Chem. Soc.* **1990**, *112*, 7638-7647.

17)Maple, J. A.; Hwang, M. J.; Stockfisch, T. P.; Dinur, U.; Waldman, M.; Ewig, C. S.; Hagler, A. T. *J. Comput. Chem.* **1994**, *15*, 162-182.

18)Hwang, M. J.; Stockfisch, T. P.; Hagler, A. T. *J. Am. Chem. Soc.* **1994**, *116*, 2515-2525.

19)Sun, H.; Mumby, S. J.; Maple, J. R.; Hagler, A. T. *J. Am. Chem. Soc.* **1994**, *116*, 2978-2987.

20)Sun, H. *Macromolecules* **1995**, *28*, 701-712.

21)Sun, H. *J. Comput. Chem.* **1994**, *15*, 752-768.

22)Humphrey, W.; Xu, D.; Sheves, M.; Schulten, K. *J. Phys. Chem.* **1995**, *99*, 14549-14560.

23)Shamovsky, I. L.; Ross, G. M.; Riopelle, R. J.; Weaver, D. F. *J. Am. Chem. Soc.* **1996**, *118*, 9743-9749.

24)Anderson, H. C. *J. Comp. Phys.* **1983**, *52*, 24-34.

25) Eccentricity is defined for each molecule considered by taking the ratio of the moments of inertia given in Figure 2 for each structure in the production trajectory. The average of these is reported.

26) RMS fluctuation was calculated for each topological group of atoms (i.e. TERM, G1, G2, etc.) in each of the dendrimer models. In any two given frames captured during the course of the simulation, non-hydrogen atoms in each of the specified topological groups were superimposed using an iterative nonlinear least-squares algorithm (Discover 2.9.7/95.0/3.0.0 manual, p. 4-19). Subsequently, the equation used to calculate the RMS fluctuation between frames j and k for a topological group was:

$$\mathrm{RMS} = \left[\sum_{i=1}^{N} \frac{\left(x_{ij} - x_{ik}\right)^2 + \left(y_{ij} - y_{ik}\right)^2 + \left(z_{ij} - z_{ik}\right)^2}{N} \right]^{1/2}$$

where N represents the number of non-hydrogen atoms in the topological group. The values graphed in Figure 3 are the average of the calculated RMS fluctuations over each pair of frames captured during the course of the production molecular dynamics trajectory (here 125 frames captured during the course of a 500 ps production dynamics trajectory). See the INSIGHTII 3.0.0 User's Guide, p. 6-9. This type of data has been used to illustrate relative segmental motion in proteins, see: Elber, R.; Karplus, M. *Science*, **1987**, *235*, 318-321.

APPENDIX I

DEVELOPMENT OF COMPUTATIONAL SEARCHING PROTOCOL

A.1. Impetus

The incorporation of units with contrasting chemical properties into a molecular architecture inevitably cause changes in its three-dimensional shape and internal organization. A valid comparison of two architectures, such as those considered in this study, proffers from models of the molecular conformation. Molecular models, however, are only models. Their purpose in the present study, and arguably in any study, are to offer a hypothetical physical picture for rationalizing experimental trends. The level of rigor taken in generating a model depends on the theoretical technique employed. In Section 2.7, the development of a search routine employing classical mechanics and molecular dynamics simulations is outlined. The significance of the resultant three-dimensional structures is at best slightly more reliable than ball-and-stick models built using a sophomore organic chemistry modeling set. Nevertheless, the usefulness of these simulations for interpreting data and conceptualizing a molecular-scale physical picture turns out to be indispensable.

Conformational searching is a non-deterministic method (i.e. it approximates solutions to mathematical problems) for analyzing molecular conformation. This technique suffers from uncertainties resulting directly from the "multiple minimum problem." That is, there is no sure way to guarantee that a minimum energy conformation found during a search is *the* lowest energy minimum on the potential energy surface. To ensure that the structures generated during the search were non-arbitrary, we designed a novel searching method that incorporated not one but two searches- 1) a high temperature coarse-grain search designed to scan large portions of the potential energy surface and 2) a low temperature search designed to generate a localized search around the "best" structure found in 1). Issues and concerns regarding the development and interpretation of these conformational searches will be discussed in Sections 2.7.2 – 2.7.7.

A.2. Coarse-grained search (High Temperature Search)

A.2.1. General Procedure

A high temperature (1000K or greater) search routine was designed for quickly scanning the potential energy surface and locating a low energy starting point for subsequent simulations done in lower temperature regimes (as described in Sections 2.7.3 and 2.7.4). Simulations performed in high temperature regimes allow the system to traverse high potential energy barriers and visit several regions of the potential energy surface in a short amount of simulation time. There are disadvantages to using this strategy that should be noted. Highly kinetically energized structures generated along the dynamics trajectory require a cooling schedule prior to their minimization. The "simulated annealing" process should be slow enough (ideally infinitely slow) to relax structures into nearby wells. The cooling process is critical to obtaining useful data (i.e. structures that are effectively relaxed) and computationally the most costly portion of the search routine described here.

A stepwise description of the high temperature conformational search routine follows. Structures were generated using the BUILDER module within the MSI (BIOSYM) InsightII visualization program. The initial construction of each model was done using the BUILDER module. The same procedure for building molecular models was employed in every case. Specifically, the core was substituted with the appropriate repeat units to produce the generation 1 dendrimer. This structure was minimized. Then, repeat units were attached to this geometry-optimized structure to produce the generation 2 dendrimer. This structure was geometry optimized, and so on. The completed model was subjected to 25 cycles of high temperature (1000K or higher) dynamics as follows. Each model was subjected to 4 ps of high temperature dynamics at temperatures chosen as described in sections to follow. Four structures from this trajectory (0.5 ps, 1.0 ps, 2.0 ps, and 4 ps) were cooled to 300K at a rate of 100 K/ps starting at 1000 K, minimized and saved. The fourth minimized structure was used as the start point in the next cycle. Completion of twenty-five cycles gave 101 minimized conformers (100 generated

conformers plus the starting conformer). The lowest energy conformer in this set was carried on to the next step of dynamics.

A successful search sampled a large range of molecular geometries and gave several adequately relaxed structures (i.e. structures that, after minimization, had potential energies below or comparable to that of the initial starting structure.) These criterions were met except in the case of **G3Rigid** and **G4Rigid**. In these two cases, it was not possible to find a practical search temperature.

A.2.2. Evaluation of High Temperature Search

During the high temperature (1000K) initial conformational searches, these data were evaluated as to whether conformational space was adequately searched and whether lower energy minima than the initial starting structure could be found. Figure A.1 is a representation of the 101 minimized structures (100 from dynamics plus the starting structure) generated during the high temperature searches (e.g. 1000K) for the flexible dendrimer models. Each panel represents the data for one search. The histogram at the bottom of each panel bins the structures according to the geometric parameter R_{core}/R_g (relative core offset). The plot on top maps out the relative potential energy versus geometric parameter R_{core}/R_g. Relative potential energy was fixed by setting the energy of the lowest energy structure found during the search to zero. Thus, these panels depict both the relative potential energy of the minimized structures and the range of geometries sampled during the search. The data indicate that a reasonable range of conformations were sampled. The lowest energy structure found during this search was carried on as the starting point for quenched molecular dynamics. (Section A.3) It was initially tempting to choose a conformation representative of the most common R_{core}/R_g value found during this search (i.e. one from the set represented by the biggest bar in the histograms shown). However, we have observed that extremely high temperature searches will unavoidably generate a set of structures biased toward high energy conformers, so the choice was not made in this way.

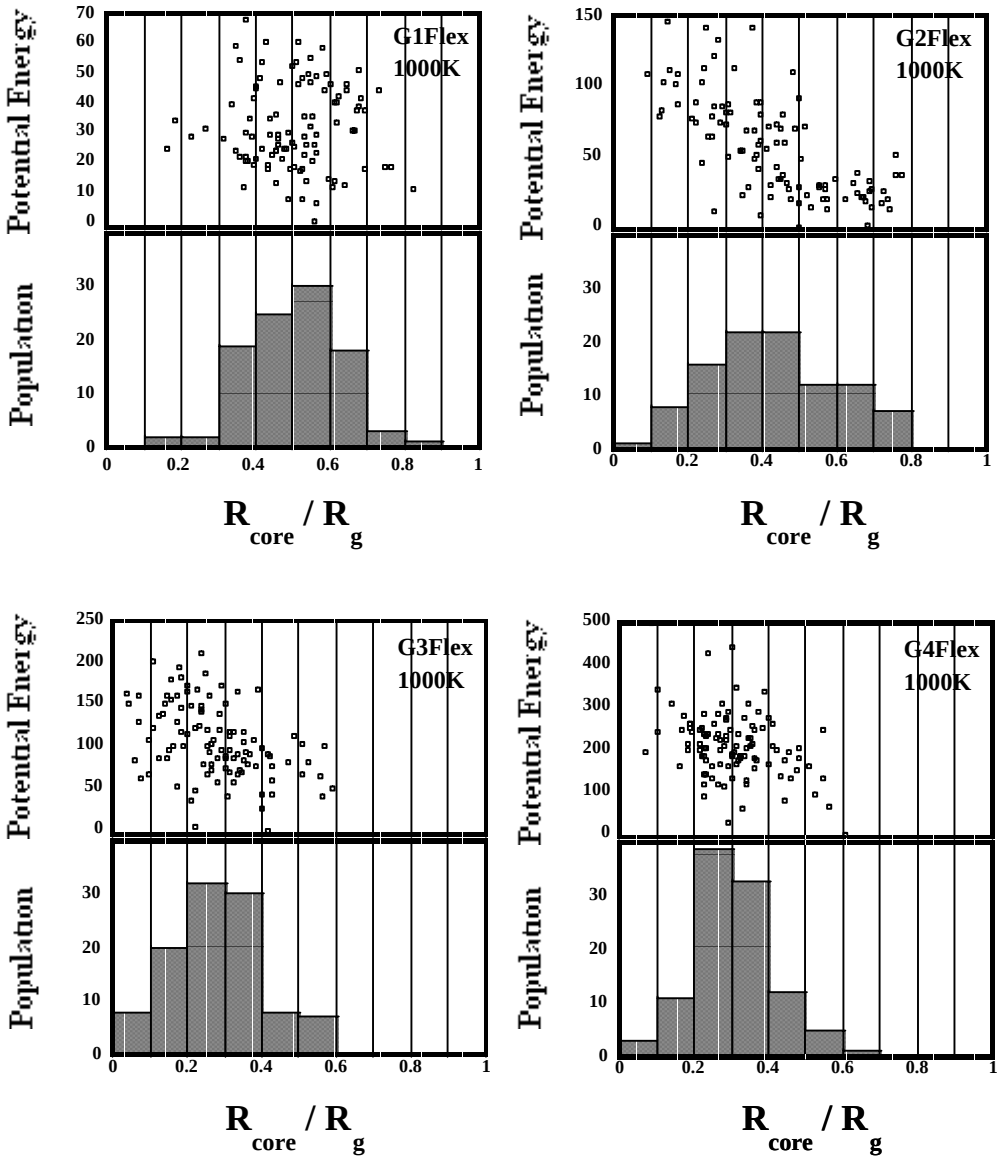

Figure A.1. Results of high temperature searches for flexible dendrimer series. Potential energy is relative to the lowest energy strucutre and in units of kcal/mol.

Figure A.2 is a representation identical to that of Figure A.1 for **G1Rigid**. It was deemed that, again, an adequate range of conformations was sampled for this model. However, one can already discern that fewer conformations were sampled for a given search temperature in this small, rigid dendrimer model than were found in the flexible dendrimer models.

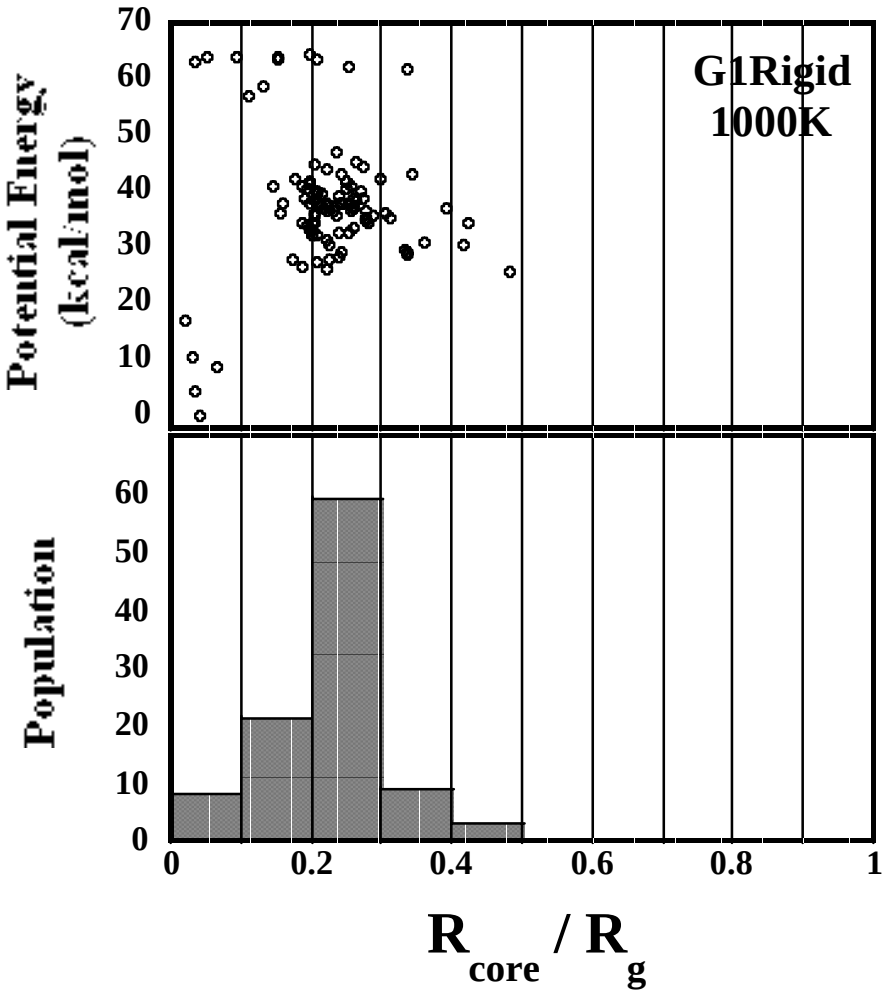

Figure A.2. High temperature search results for G1Rigid. Potential energy is relative to the lowest energy structure.

This problem is exacerbated with increasing molecular size for the rigid dendrimers as is illustrated in Figure A.3 for **G2Rigid.** After 44 conformers were obtained, it became clear that a 1000K search failed to find a range of conformers with much difference in geometry. Thus, the conformational search for **G2Rigid** was rerun at a higher temperature (1450K). The second panel in Figure A.3 shows the first 44 conformers obtained in this 1450K search and illustrates that a much broader range of conformers was found. The third panel of Figure A.3 shows all 101 conformers obtained in this 1450K search. The lowest energy conformer in this set was carried on to the next phase of molecular dynamics.

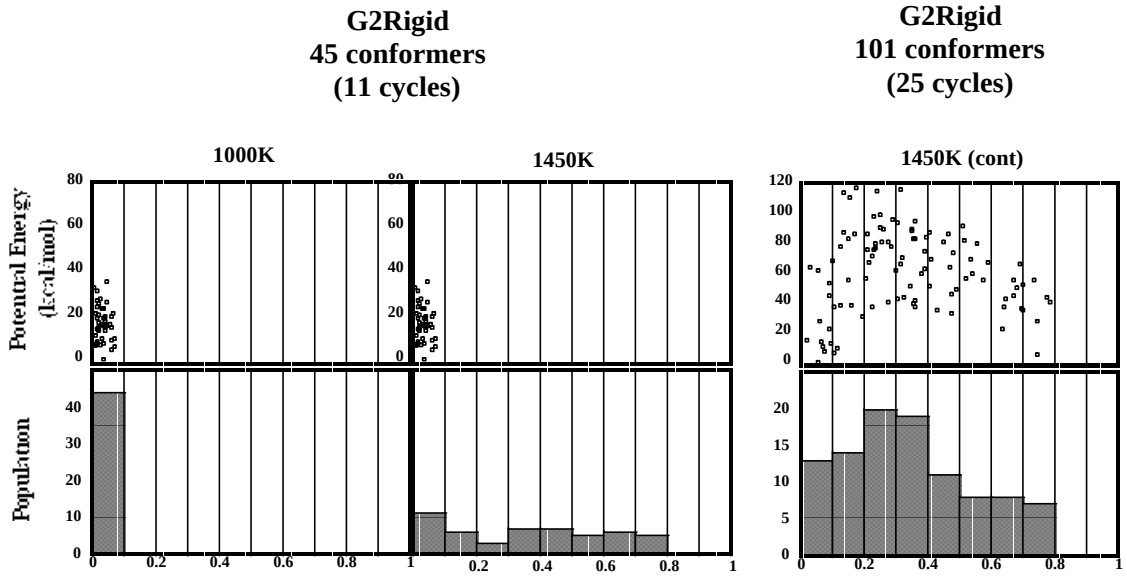

Figure A.3. High temperature search results for G2Rigid at two temperatures, 1000K and 1450K. Potential energy is relative to the lowest energy structure.

Figure A.4 shows that, in the case of **G3Rigid**, poor sampling was obtained at 1450K but adequate sampling was obtained at 1850K. Here, only 61 conformers were generated because, as will be discussed further below, the energy criterion was not met, and ultimately, this set of structures was not useful. One gets a first indication of this by noting that all the structures shown in the 1850K search (save one, the starting structure) are substantially higher in relative energy than the starting structure. Figure A.4 shows 69 conformers obtained during a 1450K search on **G4Rigid** and again suggests poor sampling. Higher temperature searches were not conducted on **G4Rigid** for reasons discussed further below.

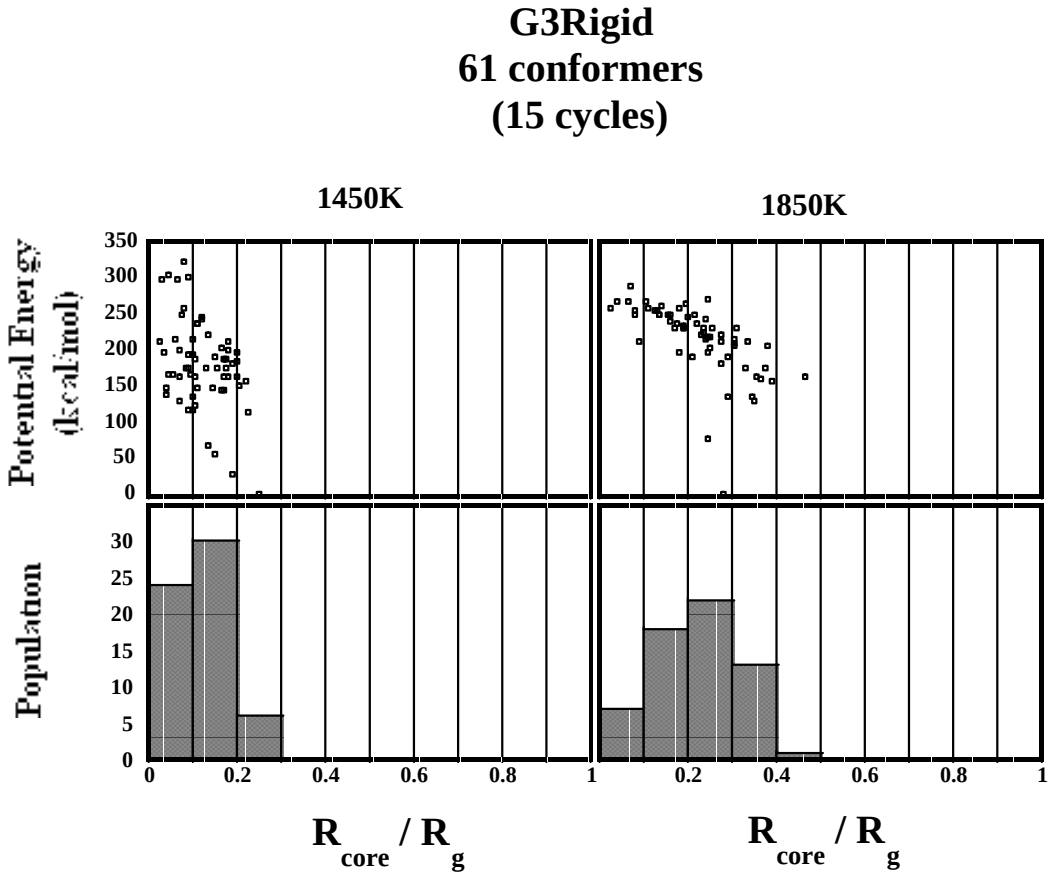

Figure A.4. High temperature search results for G3Rigid at two temperatures, 1450K and 1850K. Potential energy is relative to the lowest energy strucutre.

Figure A.6 graphs the energies of the minimized conformers generated during the course of each high temperature search. Thus, these data illustrate the evolution of the *minimized* potential energy (i.e. the "bottom" of the potential energy surface) with simulation time. The plots represent 251 minimized structures for each search (except the **G3Rigid** and **G4Rigid** searches which were stopped early as indicated previously). Lines are drawn through the data merely as a guide to the eye. The data shows that for the flexible molecules and for **G1-G2Rigid**, the search found structures with a lower energy than the starting structure. In contrast, the **G3Rigid** and **G4Rigid** searches did not exhibit this behavior. In fact, no minimized structure was found within 30 kcal/mol of the initial start structure after 15 cycles for **G3Rigid** and 17 cycles for **G4Rigid**. This behavior is due to the bias of the high temperature search towards higher energy minima.

The solution is to apply a slower rate of cooling during the annealing process. However, this option was impractical from the standpoint of computational time.

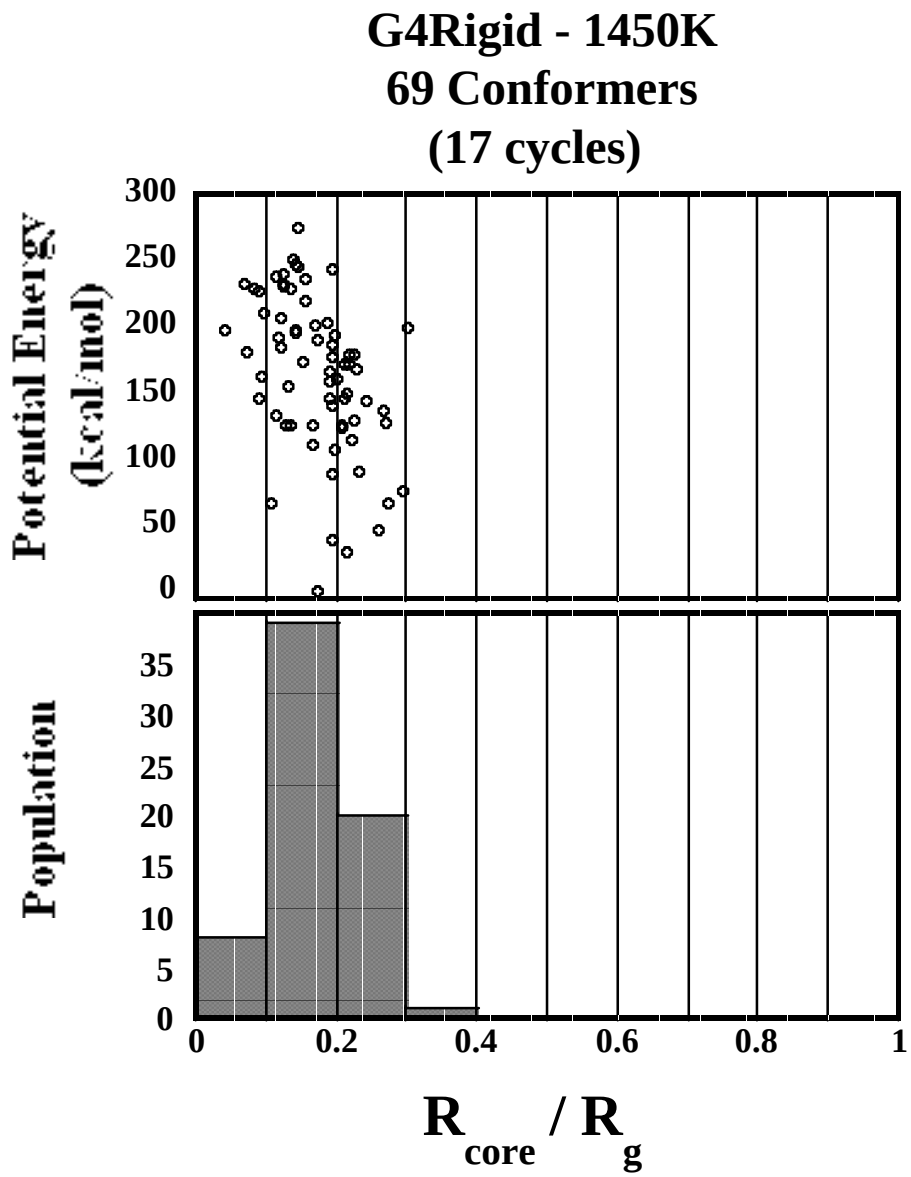

Figure A.5 . High temperature search results for G4Rigid at 1450K. Potential energy is relative to the lowest energy structure.

Thus, by increasing the temperature of the search for the purpose of sampling a larger range of structures, in the case of **G3Rigid** and **G4Rigid,** the search was biased towards

high energy (and thus useless) minima. As stated before, a much slower cooling schedule would be required to obtain lower energy minima in these high temperature searches, but this was not feasible as it would have been too computationally intensive. Thus, the starting structures constructed in the BUILDER as described in Section 2.7.1 were used as start points in subsequent searches for **G3Rigid** and **G4Rigid**.

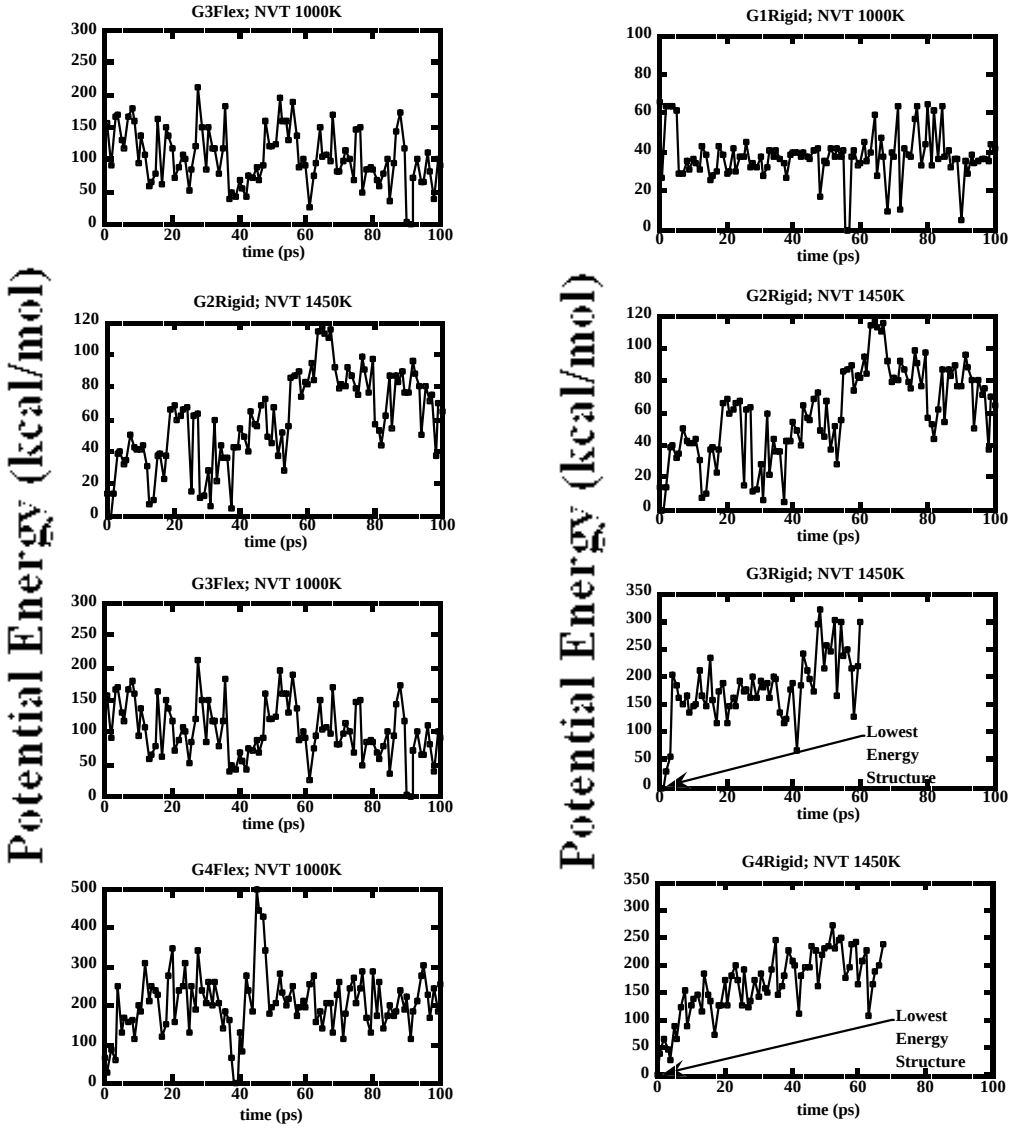

Figure A.6. ***Minimized*** **potential energy versus time during high temperature searches. Potential energy is relative to the lowest energy structure.**

The underlying reasons for the data trends outlined in Section 2.7.3 are: 1) in the case of **G3Rigid** and **G4Rigid**, the initially constructed configuration really is the most preferred or, 2) the intramolecular energy transfer within a large, rigid model is sufficiently poor that the present cooling rate fails to discriminate between high energy and low energy local minima. (i.e. Annealing is effectively too fast.) The latter is most likely for obvious reasons. The cooling schedule incorporated into the high temperature search routine employed here is 100K/ps and is rather fast. Nevertheless, the cooling stage still comprises 60% of the total computational time. The necessity for a practical yet effective cooling stage illustrates a major disadvantage of performing conformational searching in high temperature regimes.

A.3. Quenched molecular dynamics (Low Temperature Search)

A.3.1. General Procedure

Quenched molecular dynamics employs molecular dynamics simulations at *slightly* elevated temperatures (in contrast to the coarse-grained high temperature search outlined in Section 2.7.1 and 2.7.2) to map out the potential energy surface and generate a set of minimized structures that most likely represent important conformations at ambient temperatures. To perform this search, starting structures obtained from the search described in Sections 2.7.1 and 2.7.2 for each model were subjected to 250 ps of constant temperature dynamics at 500K (400K for **G3Rigid** and **G4Rigid**). Snapshots of trajectory coordinates were saved every ps, and subsequently minimized and saved. As a result, 251 minimized structures were generated for each molecule.

A successful search was one that produced a structure set incorporating several conformers within 10 kcal/mol of the lowest energy structure. This value represents the range of energy states that are thermally accessible at 500K. The choice of simulation temperature was critical for generating a reasonable number of low energy structures that fell within the energy cutoff (i.e. the cutoff specifying thermally accessible conformations). Simulation temperature used for **G1-G4Flex** and **G1-G2Rigid** was 500K. Simulation temperature used for **G3-G4Rigid** was 400K, since 500K dynamics

resulted in data sets characterized by only one low energy conformer within the applied energy cutoff and were thus deemed uninformative.

A.3.2. Evaluation of Low Temperature Search

Figures 2.22 and 2.23 show data for the "low temperature" conformational search. Each panel is a representation of 250 minimized structures generated for each search. Darkened bars represent structures < 10 kcal/mol of the lowest energy structure. Low energy conformers for each of the molecular models of the flexible dendrimers possess relatively large R_{core}/R_g values, indicative of substantial core offset from molecular center-of-mass. These data are summarized in Figure 2.11 and 2.12 in the Sections 2.4 and 2.5 of this chapter, indicating the large relative difference in core offset when each **GnFlex** model is compared with the analogous **GnRigid** model (n = 1– 4).

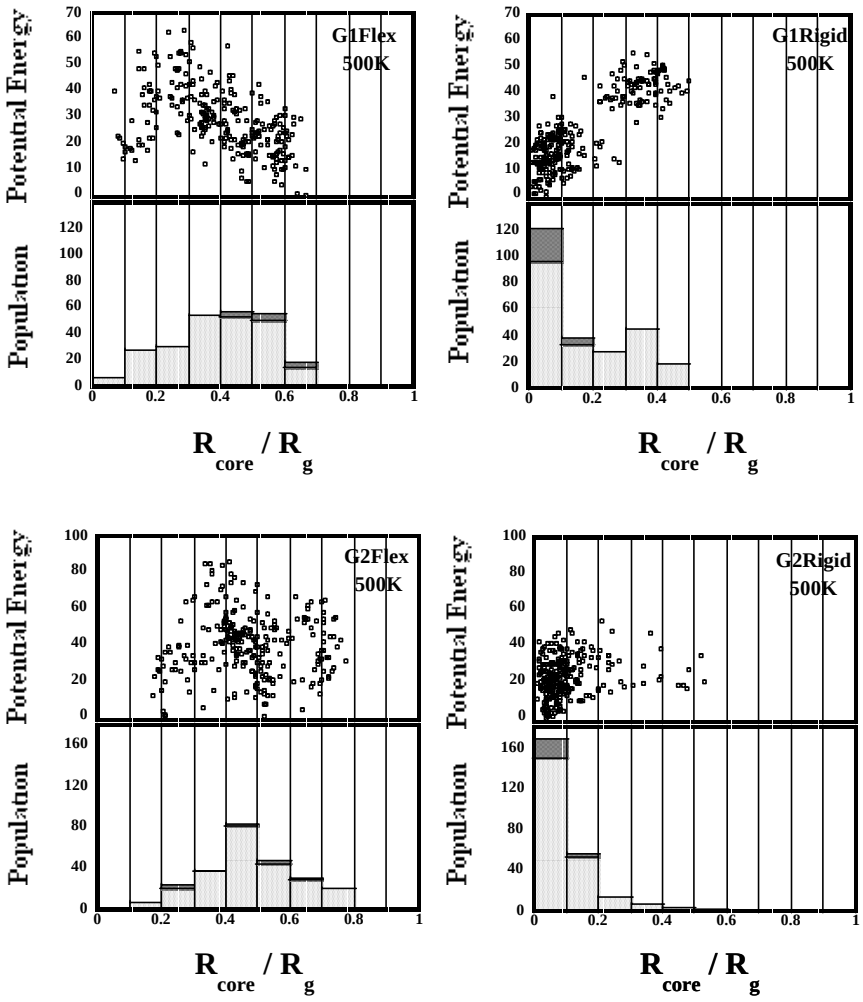

Figure A.7. Quenched dynamics results for G1 and G2 Flex and Rigid. Potential energy is relative to the lowest energy structure and in units of kcal/mol.

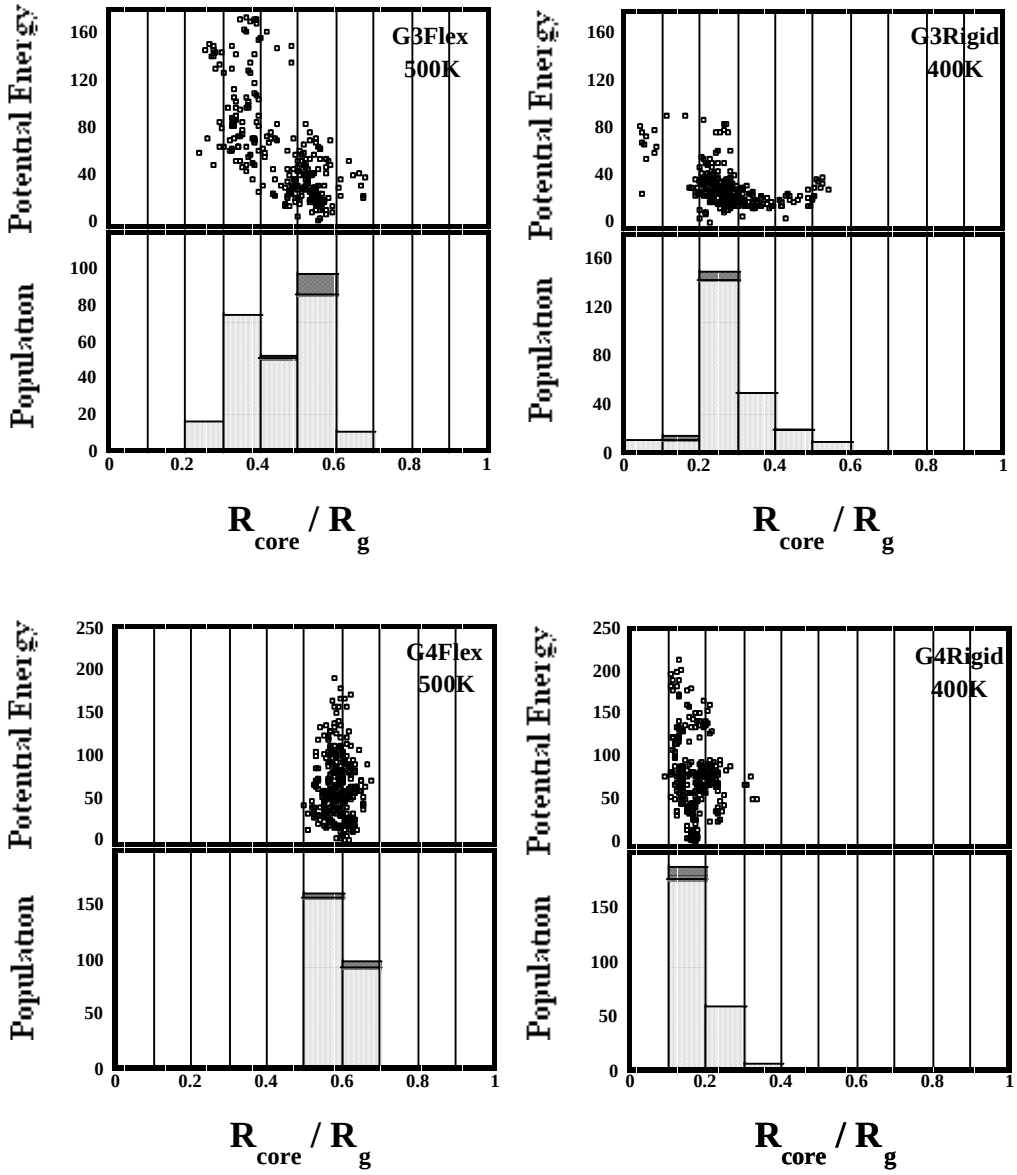

Figure A.8. Quenched dynamics results for G3 and G4 Flex and Rigid. Potential energy is relative to the lowest energy structure and in units of kcal/mol.

One can also note the relative variation in core mobility when comparing flexible and rigid models. In general, the searches on the flexible models found a wider geometric range of structures than did the searches on the rigid models. This was discussed in terms of the relative shape persistency of rigid models compared to their flexible counterparts. Interestingly, by these criteria, the fourth generation models (both **G4Flex** and **G4Rigid**) showed little geometric change over the course of this search. Although it is tempting to

hypothesize that this is the result of an increasing shape persistency as molecular size increases, it may also be the result of difficulties in sampling with increasing molecular size as discussed in Sections 2.2.1 and 2.2.2 for the "high temperature" search. Thus, we feel that this conclusion is probably not supportable given procedural uncertainties.

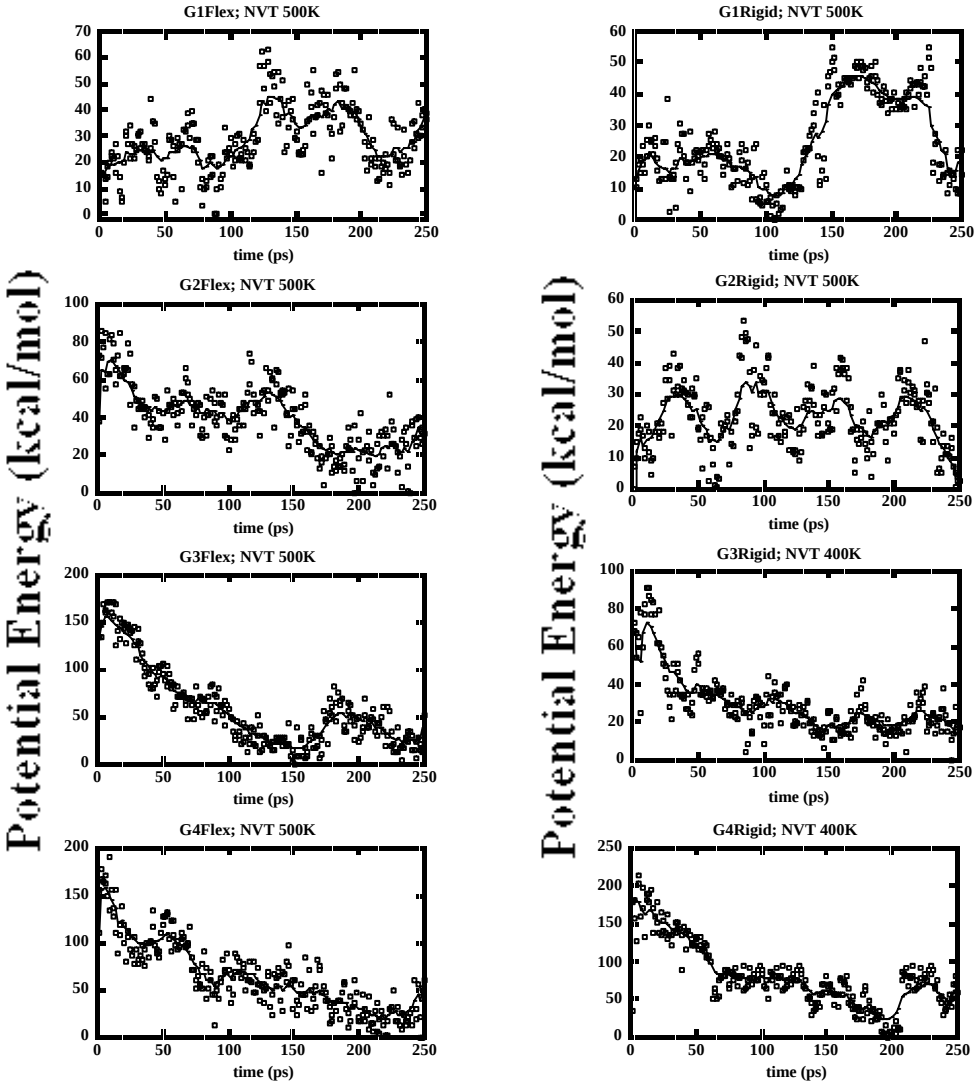

Figure A.9. *Minimized* potential energy versus time during low temperature quenched dynamics. Potential energy is relative to the lowest energy structure.

Figure A.9 contains data sets illustrating the evolution of the *minimized* potential energy (i.e. the "bottom" of the potential energy surface) with simulation time. This data is analogous to that shown in Figure A.6, which showed this data for the high temperature

(1000K or greater) searches. Again, lines are drawn through the data merely as a guide to the eye. These data indicate that for the **G3Rigid** and **G4Rigid** models, most of the minimized structures were lower in energy than the starting point. This observation obviated concerns that the final results of these two searches would be biased by the starting structure of the simulation. It further demonstrates that conformational searches for these large, rigid models is more effective in a low temperature regime rather than a high temperature regime.

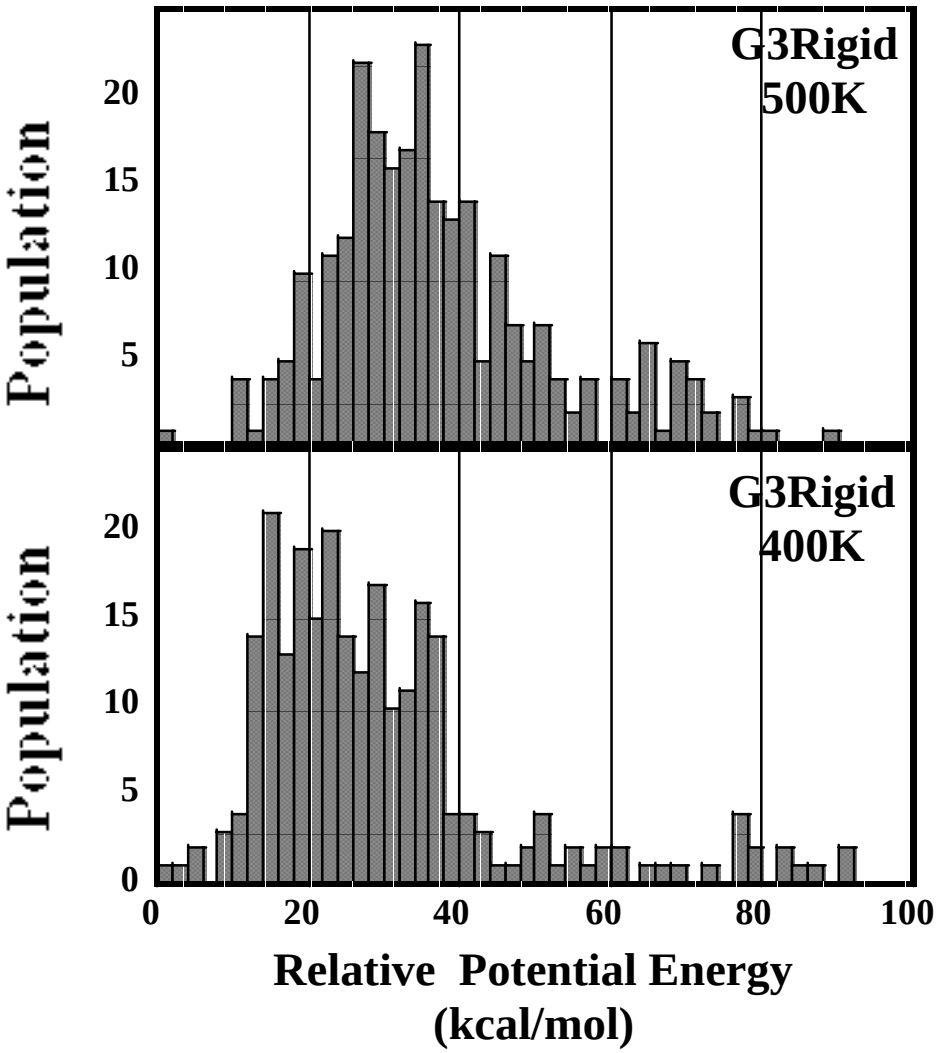

Figure A.10. Quenched dynamics histograms of *minimized* potential energies for G3Rigid at two temperatures, 400K (bottom) and 500K (top).

This notion is further supported by the data shown in Figure A.10. Note that the searches described in Figures 2.21 and 2.22 for the **G3Rigid** and **G4Rigid** models were conducted at 400K versus 500K for the other models. When the search was performed on **G3Rigid** at 500K only one energy minimum was found within the < 10 kcal/mol cutoff employed here (Figure A.25, top panel). However, when the search was performed on **G3Rigid** at 400K several energy minima were found within this cutoff (Figure A.10, bottom panel). A similar behavior was observed for the **G4Rigid** model. These results caused us to report the results of the 400K searches for these two models.

A.4. Alternative data representations

Relative core offset is but one geometrical parameter to consider. Alternative data representations of the lowest energy geometries found were produced. (Figure A.11 – A.14) The range of sizes, absolute core displacements, and molecular eccentricities were apparent from these data.

In most cases, the flexible dendrimers exhibit a broader range of geometries compared to their rigid counterpart. This effect is especially prominent in the data shown in the Radius of Gyration (R_g) and molecular eccentricity (Iz/Ix) histograms for generations 2-4. The inability of the rigid dendrimers to sample a range of molecular geometries is consistent with their postulated shape persistent nature.[44-46]

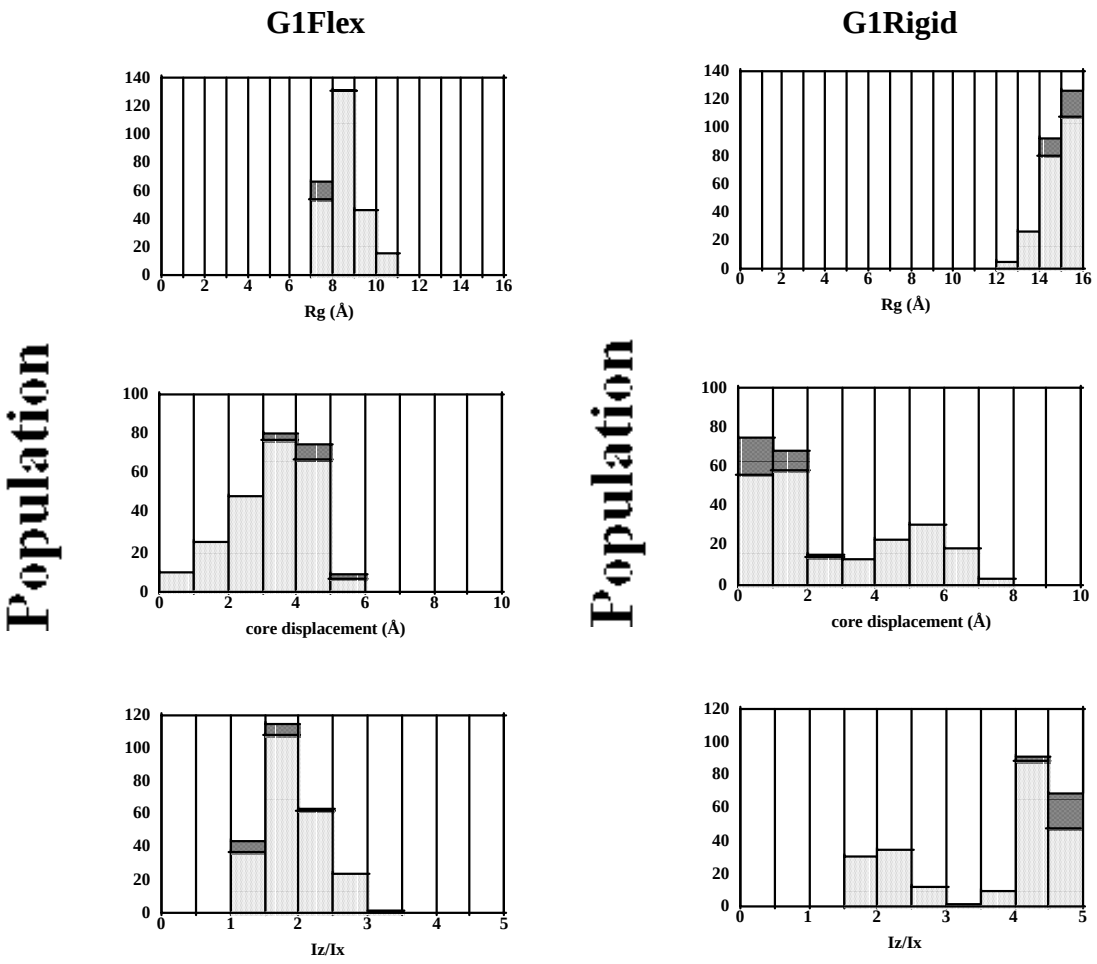

Figure A.11. Histograms for G1Flex (three left panels) and G1Rigid (three right panels) 500K searches using Radius of Gyration, Rg, absolute core displacement, and molecular eccentricity, Iz/Ix, as categories. The darkened bars indicate structures <10 kcal/mol from the lowest energy structure.

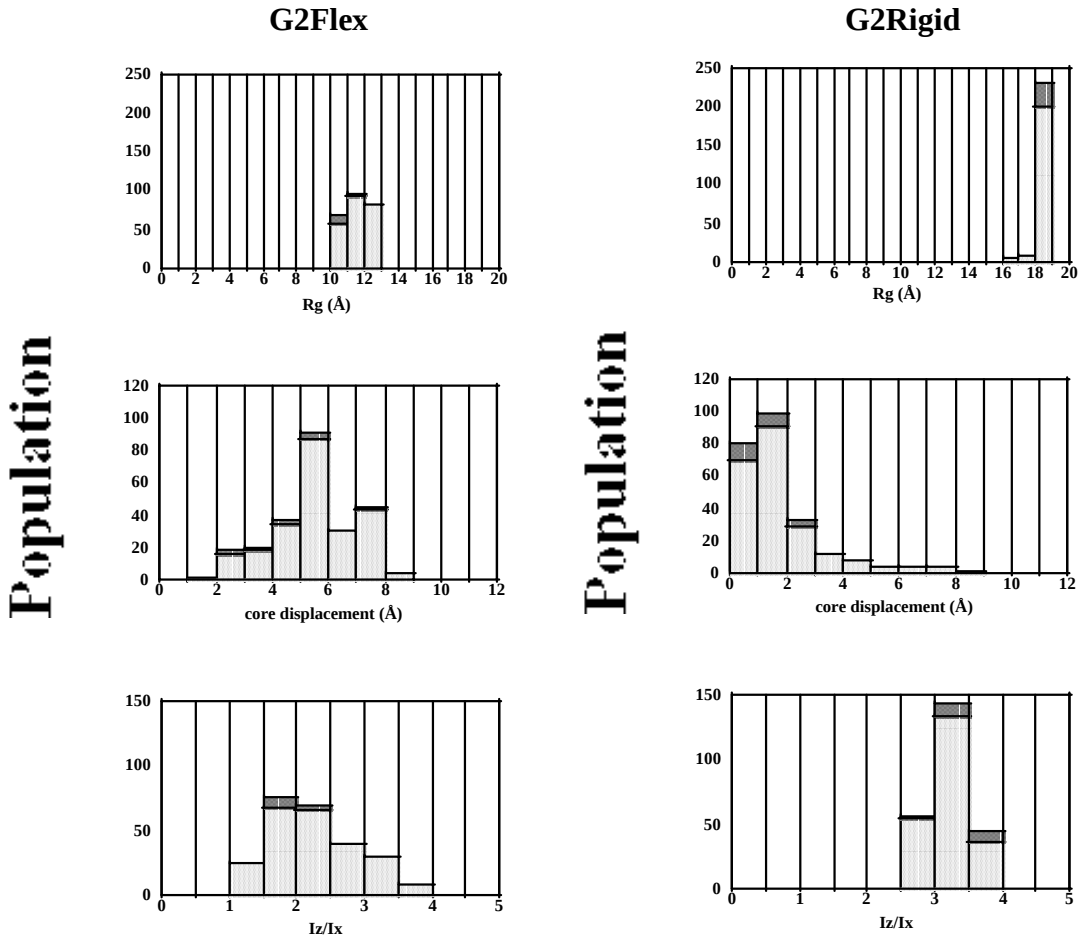

Figure A.12. Histograms for G2Flex (three left panels) and G2Rigid (three right panels) 500K searches using Radius of Gyration, Rg, absolute core displacement, and molecular eccentricity, Iz/Ix, as categories. The darkened bars indicate structures <10 kcal/mol from the lowest energy structure.

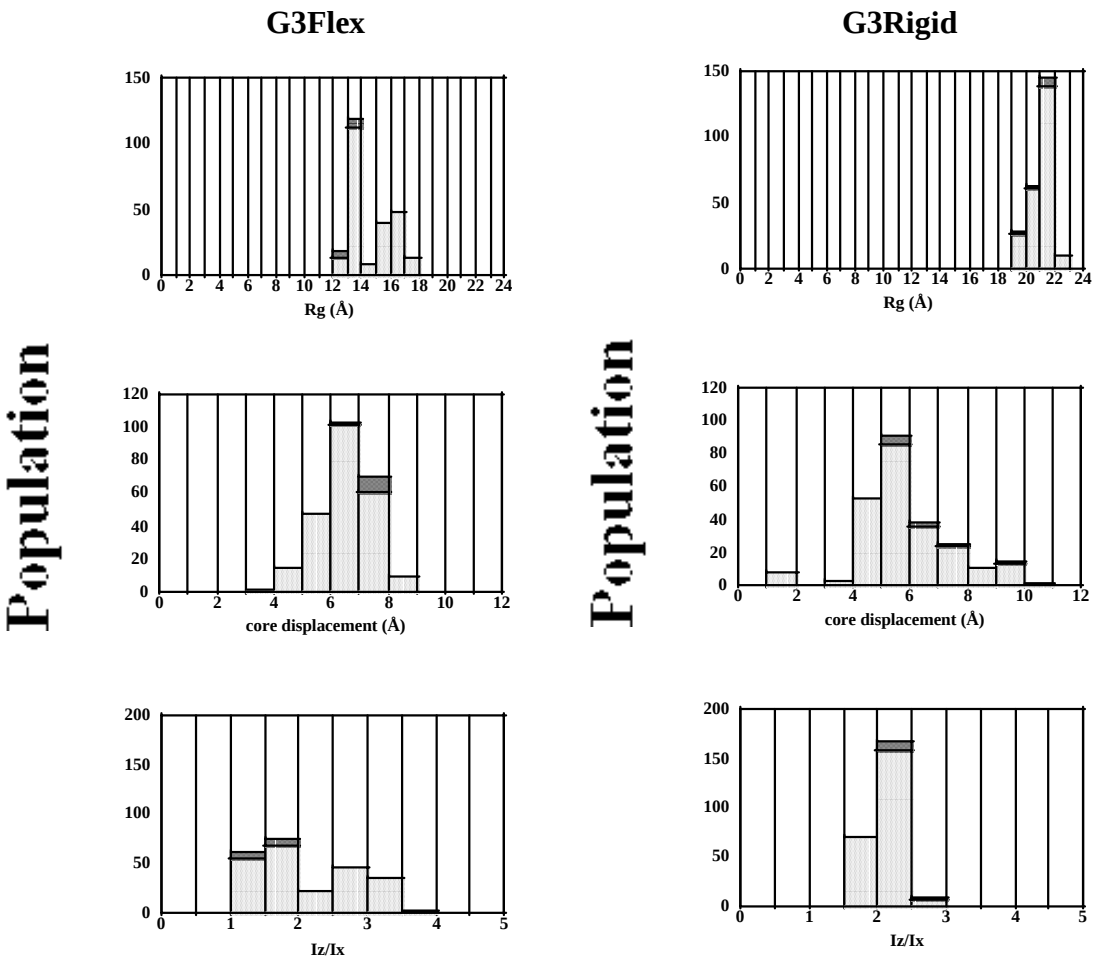

Figure A.13. Histograms for G3Flex (three left panels) and G3Rigid (three right panels) searches using Radius of Gyration, Rg, absolute core displacement, and molecular eccentricity, Iz/Ix, as categories. The darkened bars indicate structures <10 kcal/mol from the lowest energy structure. Search temperatures were 500K and 400K for G3Flex and G3Rigid respectively.

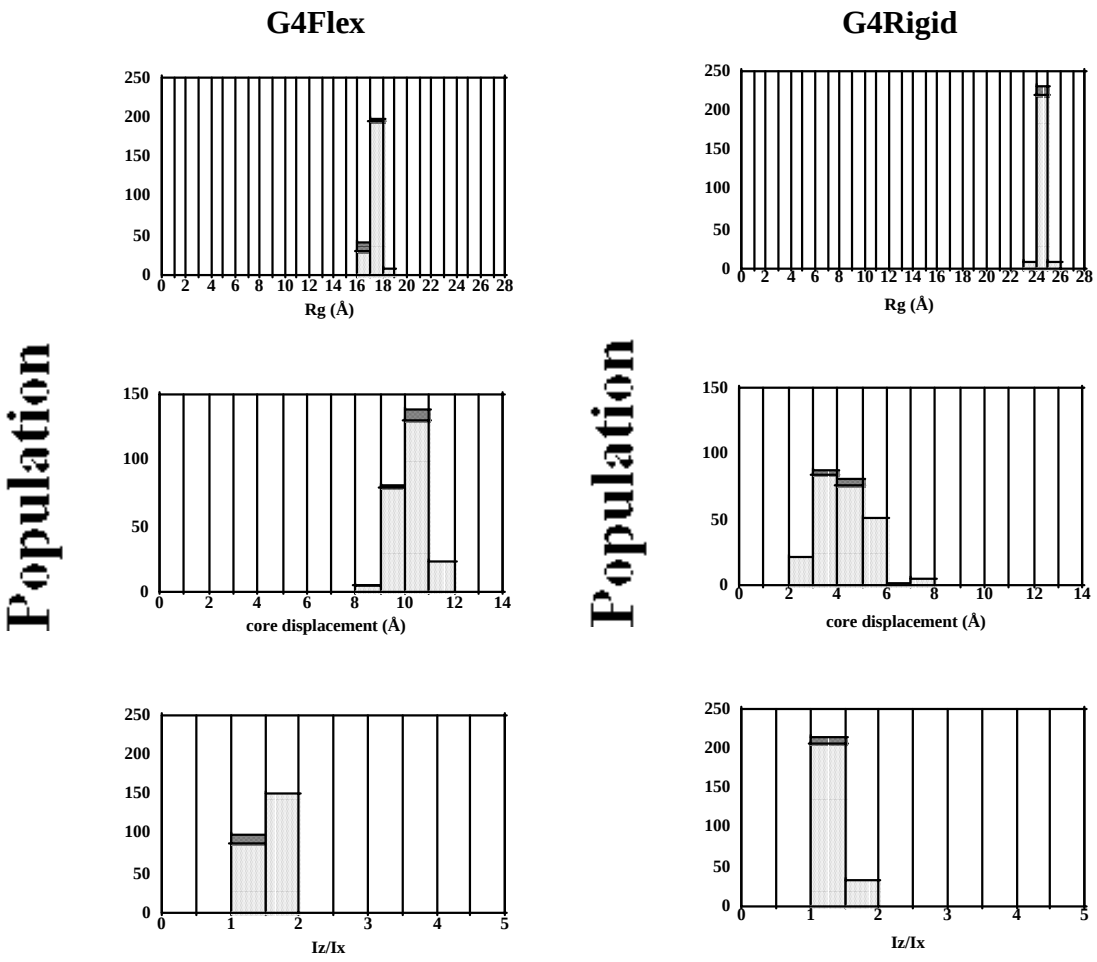

Figure A.14. Histograms for G4Flex (left three panels) and G4Rigid (right three panels) using Radius of Gyration, Rg, absolute core displacement, and molecular eccentricity, Iz/Ix, as categories. The darkened bars indicate structures <10 kcal/mol from the lowest energy structure. Search temperatures were 500K and 400K for G4Flex and G4Rigid respectively.

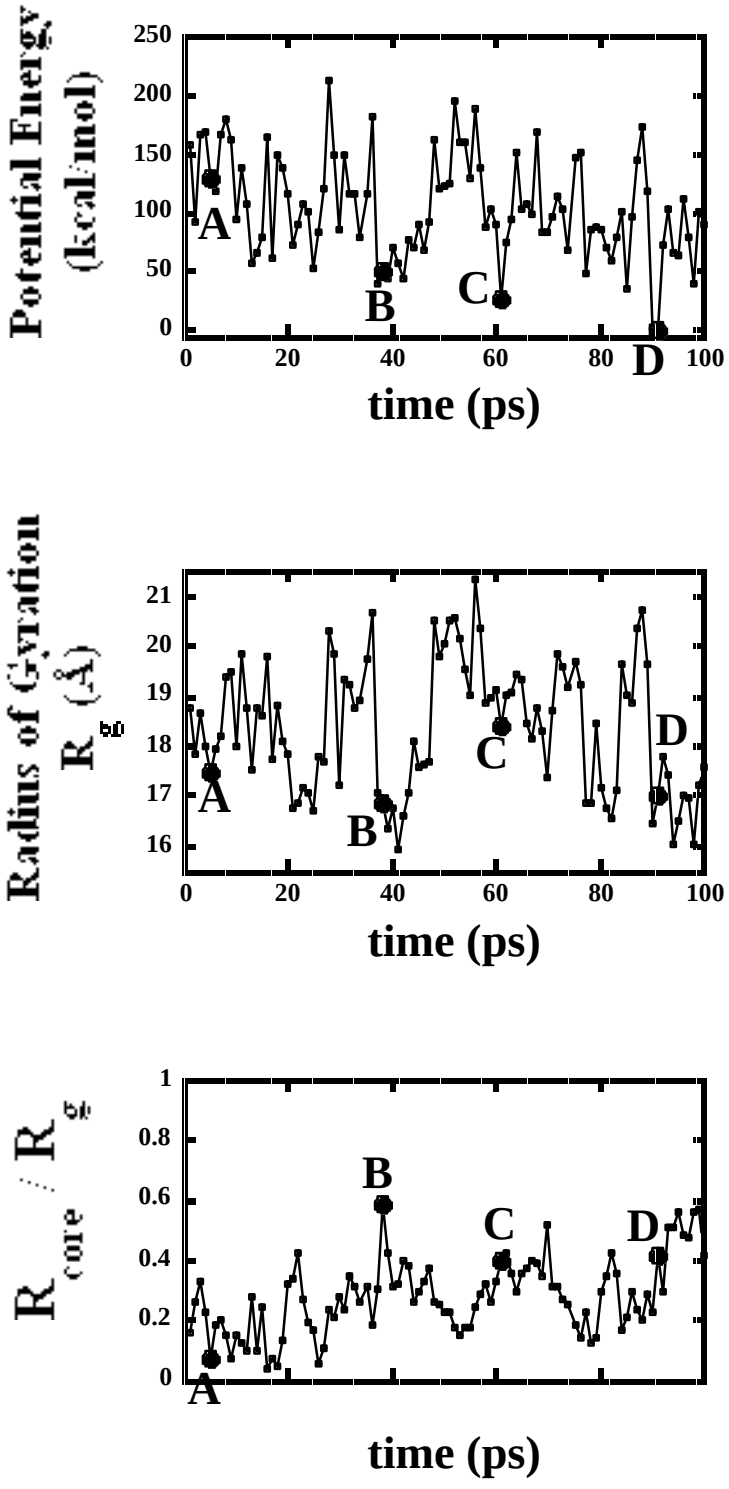

Figure A.15. High temperature search results for G3Flex. Three representations of the same data set are shown, namely, the *minimized* potential energy (top), Radius of Gyration (center), and Relative Core Offset, R_{core}/R_g (bottom) versus time. Enlargened points indicate start point of subsequent searches designed to test for dependence on start structure. Potential energy is relative to the lowest energy structure.

A.5. Search Validation

It is important to establish some degree of certainty for a novel conformational search routine. A helpful method for assessing the validity of a conformational search is to begin searches from several arbitrary starting points and verify that each search finds a similar set of structures. This test ensures that the search is not biased by the starting structure. Such a test was performed on the **G3Flex** model. Figure A.16 shows the results of a 100ps molecular dynamics simulation @1000K (high temperature search). The procedure used here was identical to that described for the coarse-grained high temperature searches described in Sections 2.7.1 and 2.7.2. Clearly a wide range of conformations was sampled as evidenced by a substantial range of relative potential energy, radius of gyration and core offset, respectively.

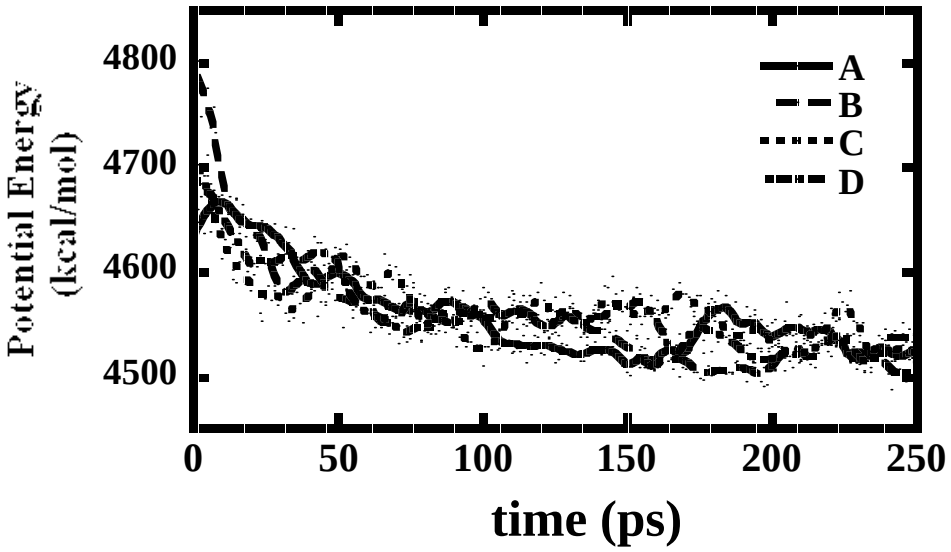

Figure A.16. ***Minimized*** **potential energy versus time during high temperature searches for the four starting point indicated in Figure A.15. The plots indicate convergence to similar potential energies.**

Thus, these data provide a set of unbiased structures to use as starting points in conformational searches. Four points in this trajectory were selected and used as the starting point for four conformational searches at 500K using the procedure described

2.2.1 and 2.2.2 for quenched dynamics. Figure A.16 indicates that the potential energy of the structures found in each of these four searches rapidly converged (within ca. 50 ps).

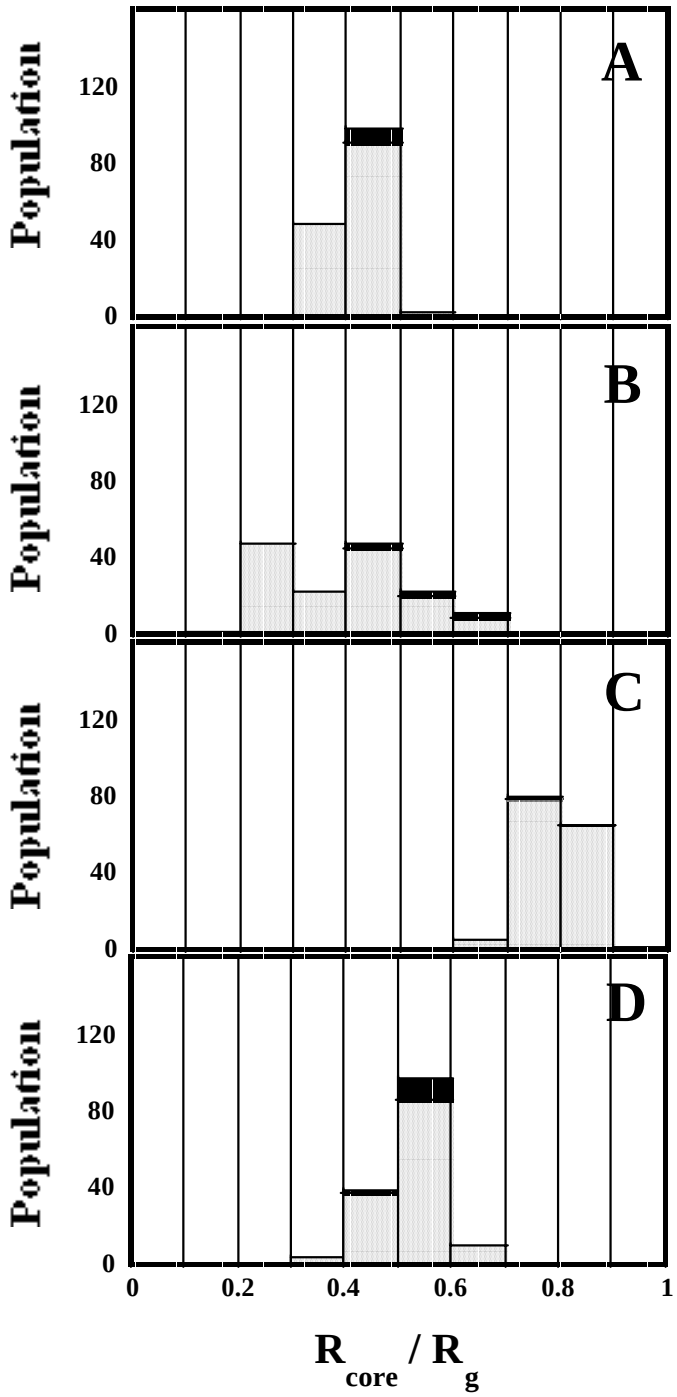

Figure A. 17. Lowest energy conformers (black bars in histogram indicate structures within 10 kcal/mol of the lowest energy structure) display an offset core in all four conformational searches. Therefore, the presence of an offset core in G3Flex is start structure-independent.

Figure A.17 shows the relative core offsets of the structures generated during the last 150 ps of this search and indicates that each search found structures with a substantially offset core. Although each of these searches clearly did not give identical results, the results were sufficiently similar to, in every case, support the conclusions made in this study.